PB-235 675

APPLICATION OF HOLOGRAPHIC METHODS TO THE MEASUREMENT OF FLAMES AND PARTICULATE. VOLUME II

B. J. Matthews, et al

TRW Systems Group

Prepared for:

Environmental Protection Agency

April 1974

DISTRIBUTED BY:

NTIS
National Technical Information Service
U. S. DEPARTMENT OF COMMERCE
5285 Port Royal Road, Springfield Va. 22151

TECHNICAL REPORT DATA

(Please read Instructions on the reverse before com

PB 235 675

1. REPORT NO. EPA-650/2-74-031-b	2.
4. TITLE AND SUBTITLE Application of Holographic Methods to the Measurement of Flames and Particulate, Volume II	5. REPORT DATE April 1974 6. PERFORMING ORGANIZATION CODE 11982
7. AUTHOR(S) B.J. Matthews and C.W. Lear	8. PERFORMING ORGANIZATION REPORT NO. TRW-23523-6001-TU-00
9. PERFORMING ORGANIZATION NAME AND ADDRESS TRW Systems Group One Space Park Redondo Beach, CA 90278	10. PROGRAM ELEMENT NO. 1AB014; ROAP 21ADG-51 11. CONTRACT/GRANT NO. 68-02-0603
12. SPONSORING AGENCY NAME AND ADDRESS EPA, Office of Research and Development NERC-RTP, Control Systems Laboratory Research Triangle Park, NC 27711	13. TYPE OF REPORT AND PERIOD COVERED Final 14. SPONSORING AGENCY CODE

15. SUPPLEMENTARY NOTES

16. ABSTRACT

The report gives results of an investigation to determine the feasibility of applying pulsed ruby laser holographic techniques to the measurement of particulate in the 1-micron and sub-micron size range. The investigation included the design and evaluation of a scattered light holocamera, and evaluation of the effects of four basic variables on scattered light methods. The variables were: particle size, angular illumination of the particle (scattering angle), particle number density, and incident laser beam diameter. The program included an analysis of the mathematical and physical models from which the transformation can be made from a scattered light distribution to a particle size distribution. The experimental portion of the program was conducted to assess the advantages and limitations of certain promising scattered light holographic methods.

17. KEY WORDS AND DOCUMENT ANALYSIS

a. DESCRIPTORS	b. IDENTIFIERS/OPEN ENDED TERMS	c. COSATI Field/Group
Air Pollution	Air Pollution Control	13B
Holography		14B
Particle Size		
Light Scattering		20N, 20F

18. DISTRIBUTION STATEMENT Unlimited	19. SECURITY CLASS *(This Report)* Unclassified	21. NO. OF PAGES 122
	20. SECURITY CLASS *(This page)* Unclassified	22. PRICE 4.50 - 2.25

EPA Form 2220-1 (9-73)

122

Reproduced by
NATIONAL TECHNICAL
INFORMATION SERVICE
U S Department of Commerce
Springfield VA 22151

EPA-650/2-74-031-b

APPLICATION OF HOLOGRAPHIC METHODS TO THE MEASUREMENT OF FLAMES AND PARTICULATE,

VOLUME II

by

B.J. Matthews and C.W. Lear

TRW Systems Group
One Space Park
Redondo Beach, California 90278

Contract No. 68-02-0603
ROAP No. 21ADG-51
Program Element No. 1AB014

Project Officer: William B. Kuykendal

Control Systems Laboratory
National Environmental Research Center
Research Triangle Park, N. C. 27711

Prepared for

OFFICE OF RESEARCH AND DEVELOPMENT
ENVIRONMENTAL PROTECTION AGENCY
WASHINGTON, D.C. 20460

April 1974

ia

This report has been reviewed by the Environmental Protection Agency and approved for publication. Approval does not signify that the contents necessarily reflect the views and policies of the Agency, nor does mention of trade names or commercial products constitute endorsement or recommendation for use.

TRW REPORT NO. 23523-6001-TU-00

APPLICATION OF HOLOGRAPHIC METHODS
TO THE
MEASUREMENT OF FLAMES AND PARTICULATE

VOLUME II

Prepared for

OFFICE OF RESEARCH AND DEVELOPMENT
ENVIRONMENTAL PROTECTION AGENCY
Washington, D.C. 20460

ABSTRACT

The report gives results of an investigation to determine the feasibility of applying pulsed ruby laser holographic techniques to the measurement of particulate in the 1-micron and sub-micron size range. The investigation included the design and evaluation of a scattered light holocamera, and evaluation of the effects of four basic variables on scattered light methods. The variables were: particle size, angular illumination of the particle (scattering angle), particle number density, and incident laser beam diameter. The program included an analysis of the mathematical and physical models from which the transformation can be made from a scattered light distribution to a particle size distribution. The experimental portion of the program was conducted to assess the advantages and limitations of certain promising scattered light holographic methods. This report was submitted in fulfillment of TRW Project No. 23523 and Contract No. 68-02-0603 by TRW Systems Group under the sponsorship of the Environmental Protection Agency. Work was completed as of November 1973.

Preceding page blank

CONTENTS

Page

1. OBJECTIVE AND SCOPE 1

2. PROBLEM ANALYSIS 3

   2.1 General Formalism 4
   2.2 Linearization and the "Inverse Problem" 7
   2.3 The Scattering Gain Matrix 10
   2.4 The Log Normal Distribution 20
   2.5 Estimation of Distribution Parameters for a Sub-Micron Particulate 24
   2.6 Discrimination Between Two Types of Particulate 30

3. EXPERIMENTAL PROGRAM 33

   3.1 Experimental Objectives 34
   3.2 Test Apparatus 39
   3.3 Experimental Procedures 60
   3.4 Results 71

4. CONCLUSIONS AND RECOMMENDATIONS 100

REFERENCES 101

APPENDICES

A THE IMAGINARY PART OF THE INDEX OF REFRACTION 103

B COMPUTER PROGRAM FOR FORWARD DIFFRACTION SCATTERING 105

Preceding page blank

ILLUSTRATIONS

Page

2-1 Angular Gain at θ = 90 Degrees for Totally Reflecting Spheres 15

2-2 Angular Gain at θ = 60 Degrees for Totally Reflecting Spheres 15

2-3 Angular Gain at θ = 120 Degrees for Totally Reflecting Spheres 16

2-4 Position and Value of the First Maximum of the Angular Gain Function for Totally Reflecting Spheres 17

2-5 Position and Value of the First Minimum of the Angular Gain Function for Totally Reflecting Spheres 18

2-6 Angular Gain at θ = 10 Degrees for Totally Reflecting Spheres 21

2-7 Scattering Diagram for Totally Reflecting Spheres in Each Polarization Mode 21

2-8 A Plot of the Function E (α,$\underline{p}$), Showing the Sensitive Dependence on σ and α 25

2-9 Scattering Diagram for Very Small Totally Reflecting Spheres 26

2-10 The Scattered Light Distribution for Particulate with X_g = 1.0 and σ_g = 1.7 29

3-1 Schematic Diagrams of Focused Ground Glass Holocamera Arrangements to Record Bright Field (Lower Diagram) and Dark Field (Upper Diagram) Scattered Light Holograms 41

3-2 Photograph of Breadboard Scattered Light Holographic Arrangement Shown in Figure 3-1 44

3-3 The Garrett Two-Beam Scattered Light Holocamera in its Completed Form 45

3-4 Three-Beam Breadboard Holocamera Used to Test Linearity and Sensitivity of the Holographic Process 46

3-5 Perspective Sketch of Wide Angle Double Reference Beam Holographic Arrangement 48

3-6 Layout Drawing of Wide Angle Double Reference Beam Breadboard Holocamera 49

ILLUSTRATIONS (Continued)

Page

3-7 Aerosol Solution Feed System 54

3-8 Voice Coil and Aerosol Generator Orifice Mount 55

3-9 Breadboard Three-Beam Wide Angle Scattered Light Holocamera With Monodisperse Aerosol Generating System 56

3-10 Geometry of Internally Scattered Light From a Liquid Aerosol Droplet of Diameter a 58

3-11 Nonlinear Diffraction Equations for Light Internally Reflected From a Sphere and the Two Branches of Their Solution 58

3-12 TRW Q-Switched Ruby Laser Illuminator 59

3-13 Ruby Laser Illuminator With Cover Removed to Show Location of Major Components 59

3-14 Schematic Diagram of Compact Ruby Laser Illuminator 61

3-15 Photograph of TRW Pulsed Ruby Laser Power Supply Consoles and Tektronix 535A Oscilloscope 62

3-16 The Optical Arrangement by Which Light Intensity From a Small Volume Element of the Reconstructed Real Image of a Hologram is Imaged Onto a Power Sensitive Detector ... 66

3-17 Photomicrographs of Sample "Micro-Balloons" 72

3-18 High Magnification Photomicrographs of Sample "Micro-balloons" 73

3-19 Photographs of the Reconstruction of Two Different Holograms 75

3-20 Photographs of the Reconstruction of Same Scattered Light Hologram of Glass Micro-Balloons of 30-Micron Typical Size 76

3-21 Photographs of the Reconstruction of the Same Hologram of Phenolic Micro-Balloons Recorded in the Dark Field Scattered Light Holocamera Shown in Figure 3-1........ 77

3-22 Sensiometric Curves of Emulsions Used In Holography 83

3-23 Primary Laser Beam Flux to Record Scattered Light Holograms of Individual Particles on Agfa 8E75 Plate 85

ILLUSTRATIONS (Continued)

Page

3-24 Schematic Diagram of Scattered Light Three-Beam Transmission Holocamera Test Setup 86

3-25 Reconstruction Photographs of Holograms 9A and 9B, Showing Forward and Side Scattering 88

3-26 Reconstruction of Hologram 12A, Showing Forward Scattered Light From Tobacco Smoke 90

3-27 Reconstruction Photos of Hologram 16A at 30 Degrees Scattering Angle, and Hologram 16C at 150 Degrees Scattering Angle 91

3-28 Observed and Calculated Scattered Light Intensity Distribution from Tobacco Smoke 92

TABLES

Page

2-1 A Matrix of Angular Scattering Gain Coefficients for Totally Reflecting Spheres, $\chi < 2$ 18

2-2 The First Five Angular Scattering Gain Coefficients for the Diffraction Approximation to Forward Scattering 19

2-3 A Comparison of the Rayleigh Coefficients, C^{42}, for Polarization in the Scattering Plane 26

2-4 Components of the H Matrix for $\chi g = 1$ and $\sigma g = 1.7$, and Components of the Resulting A Matrix Using the Forward Scattering Model of Equation (2-20). Components are normalized to $n_0 = 1$. 28

3-1 Reference and Scene Beam Intensities in Terms of Photocell Output 79

3-2 Transmission of Filters at 0.6328 Micron 80

3-3 Experimental Results 81

3-4 Maximum Velocity for Q-Switch Ruby Laser Forward-Scattered Hologram With Particle Moving Parallel to Hologram 98

3-5 Maximum Velocity for Q-Switched Ruby Laser for Different Ranges and for Particle Moving Parallel to Hologram and Viewing Along All Angles Perpendicular to Motion 98

3-6 Maximum Velocity for Q-Switched Ruby Laser Forward Scattered Hologram When Particle Moves Toward or Away from the Hologram 99

ACKNOWLEDGMENTS

We are indebted to Dr. R. F. Wuerker and Dr. L. O. Heflinger of the TRW Systems Group Research Staff for valuable technical assistance, and direct contribution to the work done on the Garrett holocamera and the holographic linearity and sensitivity tests. Thanks are also due to Mr. H. W. Reim and Mr. R. A. Briones for technical support of the holography.

NOMENCLATURE

a - Particle diameter - microns

$\underset{\sim}{A}$ - Matrix relating $\delta \underline{J}'$ to $\delta \underline{q}$

s - Area of intensity observing lens or telescope, cm^2

B - Effective hologram diameter, cm

$C^{\ell}(\theta)$ - Angular parts of the scattering gain function

d_s - Effective scattering diameter, cm

D - Orifice or aperture diameter - cm

$E(\alpha,p)$ - Exp $[\alpha\sigma^2 \; (2\bar{\mu} + \alpha\sigma^2]$: Normalization factor for log-normal distribution moment of order α.

$\underline{f}(\underset{\sim}{p},\mu)$ - Log-normal particle size distribution

$g_{\ell}(x)$ - Particulate distribution dependent parts of scattering gain function

$\underset{\sim}{G}$ - $4/x^2 \; (\underset{\sim}{S}^{*} : \underset{\sim}{S})$, the scattering gain function

$\underline{hi}$ - $\int_0^{\alpha} dx \; n_i(\underset{\sim}{p},\partial) \; x^{\underline{q}+2}$: augmented particulate distribution vector

H - $\int_0^{\alpha} dx \; (\partial n/2\underline{q}) \, x^{\underline{q}+2}$: particulate distribution matrix

$\underline{I}_o$ - Incident beam intensity, watts/cm^2

$\underline{J}$ - Light intensity distribution - watts/sterad-cm^3

k - π/λ, cm^{-1}

K - Ratio of scene beam to reference beam intensity

L - Fluid instability wavelength, cm

m - Complex index of refraction of particulate

$\underline{n}$ - Particle number density functions, particles/cm^2

p - Particulate distribution parameters

P - Power, watts

q - Re-indexed vector of particulate distribution parameters

Q_{sca} - $4\Sigma_{sca}/\pi a^2$, scattering efficiency

r - Vector from scattering source to center of A_o

R - Volumetric flow rate - cm^3/sec

S - Amplitude scattering matrix

u - $\ell n\ x$, log-normal distribution variable

u_i - Mean value of u under $f_i(p,u)$

v - Velocity, cm/sec

V_s - Volume containing scattering particulate, cm^3

x_g - e^u, geometric mean particle size

y - Focal length, cm

Z - Hologram-to-image distance, cm

Nomenclature - Greek

α - $q + 2$, distribution moment index

β - Angle of incidence

β' - Angle of refraction

γ - $\ell n\ n_o$, a log-normal distribution parameter

δ - Signifies increment

Δ - Optical path length

ϵ_s - Emulsion sensitivity, joules/cm^2

θ - Scattering angle or its complement, degrees

λ - Light wave length, microns

ν - Frequency - sec^{-1}

σ - Standard deviation of log-normal distribution

σ_g - e^{σ}, geometric standard deviation of particle distribution

Σ_{sca} - Total scattering cross section, cm^2

τ - Pulse time - sec

ϕ - Angle between $\overline{r}$ and the normal to s

Ω - Solid angle - steradians

χ - ka

Metric System Conversion Table

SYMBOL	WHEN YOU KNOW	MULTIPLY BY	TO FIND	SYMBOL
in.	inches	25.4	millimeters	mm
ft	feet	0.3048	meters	m
yd	yards	0.9144	meters	m
lb	pounds	0.453592	kilograms	kg
°F	Fahrenheit temperature	5/9 (after subtracting 32)	Celsius temperature	°C
psi	pounds per square inch	51.71	torr	torr
mm	millimeters	0.03937	inches	in.
m	meters	3.28084	feet	ft
m	meters	1.09361	yards	yd
kg	kilograms	2.20462	pounds	lb
°C	Celsius temperature	9/5 (then add 32)	Fahrenheit temperature	°F
torr	torr	0.01933	pounds per square inch	psi

1. OBJECTIVE AND SCOPE

The holography of particulate using scattered light techniques is concerned with demonstrating the feasibility of recording and identifying particulate in the one-micron and sub-micron size range. Development of such methods would provide new diagnostic tools in the form of various types of laser instrumentation which could be used in situ, and without disturbing the process being observed.

The work described herein is an extension of previous EPA holography studies.[1,2] These and other similar studies have already demonstrated the ability to holographically record micron size aerosols. Further, quantitative estimates of particle number densities as a function of scattered light intensity have been accomplished. The methodology thus far has been based on a simple model in which scattered light intensity is a function of a single parameter, usually the average product of number density and scattering cross section. The optical scattering cross section is assumed to be equal to the geometrical cross section multiplied by an optical factor depending only on scattering angle. The method is incapable of distinguishing between number density and mean particulate size, and some assumption must be made about one or the other in order to obtain useful information. The uncertainties, therefore, center on the problem of estimating particle size or size distribution from recorded or measured data on scattered light intensity, or by other means.

It would seem to be a fairly straightforward task to holographically record the laser light scattered from a particulate for all (or nearly all) scattering angles so that the scattered light angular distribution can be studied at leisure. It is an objective of the present study to demonstrate the feasibility of doing so. The second objective of the study is concerned with what useful information can be obtained about the particulate size distribution once such a scattered light distribution function is available. In particular, is there a way to extract both mean particle size and number density independently from the data? Can information also be obtained about the particulate size range? If a scattered light intensity as a continuous function of angle is given, is it possible to extract from it a continuous particulate size distribution function? And if two particulate distributions are present is it possible to distinguish between them? The answer to all these questions is a conditional "yes" based on the results of this study. In theory, at least, conditions can be found for which all of the desired information is contained in an angular distribution of scattered light. In practice, however, these conditions may not be so easy to establish.

The scope of this work includes an analysis of the mathematical and physical models by which the transformation can be made from a scattered light distribution to a particle size distribution. Also included is an experimental program designed to assess the advantages and limitations of certain promising scattered light holographic methods. The program includes the design and evaluation of a scattered light holocamera, and an evaluation of the effects of four basic variables on the scattered light methods. These four variables are: (1) particle size, (2) angular illumination of the particle (scattering angle), (3) particle number density, and (4) incident laser beam diameter.

2. PROBLEM ANALYSIS

In this section, a physical and mathematical formalism suitable for the study of light scattering by small particulate is presented. Existing formalism shows how to obtain a scattered light intensity distribution as a function of scattering angle, given a particle size distribution function. Conditions necessary to the solution of the "inverse problem" are derived; that is, given the scattered light distribution, find a unique particle size distribution. A possible numerical method of solution emerges from a study of these necessary conditions. Using a polynomial approximation for the scattering matrix and assuming a log normal type of particle distribution, we then determine the feasibility of estimating distribution parameters for a sub-micron particulate, and of differentiating between the number densities of a sub-micron and a 10-micron particulate size distribution both present in the same volume.

In the mathematical formalism which follows, vector quantities will be represented by a straight bar underlining the character. For example, $\underline{J}$ will be presented as a scattered light intensity vector having two components. Matrices and higher order tensors will be represented by a curved bar underlining the character. For example, the 2 by 2 scattering matrix is represented by a curved bar underlining the character. For example, the 2 by 2 scattering matrix is represented by $\underset{\sim}{S}$. The components of a vector or tensor will be represented by subscripts or superscripts, depending on whether the index property is contravariant or covariant. For practical purposes, contravariant indices will here represent the components of a column vector, and covariant indices represent the components of a row vector. When vector superscripts are used, they will be indicated as such; otherwise, a power function may be assumed. Because of an extensive use of subscripts and superscripts throughout this text, the same characters will sometimes appear as representing a variable and an index. The value of an index is entirely independent of the value of any variable bearing the same notation.

In writing vector inner products, summation notation over repeated indices will be assumed. Thus, an inner product

$$\underset{\sim}{S} \cdot \underset{\sim}{J} = S_i^n \, J_n$$

assumes sum over all n. Direct products of the form

$$\underset{\sim}{A} = \underline{q}\,\underline{C} = q_i\,C^k = A_i^k$$

will also be employed to form higher order tensors.

Complex conjugates will be denoted with an asterisk where variables have both real and imaginary parts. In the case of tensor quantities, the asterisk denotes a conjugate transposition of the tensor indices.

2.1 GENERAL FORMALISM

We first present a mathematical method by which an angular distribution of scattered light intensity can be obtained when particle number density is known as a function of particle size. The physical conditions under which this method is valid are discussed.

Let $J^n(\theta)\delta V_s \delta\Omega$ be the light intensity scattered out of a small, incremental unit of volume δV_s containing particulate and into an incremental unit of solid angle $\delta\Omega$, oriented at an angle θ from the forward path of the incident beam. The index n is a vector superscript taking the value n=1 if the light is polarized in the scattering plane or n=2 if polarized at right angles to it. The units of J^n will be watts/steradian$^{-cm^3}$ when the units of δV_s are cm^3. This notation is chosen to be consistent with that of Van de Hulst.[3]

Suppose the observing telescope used to make scattered light intensity measurements has an objective of area s_0, at a distance r from the source, and at an angle ϕ to the vector $\underline{r}$ from source to center of the objective. We assume s_0/r^2 is sufficiently small to approximate the solid angle. Then, the total power measured is:

$$P = \sum_n J^n(\theta)\,\delta V_s\,\delta\Omega \tag{2-1}$$

$$\delta\Omega = s_0 \cos\phi / r^2$$

Let $\underline{I}_0$ be the incident beam intensity in watts/cm^2, into the volume increment δV_s. Suppose δV_s has one particle, spherical, with diameter a and complex index of refraction m. Let $k=\pi/\lambda$ be the wave number of the incident wave amplitude into the scattered wave amplitude is a 2 by 2 nonsingular matrix denoted by $\underset{\sim}{S}(ka,\theta,m)$. The matrix is dimensionless and complex. The scattered light intensity from the particle is now represented as follows.[3]

$$\underline{J}(ka,\theta) = \frac{1}{k^2 \delta V_s} \underset{\sim}{S}^* \cdot \underset{\sim}{S} \cdot \underline{I}_o \qquad (2\text{-}2)$$

The two components of $\underline{I}_o$ and $\underline{J}$ represent simple linear combinations of four independent variables, called Stokes parameters, which completely describe the intensity and polarization of monochromatic light. Thus, the complete transformation matrix of Equation (2-2) would be a 4 by 4. In restricting ourselves to plane polarized light, we have effectively dropped the two Stokes parameters which describe the ellipticity and orientation of the polarization. The remaining two equations become decoupled from the set describing $\underline{J}$, and only the two equations in Equation (2-2) need be considered.

The next step is to fill δV_s with particulate having a range of diameters a, and sum or integrate an equation of the form (2-2) over all particle sizes. In doing this, we make three simplifying assumptions. First, we assume that the particulate is not optically dense, so that multiple scattering of photons does not occur. If multiple scattering should occur, Equation (2-2) becomes considerably more complicated to solve. The light will be depolarized, and the matrix will have off-diagonal terms which will depend on integrals of particle number density. Secondly, it is assumed that the particulate is small enough to avoid depolarization effects from higher order electromagnetic modes. This implies $ka \lesssim 10$. We may then assume that $\underset{\sim}{S}$ is a diagonal matrix, and the equations are further simplified. Finally, we assume that the particulate number density distribution is spatially uniform.

With these restrictions established, we define a particulate number density distribution $n(\underline{p},a)\text{cm}^{-4}$, so that $n(\underline{p},a)da$ is the number of particles per cm^3 having diameters between a and a+da, and

$$\int_0^\infty n(\underline{p},a)da = n_o \text{ particles/cm}^3 \qquad (2\text{-}3)$$

The $\underline{p}$ vector is a set of parameters for the distribution which fix, among other things perhaps, the value of n_o, the mean size of the distribution, and the standard deviation.

Suppose further that there are several different particle species in the volume δV_s, and that each has a separate distribution function $n_i(\underline{p}_i, a)$ associated with it. Then, the n_i can be treated as the components of a vector, and p_{ki} is a matrix. Each of the n_i has a different scattering matrix $\underset{\sim}{S}^i$ associated with it, so $\underset{\sim}{S}$ becomes a third order tensor. The scattered light intensity coming from these particulate distributions may now be written as follows:

$$J^n(\theta) = \frac{1}{k^2} \int_o^\infty da\; n_i(\underline{p}_i, a)\; \underset{\sim}{S}_m^{*in}\; \underset{\sim}{S}_{ij}^m\; (ka, \theta)\; I_o^{\,j} \tag{2-4}$$

$$\text{or,} \qquad \underline{J}(\theta) = \frac{1}{k^2} \int_o^\infty da\; \underline{n}(\underset{\sim}{p}, a) \cdot \underset{\sim}{S}^* : \underset{\sim}{S}(ka, \theta) \cdot \underline{I}_o$$

There are a few notational simplifications which will put Equation (2-4) in its final form. In order to simplify the integration, we will change to a variable χ.

$$\chi = ka \tag{2-5}$$

In rewriting $\underline{n}(\underset{\sim}{p}, \chi)$ the scale factor k then becomes a part of the parameter matrix $\underset{\sim}{p}$. We then define a tensor quantity $\underset{\sim}{G}(\chi, \theta)$ which we shall call the "scattering gain."[3]

$$S_m^{*in}\; S_{ij}^m = \frac{1}{4} \chi^2\; G_j^{ih} \tag{2-6}$$

$$\text{or,} \qquad \underset{\sim}{S}^* : \underset{\sim}{S}(ka, \theta) = \frac{1}{4} \chi^2\; \underset{\sim}{G}(\chi, \theta)$$

The function G is defined such that

$$\int d\Omega\; G(\chi, \theta) = 4\pi\; Q_{sca}$$

where $Q_{sca} = 4\,\Sigma_{sca}/\pi a^2$ is the total scattering efficiency.

Finally, suppose there are a number of specific values of θ, denoted θ_m, at which data are available. We now remove the variable θ and replace it with index notation, thus:

$$\underline{J}^n(\theta_m) = J_m^n \;;\; G_j^{in}\; (\chi, \theta_m) = G_{mj}^{in}\; (\chi) \tag{2-7}$$

and so on, where applicable.

Equations (2-5) through (2-7) into (2-4) can now be substituted, and the final form of the scattering equation be obtained.

$$J^n_m = \frac{1}{4k^2} \int_0^\infty dx\; n_i(\underline{p}_i, x)\; G^{in}_{mj}(x)\; I^j_o\; x^2 \tag{2-8}$$

The indices n and j of $\underset{\sim}{G}$ in this equation correspond to the indices of the original scattering matrix $\underset{\sim}{S}$. The index i denumerates the particulate species, and the index m denumerates scattering angle. The matrix $\underset{\sim}{G}^{i\cdot}_{m\cdot}$ for a given m and i is a positive definite diagonal matrix, which means that the equation for $\underline{J}^1$ is decoupled from that for $\underline{J}^2$. It is convenient to rewrite Equation (2-8) in partial index form which emphasizes the decoupling.

$$\underline{J}^n = \frac{1}{4k^2} \int_0^\infty dx\; n_i(\underline{p}_i, x) \cdot \underset{\sim}{G}^{in}(x) \cdot \underline{I}_o\; x^2$$

We have renormalized the n_i so that the units are cm^{-3} and

$$\int_o^\infty dx\; n_i(\underline{p}_i, x) = n_{oi} \text{ particles/cm}^3 \tag{2-9}$$

Equation (2-8) is a representation of the "normal" scattering problem, in which a gain tensor $\underset{\sim}{G}$ is given, and a particulate distribution $n_i(\underline{p}_i, x)$ along with its parameters is given, and the unknown to calculate is the scattered light intensity distribution on the left side of the equation. The $\underline{J}^n$ vectors may be looked upon as nonlinear functions of the distribution parameters $\underset{\sim}{p}$.

2.2 LINEARIZATION AND THE "INVERSE PROBLEM"

In the last section, we posed the problem of obtaining a scattered light density distribution off of a known particulate size distribution. We shall now formulate conditions necessary to solve the "inverse problem"; that is, given a scattered light intensity distribution, what is the particle distribution?

A number of previous investigators have defined and solved the inverse problem under various conditions and assumptions on the nature of the scattered light and particulate size distributions. Their work deserves some comment and reference here. A good overview of the problem has been given by Kerker[4], who has also reviewed previous investigations in some detail.

Among the methods more closely related to the one discussed in this report is one by Kerker, et al.[5] which makes use of the angular dependence of the ratio $J^1(\theta)/J^2(\theta)$. The method is similar to the present method in that it makes use of data matching at various scattering angles, and uses a parameter adjustment on a known mathematical model for the particulate distribution. Another widely used method involves the use of turbidity measurements, and Wallach and Heller[6] have shown the feasibility of using turbidity spectra of visible light at various scattering angles.

A number of techniques have been proposed[7,8,9] which are based upon the angular variation of the intensity of forward scattered light at very small angles and at a single wavelength. These deserve comparison with the analysis in this report. They involve integral transforms of scattered light distribution functions, and lead directly to a nonparametric distribution function n(a) without any a priori assumption of its form.

In Equation (2-8) we assume there is a mathematical model for the distributions $\underline{n}(\underset{\sim}{p},\chi)$ which is sufficiently general that any desired degree of agreement can be achieved with the actual distributions by choosing the parameters $\underset{\sim}{p}$ to fit the data. The more elements there are in the matrix, the more degrees of freedom are available to achieve the data match. In theory, an infinite number of p_{ij} would be required to fit a real distribution exactly. In practice, just a few will give a good approximation if the functional dependence $\underline{n}(\underset{\sim}{p},\chi)$ is chosen wisely.

The inverse problem can then be stated in terms of finding a solution to Equation (2-8) when the vector $\underline{J}^n$ is known and the parameter matrix $\underset{\sim}{p}$ is a matrix of unknown quantities which must be solved for.

The necessary and sufficient conditions that a unique solution $\underset{\sim}{p}$ exists are that $\underline{J}^n$ be an analytically continuous, single valued function of $\underset{\sim}{p}$ and that the values used for $\underline{J}^n$ lie within the solution space of Equation (2-8).

Suppose now there are measurements of the function $J^{n(\theta)}$ taken at angles θ_m. The data should correspond to the components of the J^n_m vector and may be represented by $\hat{J}^n_m$. Suppose a $\underset{\sim}{p}$ is found such that the following increment is small.

$$\delta J^n_m(\underset{\sim}{p}) = \hat{J}^n_m - J^n_m(\underset{\sim}{p}) \qquad (2\text{-}10)$$

We now perform a linearization of Equation (2-8) by using a first order Taylor series expansion.

$$\delta J_m^n = \frac{1}{4k^2} \int_0^\infty dx\ (\partial n_i/\partial p_{ki})\ G_{mj}^{in}\ I_o^j\ x^2\ \delta p_{ki} \tag{2-11}$$

The parameter p_{ki} is the k'th parameter for the i'th distribution. Equation (2-11) is a set of linear equations in the unknown variables p_{ki}. It is convenient to simplify the notation by rearranging the components of p_{ki} into a single vector $\underline{q}$, which has every parameter for each distribution.

$$q_j = p_{ki} \tag{2-12}$$

Then define a matrix A^n such that

$$\delta \underline{J}^n = \underset{\sim}{A}^n \cdot \delta \underline{q} \tag{2-13}$$

$$\underset{\sim}{A}^n = \frac{1}{4k^2} \int_0^\infty dx\ (\partial n_i/\partial \underline{q})\ \underset{\sim}{G}^{in} \cdot \underline{I}_o\ x^2$$

$$\text{or,} \qquad A_m^{nj} = \frac{1}{4k^2} \int_0^\infty dx\ (\partial n_i/\partial q_j)\ G_{m.}^{in} \cdot \underline{I}_o\ x^2$$

The superscript n may be considered as fixed, and it determines also which of the two components of I_o is selected. The indices j and m vary in such a way as to make of $\underset{\sim}{A}^n$ a second rank tensor — that is, a matrix.

The necessary and sufficient conditions that there be a unique solution vector, $\delta\underline{q}$, to Equation (2-13) may then be simply stated. The matrix $\underset{\sim}{A}^n$ must be square and nonsingular. It may be proven that these are also necessary and sufficient conditions that there be a locally unique solution matrix to the nonlinear inverse problem posed by Equation (2-8), and that they are also necessary conditions (but not sufficient) that there be a globally unique solution matrix.

The requirement that $\underset{\sim}{A}^n = A_m^{nj}$ be a square matrix dictates that the range of the index j equals that of the index m. This simply means that the number of angles θ_m at which there are data equals the number of parameters q_j for which we are solving. Every degree of freedom in $\underline{q}$ requires a data point to fix it. If $j > m$ there are more variables than equations, and the data are not sufficient to uniquely determine a solution to Equation (2-13).

In this case, there are an infinite number of solutions to the equations, all lying within a continuous (j-m)-dimensional subspace of the vector space having the same dimension as the range of j. If on the other hand $j < m$, there are more equations than variables, and the system of equations is overdetermined. In such cases, a least squares solution is often valid and useful.[10] Such a solution is one way of accounting for statistical errors in the data points $\hat{J}_m^n$.

We are now in a position to attempt to show the feasibility of finding a solution vector q_{ij} which satisfies the inverse problem. If we can show that the matrix $\underset{\sim}{A}^n$ of Equation (2-13) is nonsingular, and under what conditions, then we shall have established that at least the necessary conditions are met for the existence of a unique solution q_j, and therefore the solution is feasible. Furthermore, the analysis we are using suggests at least the possibility of a method of solution. For if a $\underset{\sim}{p}$ is found such that the increment computed from Equation (2-10), using (2-8) to calculate the $J_m^n(\underset{\sim}{p})$, is sufficiently small to support the linearization approximation, then Equation (2-13) can be used to calculate the $\underset{\sim}{A}^n$ matrix using the same $\underset{\sim}{p}$. The linear equations can then be solved to find the errors in the $\underset{\sim}{p}$ matrix, and thereby improve our estimate of it. The new estimate can then be used in a recalculation, and an iterative procedure will refine the solution to the best possible degree of accuracy.

To summarize, the basic linearized equations we have derived thus far are as follows:

$$J_m^n\,(\underset{\sim}{p}) = \frac{1}{4k^2}\int_0^\infty dx\; n_i(\underline{p}_i, x)\; G_{mj}^{in}\,(x)\; I_o^j\, x^2 \tag{2-8}$$

$$\hat{J}_m^n - J_m^n\,(\underset{\sim}{p}) = \underset{\sim}{A}^n \cdot \delta \underline{q} \tag{2-13}$$

$$A_m^{nj} = \frac{1}{4k^2}\int_0^\infty dx\; (\partial n_i/\partial q_i)\; \underline{G}_m^{in} \cdot \underline{I}_o\, x^2$$

2.3 THE SCATTERING GAIN MATRIX

In order for Equation (2-13) to yield a nonsingular $\underset{\sim}{A}^n$ matrix, the $\underset{\sim}{A}^n$ matrix must be of full rank, and the gain matrix $\underset{\sim}{G}$ must be of equal rank. This condition will be satisfied if each of the $\underline{G}_j^{in}$ vectors is linearly independent. In this case, we may loosely speak of $\underset{\sim}{G}$ as being nonsingular with respect to the index m. In this section we discuss some conditions for the nonsingularity of $\underset{\sim}{G}$. We then investigate some properties of the gain matrices for totally reflecting spheres, and for small angle scattering of diffracted light, with the aim of establishing nonsingularity for a special case.

We begin with the assumption that the gain function can be written in the following series form, where q is the summation index of the series.

$$G_j^{in}(\chi,\theta) = g_{qk}^{i}(\chi)\; C_j^{qkn}(\theta) \tag{2-14}$$

Thus, each term of the series is separable in χ and θ. The indices i and k refer to particle species, and g_{qk}^{i} is non-zero only for i=k. The n and j indices refer, as before, to the state of polarization of the incoming and outgoing light. The series (2-14) may be infinite, in which case $q=0,1,2,\ldots,\infty$. The functions $g_q(\chi)$ and $C^q(\theta)$ may be taken as complete sets of orthonormal functions, in which case Equation (2-14) will describe any desired gain function, either calculated from theory or measured from experimental data. If we now choose $\theta=\theta_m$, where scattering data are available, we recover the originally defined gain tensor.

$$\begin{gathered} \underset{\sim}{G}(\chi) = \underset{\sim}{g}(\chi) : \underset{\sim}{C} \\ G_{mj}^{in}(\chi) = g_{qk}^{i}(\chi)\; C_{mj}^{qkn} \end{gathered} \tag{2-15}$$

Using this form for G, we can now rewrite the basic elements of the linearized equations from Equations (2-8) and (2-13).

$$\begin{gathered} \underline{J}^n = \frac{1}{4k^2}\left[\int_0^\infty d\chi\; \underline{n}(p,\chi)\cdot \underset{\sim}{g}(\chi)\,\chi^2\right] : \underset{\sim}{C}^n\cdot \underline{I}_o \\ \underset{\sim}{A}^n = \frac{1}{4k^2}\left[\int_0^\infty d\chi\; (\partial \underline{n}/\partial \underline{q})\cdot \underset{\sim}{g}(\chi)\,\chi^2\right] : \underset{\sim}{C}^n\cdot \underline{I}_o \end{gathered} \tag{2-16}$$

In index notation,

$$A_m^{nj} = \frac{1}{4k^2}\left[\int_0^\infty d\chi\; (\partial n_i/\partial q_j)\; g_{qk}^{i}(\chi)\,\chi^2\right] C_{mp}^{qkn}\; I_o^p$$

In each of these equations, the quantity in brackets is an integral tensor of second or third order, computed entirely from functions of χ and the parameters, p. All of the angular dependence is contained in the tensors $\underset{\sim}{C}^n \cdot \underline{I}_o$. These tensors are also third order. For a given value of the index k, corresponding to a given particulate species, the elements of $\underset{\sim}{C}^{\cdot kn} \cdot \underline{I}_o$ form a matrix. Should only one species be present, this matrix must then be shown to be nonsingular with respect to the index m. If several species are present, then it is a linear superposition of these matrices which must be shown to be of full rank.

A particular case of interest arises when the index q has only one value. Then the gain matrix is a direct product of a function of χ and a function of θ. Such is the case, for example, for small particulate Rayleigh scattering ($\chi \ll 1$) or large particulate isotropic scattering ($\chi \gg 1$). It is convenient to drop the index q in Equation (2-16). Suppose also there is only one particulate distribution, and drop the index i. Suppose I_o has only one non-zero component, and drop the index p. Then the matrix expression is greatly simplified.

$$\underset{\sim}{A}^n = \frac{I_o}{4k^2} \left[\int_o^\infty d\chi \, (\partial n / \partial \underline{q}) \; g(\chi) \; \chi^2 \right] \underline{C}^n$$

This is the direct product of two vectors, one of which is the column vector $\underline{C}^n$. This means that every column vector of $\underset{\sim}{A}^n$ is a multiple of $\underline{C}^n$, and $\underset{\sim}{A}^n$ has rank one. Thus, $\underset{\sim}{A}^n$ is nonsingular only if it is a scalar. Only one value of q can be estimated from light scattering data.

Reintroducing the index q only, we can replace $g(\chi)$ with a vector $g_q(\chi)$ and the vector C^n with a matrix $C_m^{q \cdot n}$. Then, Equation (2-16) gives

$$\underset{\sim}{A}^n = \frac{I_o}{4k^2} \left[\int_o^\infty d\chi \, (\partial n / \partial \underline{q}) \; \underline{g}(\chi) \; \chi^2 \right] \cdot \underset{\sim}{C}^n \qquad (2\text{-}17)$$

In this equation, the matrix C^n must be nonsingular with respect to the index m, which means that the range of q must be at least as great as the range of m. This establishes a condition on the number of non-zero terms in the series of Equation (2-15). There must be at least as many terms as the number of parameters to be estimated.

Among the various sets of orthonormal functions which can be used for $\underline{g}(x)$ in Equation (2-17), are several polynomials. Of these, the associated Legendre polynomials, for example, have a density function of unity. It is reasonable to expect, then, that with a suitable choice of the coefficient matrix $\underset{\sim}{C}$, we can choose a form

$$g_q(x) \sim x^q$$

and obtain the gain function dependence on x to any desired degree of accuracy. This is in fact the case. Much of the existing theoretical work on the description of the scattering gain function is expressed in terms of infinite converging series in the variable x.

There is good motivation for this choice of $\underline{g}(x)$, since for some density functions the integral in Equation (2-17) can then be evaluated directly. Accordingly, we define a matrix $\underset{\sim}{H}$ and simplify Equation (2-17) once more.

$$\underset{\sim}{A}^n = \frac{I_o}{4k^2} \underset{\sim}{H} \cdot \underset{\sim}{C}^n \tag{2-18}$$

$$\text{or,} \qquad A_m^{nj} = \frac{I_o}{4k^2} H_q^j \, C_m^{qn}$$

$$\text{where} \qquad H_q^j = \int_0^\infty dx \, (\partial n/\partial q_j) \, x^{q+2}$$

In the remainder of this section, we will discuss some possible choices for a particular matrix, $\underset{\sim}{C}^2$, for light polarized parallel to the plane of reflection. In Section 2.1, we referred to the fact that $\underline{S}$, and then $\underline{G}$, is a function of the particulate index of refraction, m. Thus far we have not made use of that dependence. As we now begin to discuss some particular gain matrices, however, we must make some assumptions about the optical properties of the scattering particulate. These include properties of light absorption, refraction and reflection, all of which are implied by a given complex index of refraction (see Appendix A). As we calculate a polynomial fit to a particular gain matrix, the scattering gain coefficients $\underset{\sim}{C}$ will then depend on the chosen index of refraction.

In general, gain function dependence on angle and particle size is very complex, exhibiting multiple lobe structure and ripple structure. One way to picture them is as a multimode superposition of complex harmonic functions. These are difficult to model analytically, since they generally require many terms of an infinite series expansion to obtain sufficient convergence to describe the function over the complete range of interest.

One case which is at least conceptually less complex is the gain function for totally reflecting spheres. The index of refraction for total reflection is real and infinite. The resulting lobe structure varies more smoothly and regularly, and does not exhibit any significant secondary ripple structure such as is characteristic of normal dielectrics. Kerker[4] gives calculated values for gain functions for totally reflecting spheres in the size range $0 < X < 10$. This is the range of interest for the present work, which is oriented toward particulates sizes of 0.1 micron to 1 micron, and 0.6942 micron ruby laser light. For this wavelength, a 1-micron particle gives X equal 4.5 .

The applicability of the assumption of total reflection is somewhat limited in industrially generated particulate. The dispersive properties of some dielectrics, especially water and ice, may result in a high enough index of refraction, with little absorption, at longer wavelengths. In the case of water droplets, however, the wavelength range is below the visible.

Figures 2-1, 2-2 and 2-3 show angular gain functions, following Kerker, for totally reflecting spheres. The 60-degree angle corresponds to forward scattering, and the other two angles are 90 and 120 degrees. The leading term in the series expansion for the gain function is in X^4, corresponding to Rayleigh scattering. Thus, the following three term polynomial approximation to the gain function was attempted for $X \lesssim 2$.

$$G^2(X,\theta) = C^{42}(\theta)X^4 + C^{62}(\theta)X^6 + C^{82}(\theta)X^8 \qquad (2\text{-}19)$$

This expression has three independent coefficients which can be adjusted to obtain the best fit for each θ. It therefore has enough degrees of freedom to estimate up to three particulate distribution parameters. In the next section, a particular three parameter adjustment will be suggested.

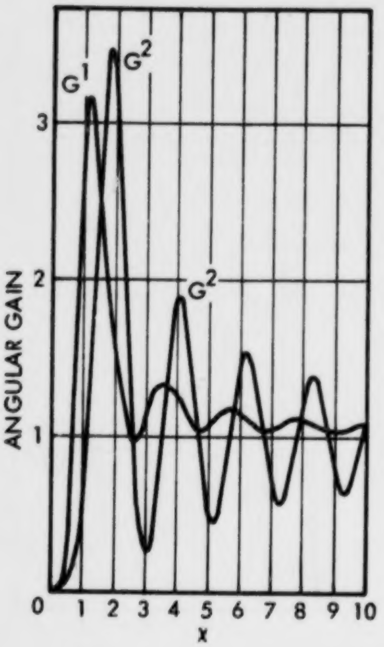

Figure 2-1. Angular Gain at θ = 90 Degrees for Totally Reflecting Spheres

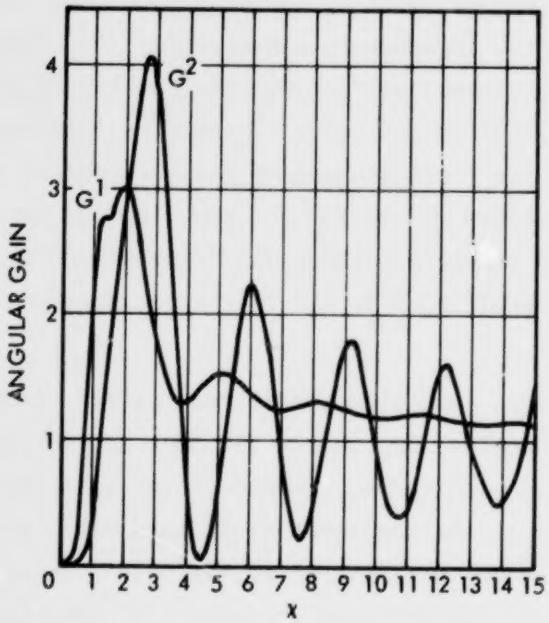

Figure 2-2. Angular Gain at θ = 60 Degrees for Totally Reflecting Spheres

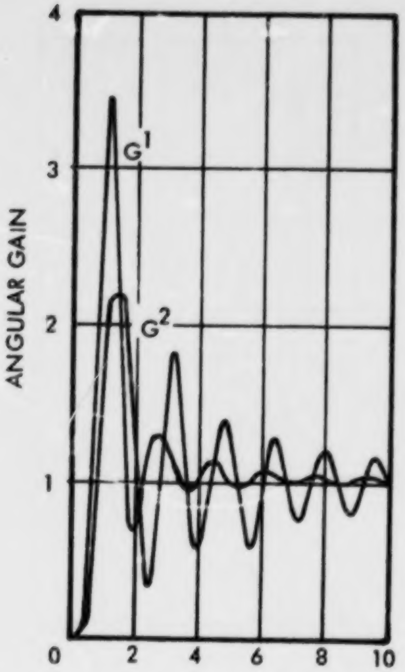

Figure 2-3. Angular Gain at θ = 120 Degrees for Totally Reflecting Spheres

Even in the limited range of X, the gain functions require many more terms than three to give an adequate convergence. In order to obtain a good fit with just the three coefficients of Equation (2-19), they were chosen to match the position and value of the first maximum, and to pass through the point at the first minimum of the theoretical curves. Figure 2-4 shows the interpolated values for the position and height of the first maximum of $G^2(X)$, and Figure 2-5 shows the interpolated values for the first minimum. The resulting fit is a fair approximation to most portions of the first peak.

Table 2-1 shows the resulting coefficient matrix, computed for three different scattering angles, 30, 90 and 150 degrees, corresponding to forward, side, and back scattering. These angles were chosen to fit the experimental geometry of the scattered light holocamera described in Section 3.2. A calculation of the determinant of the matrix shows that it is nonsingular and fairly well conditioned for numerical inversion.

A second approach to the scattering gain matrix calculation was investigated, which makes use of some simple and more general properties of forward scattered light.

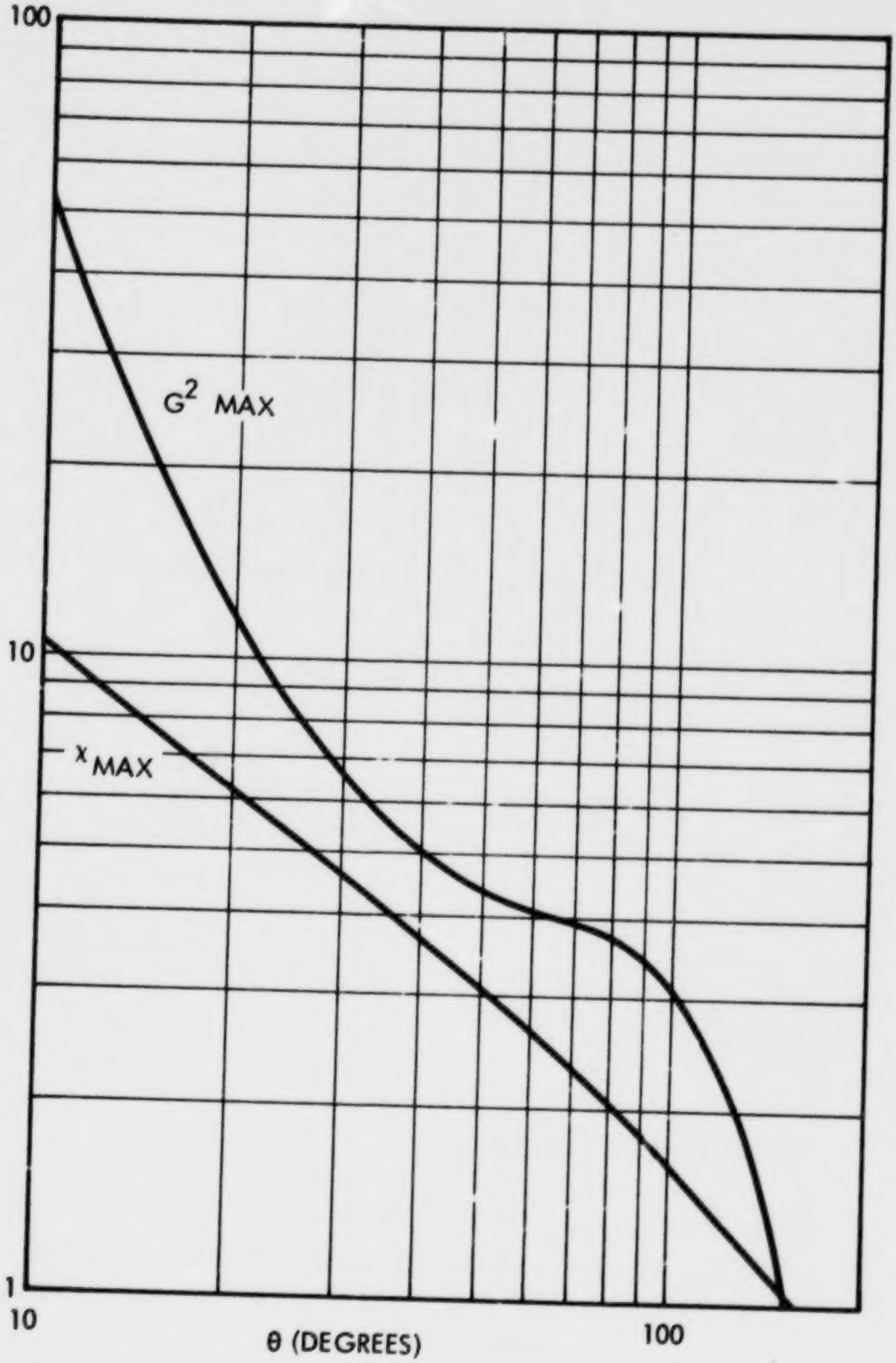

Figure 2-4. Position and Value of the First Maximum of the Angular Gain Function for Totally Reflecting Spheres

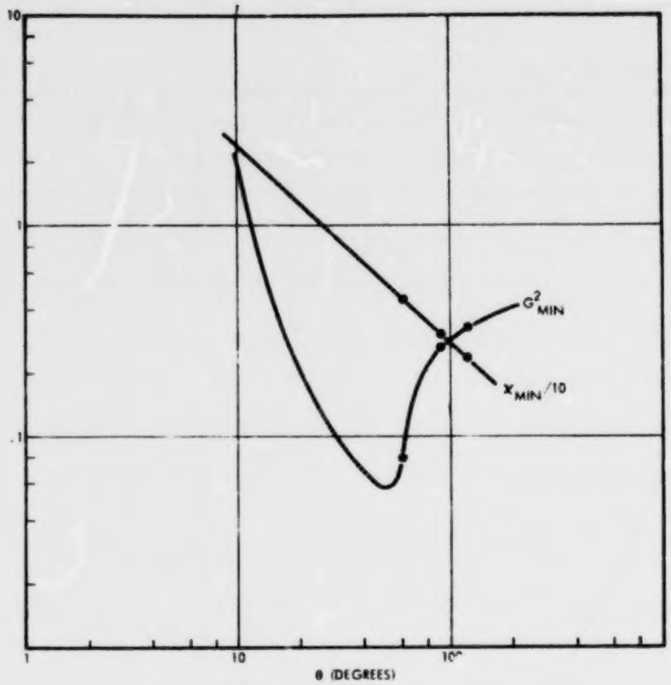

Figure 2-5. Position and Value of the First Minimum of the Angular Gain Function for Totally Reflecting Spheres

Table 2-1. A Matrix of Angular Scattering Gain Coefficients for Totally Reflecting Spheres, $X < 2$.

	C^{42}	C^{62}	C^{82}
$\theta = 30°$	0.05391	-0.002309	0.00002163
$\theta = 90°$	1.220	-0.3519	0.02408
$\theta = 150°$	3.229	-2.646	0.4873

Determinant: 0.00462

The forward lobe of the scattered light intensity distribution is due primarily to Fraunhofer diffraction, and arises predominantly from light passing near the particle, rather than from rays which undergo refraction and reflection. It is thus independent of the index of refraction of the scattering medium. The angular gain function for diffraction scattering is given by[4]

$$G_j^{in}(X,\theta) = \left[2J_1(X\sin\theta)/\sin\right]^2 \delta_j^i \qquad (2\text{-}20)$$

which is valid for both n=1 and n=2. J_1 here indicates the first order Bessel function. This approximation is good for forward scattering angles up to about 30 degrees over a wide range of $X\,(0<X<20)$. Thus, it is less limited than the previous approximation.

The Bessel function has a series expansion of the form

$$J_1(X\sin\theta) = \sum_{k=0}^{\infty} \frac{(-1)^k(\frac{1}{2}X\sin\theta)^{2k+1}}{k!\,(k+1)!} \qquad (2\text{-}21)$$

which can be inserted in Equation (2-20) to obtain the scattering matrix coefficients $\underset{\sim}{C}^n$. Only even powers of X appear. The first five non-zero coefficients have been calculated, and are shown in Table 2-2.

The method of Shifrin et al[8] also makes use of a small angle approximation of Equation (2-20). Their method gives a particulate distribution, using an integral transform, without assuming an a priori form. Its range of usefulness is limited to θ less than about 10 degrees, however. This method and other similar methods are very useful and popular for particulates exhibiting strong forward scattering.

Table 2-2. The First Five Angular Scattering Gain Coefficients for the Diffraction Approximation to Forward Scattering

$C^2(\theta)$	1
$C^4(\theta)$	$(-1/4)\sin^2\theta$
$C^6(\theta)$	$(5/2^4 \times 2! \times 3!)\sin^4\theta$
$C^8(\theta)$	$(-14/2^6 \times 3! \times 4!)\sin^6\theta$
$C^{10}(\theta)$	$(44/2^8 \times 4! \times 5!)\sin^8\theta$

Figure 2-6 shows the angular gain function for totally reflecting spheres at θ=10 degrees, following Kerker[4]. At this angle, there is considerable contribution from diffraction scattering. A comparison of this figure with Figures 2-1 through 2-3 will indicate that a given order polynomial approximation will be valid over a broader range of χ for smaller scattering angles.

Van de Hulst[3] has shown a comparison of angular gain functions versus scattering angle, between Mie theory for totally reflecting spheres and the diffraction theory of Equation (2-20). This comparison is presented in Figure 2-7 for a value of χ=3.

2.4 THE LOG NORMAL DISTRIBUTION

If we maintain the assumption that $\underline{I}_0$ has only one component, but return to the assumption that there is a multi-species particulate distribution, we have now obtained the following particular form for the linearized equations, last expressed in Equation (2-16).

$$\underline{J}^n = \frac{I_0}{4k^2}\,\underline{h}_i \cdot \underset{\sim}{C}^{in}$$

$$h_{qi} = \int_0^\infty d\chi\, n_i\,(\underline{p},\chi)\,\chi^{q+2}$$

$$\underset{\sim}{A}^n = \frac{I_0}{4k^2}\,\underset{\sim}{H}_i \cdot \underset{\sim}{C}^{in}$$

$$H^j_{qi} = \int_0^\infty d\chi\,(\partial n_i/\partial qj)\,\chi^{q+2} \qquad (2\text{-}22)$$

Here, the index i corresponds to the particulate species, and may be dropped if there is only one species, to obtain a similar equation to Equation (2-18). The $\underset{\sim}{C}^{in}$ are 2nd order tensors (matrices), consisting of the coefficients of polynomials chosen to fit the gain function at various angles. The computation of C^{i2} was discussed in the last section for two special cases. The $\underline{h}$ vector is of the same general form as the $\underset{\sim}{H}$ matrix, and can be considered as an augmented column vector.

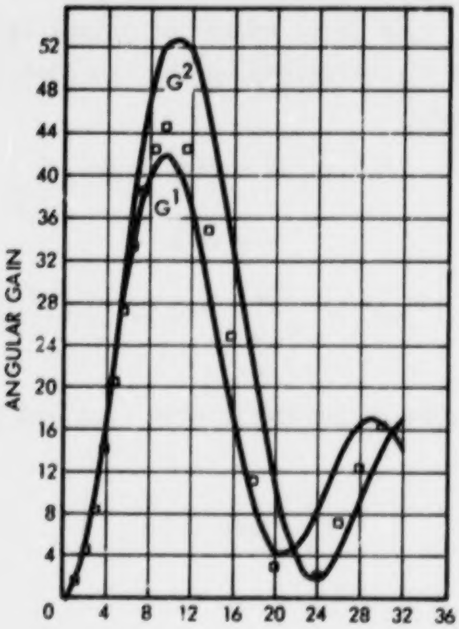

Figure 2-6. Angular Gain at θ = 10 Degrees for Totally Reflecting Spheres. Points designated by spuare are calculated according to diffraction Equation (2-20).

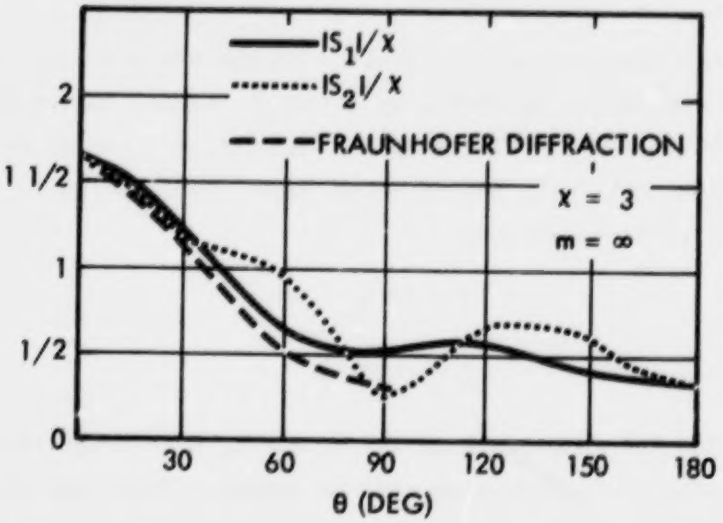

Figure 2-7. Scattering Diagram for Totally Reflecting Spheres in Each Polarization Mode. The comparison graph is as calculated from Equation (2-20).

The next task is to investigate some properties of the particulate distribution matrix $[\underline{H}, \underline{h}]$. A large number of naturally occurring polydisperse particulates are adequately described by the log normal distribution. This may be defined as follows:

$$n(\underline{p},\chi)\, d\chi = f(\underline{p},u)\, du$$

$$u = \ell n\, \chi$$

$$f(\underline{p},u) = \frac{n_o}{\sqrt{2\pi}\,\sigma} \exp\left[- (u-\bar{u})^2/2\sigma^2\right] \qquad (2\text{-}23)$$

The commonly-referred-to geometric mean size and geometric standard deviation are given by:

$$\chi_g = \exp\,(\bar{u})$$

$$\sigma_g = \exp \sigma$$

and the function f(u) is normalized so that

$$\int_{-\infty}^{\infty} f(u)\, du = n_o \text{ cm}^{-3}$$

Three strong choices for distribution parameters $\underline{p}$ are n_o, u and σ. The latter two are easier to work with directly, rather than geometric mean and standard deviation. The total number density, n_o, can be very large. To promote matrix uniformity and to speed numerical convergence, it is more convenient to use its logarithm.

$$\gamma = \ell n\, n_o$$

$$\underline{p} = (\gamma,\bar{u},\sigma)$$

In computing the components of the H matrix, nigh order integral moments of the f(p,u) distribution will be needed. These are simplified by using the following expression, wherein α is an integer exponent.

$$\chi^{\alpha} f(\underline{p},u) = E(\alpha,\underline{p})\; f(\underline{p},u)$$

where $$E(\alpha,\underline{p}) = \exp[\alpha\sigma^2(2u + \alpha\sigma^2)]$$

$$\underline{p} = (\gamma, u, \sigma)$$

$$\underline{p}' = (\gamma, u + \alpha\sigma^2, \sigma)$$

We can now evaluate the augmented H matrix given in Equation (2-22).

$$h_{qi} = n_{o_i} \, E(q+2, \underline{p}_i)$$

$$H^1_{qi} = n_{o_i} \, E(q+2, \underline{p}_i) \text{ for } \gamma_i$$

$$H^2_{qi} = n_{o_i} \, (q+2) \, E(q+2, \underline{p}_i) \text{ for } \bar{u}_i$$

$$H^3_{qi} = n_{o_i} \frac{(1+3\sigma_i^2 (q+2)^2)}{2\sigma_i} E(q+2, \underline{p}_i) \text{ for } \sigma_i \qquad (2\text{-}26)$$

Each of these expressions represents a column vector of component index q, for species i. Each has a common factor n_{o_i} which bears the same relationship to Equation (2-22) as the input intensity, I_0. The n_{o_i} depend on an absolute intensity measurement for their determination, but $\bar{u}_i$ and σ_i do not. If relative intensities are available at three different angles, the values of $\bar{u}$ and σ for a single species particulate may be solved directly from the first of Equation (2-26). This is due to the closed form analytic nature of the approximations we have made.

The factors $n_o \, E(q+2, \underline{p}_i)$ in Equation (2-26) can be expressed as a diagonal matrix multiplying the columns of a reduced matrix whose terms are algebraic. This leads to the following form for the $\underset{\sim}{H}$ matrix

$$\underset{\sim}{H}_{qi} = \delta^r_q \, \delta^j_i \left[1, r+2 \; \frac{1+3\sigma_j^2 (r+2)^2}{2\sigma_j} \right] \left[n_o \, E(r+2, \underline{p}_j) \right]$$

In this form, the resulting matrices are easily seen to be nonsingular for the general case.

The most sensitive factors in Equation (2-26) are the components of $E(q+2, \underline{p}_i)$. As can be seen from Equation (2-25), these are exponentially increasing functions of $(q+2)^2$ and σ^4. Thus, a moderate increase in the size range σ of a particulate distribution may mean many more terms are needed to obtain a good series approximation. Values of this function are shown plotted for comparison in Figure 2-8.

2.5 ESTIMATION OF DISTRIBUTION PARAMETERS FOR A SUB-MICRON PARTICULATE

In the last two sections, we have examined the $\underset{\sim}{C}$ and $\underset{\sim}{H}$ matrices of Equation (2-22) for some particular assumptions. Both matrices were found to carry full rank for the conditions investigated, and were thus nonsingular. We have, in a limited sense, proven the feasibility of solving the inverse problem for a sub-micron particulate by proving that the necessary conditions are met for a unique solution to exist. This is of course subject also to the validity of the conditions and approximations we made in showing that the matrices were nonsingular.

In setting out to choose these conditions and approximations, one is naturally influenced by the choice of data available. In the experimental portion of this program, the sub-micron particulate studied was tobacco smoke, which is known to have a distribution between approximately 0.01 and 1 micron, with a 0.1-micron geometric mean.[11] This leads to values of χ between approximately 0.05 and 5.

The three-coefficient scattering matrix derived in Section 2.3 for totally reflecting spheres is good only for values of χ less than about 2.0. This model was therefore not successful in describing the experimental data. The latter corresponded more to the shape of the gain curve for $\chi=3$, shown in Figure 2-7. The three-coefficient model seemed successful only in describing small-particle scattering, for $\chi<1$, and then only moderately so. The conclusion to be drawn is that more than three or four terms are needed in the power series expansion to be able to successfully extend it to values of χ of one or larger.

The leading coefficients in the power series expansion, the $\underset{\sim}{C}^{42}$, correspond to the Rayleigh scattering coefficients. For small, totally reflecting spheres the Rayleigh scattering gain functions are given by

$$G^1(\theta) = 4x^4(1 - \tfrac{1}{2}\cos\theta)^2$$

$$G^2(\theta) = 4x^4(\cos - \tfrac{1}{2})^2 \qquad (2\text{-}27)$$

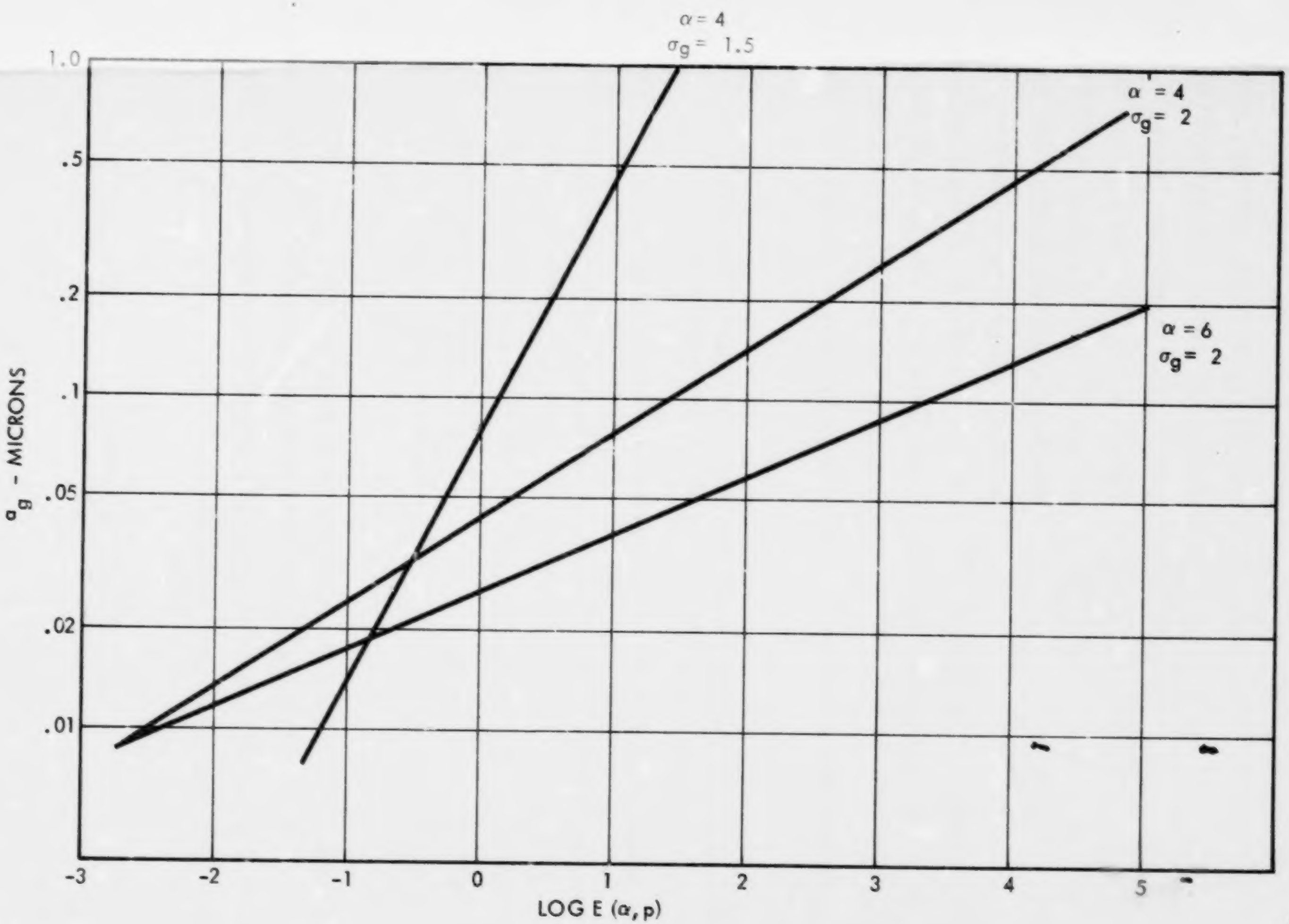

Figure 2-8. A Plot of the Function E (α,p), Showing the Sensitive Dependence on σ and α

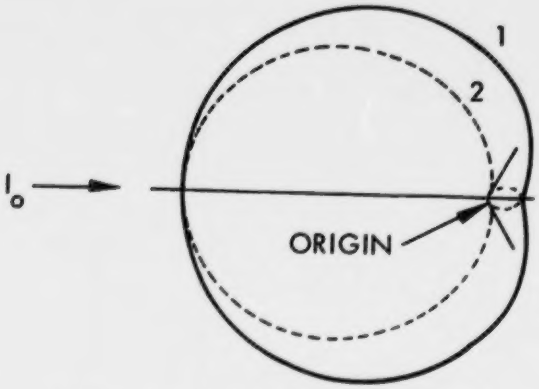

Figure 2-9. Scattering Diagram for Very Small Totally Reflecting Spheres. The scattering is predominantly back to the source.

The scattering diagram corresponding to Equation (2-27) is shown in Figure 2-9. The predominant backscattering for this configuration is clearly evident. The backscatter gain is nine times the forward scattering gain. The theoretical values of the C^{42} are just the coefficients of G^2 in Equation (2-27), for the various angles -- for example, 30, 90 and 150 degrees. These values, calculated from Equation (2-27), are shown in Table 2-3, where they are compared with the approximations of Section 2.3 [Table 2-1, Equation (2-19)].

Table 2-3. A Comparison of the Rayleigh Coefficients, C^{42}, For Polarization in the Scattering Plane

	Equation (2-9)	Equation (2-27)	Equation (2-28)
θ = 30°	0.05391	0.536	2.99
θ = 90°	1.220	1.00	0
θ = 150°	3.229	7.48	2.99

Equations (2-27) include the effects of both electric and magnetic dipole scattering. Classical Rayleigh scattering is derived assuming only an electric dipole contribution, when the dielectric medium is not strongly absorbing. The resulting gain function is

$$G^1(\theta) = 4x^4 \left| \frac{m^2 - 1}{m^2 + 2} \right|^2$$

$$G^2(\theta) = 4x^4 \left| \frac{m^2 - 1}{m^2 + 2} \right| \cos^2\theta \qquad (2\text{-}28)$$

If we assume a very large index of refraction again in this equation, the result is as follows

$$G^1(\theta) = 4x^4$$

$$G^2(\theta) = 4x^4 \cos^2\theta$$

The effect of assuming this form is also shown for comparison in Table 2-3.

If one is constrained to assume a Rayleigh-type distribution, then only one gain coefficient is available, only one element of the $\underset{\sim}{H}$ matrix need be computed, and only one distribution parameter can be estimated. Consequentially, only one data point is needed to estimate the chosen parameter. As a rule, however, sufficient data will be taken to verify the presence of Rayleigh scattering, and perhaps to be used in a least-squares estimation.

A Rayleigh scattering model can be used in conjunction with a log-normal distribution model to estimate any of the components of $\underset{\sim}{p}$ given in Equation (2-25), provided the remaining two are known or can be estimated from other sources. An alternative is to renormalize the $\underset{\sim}{H}$ matrix of Equation (2-18) in terms of an unknown geometric mean, X_g. Under these circumstances, the log-normal distribution has

$$u - \bar{u} = \ell n X - \ell n X_g = \ell n \, (X/X_g) = u'$$

and has an effective logarithmic mean of zero. In Equation (2-18), q=4 for Rayleigh scattering. The distribution and its moments remain integrable, and the coefficient $n_o a_g^6$ may be estimated in place of n_o. This is in sharp contrast to the estimation of $n_o a_g^2$ for the large sphere isotropic scattering model.[2]

Somewhat more successful results were obtained by applying the five-coefficient forward scattering model discussed in Section 2.3. With this model we were able to fit the data obtained from light scattering from tobacco smoke (Section 3.4). If the five-coefficient model of Table 2-2 is used to calculate the forward scattering gain function for X=3, the results agree with Equation (2-20) within 0.2 percent for all angles up to 30 degrees. A plot of the gain function is shown in Figure 2-7.

This model was used to obtain the linearized Equations (2-22) for several values of X_g and σ_g. The result for $X_g=3$ and $\sigma_g=1.1$ was found to agree closely with the shape of Figure 2-7. The results were convergent for values of X_g up to 10 and values of σ_g up to 2.0.

These calculations were made with a small computer program written in the BASIC language. This program is illustrated in Appendix B. Table 2-4 shows the results of such calculations for a geometric mean X_g of 1, and a geometric standard deviation σ_g of 1.7. The columns of $\underset{\sim}{H}$ and $\underset{\sim}{A}$ correspond to the parameter components of $\underline{p}$. The rows of $\underset{\sim}{H}$ are labeled according to coefficient powers of X, and rows of $\underset{\sim}{A}$ are labeled according to scattering angle.

The first column of the $\underset{\sim}{A}$ matrix in Table 2-4, corresponding to the n_o or X parameter, is the same numerically as the non-dimensional scattered light intensity distribution. This is evident from Equation (2-26). These values were computed for several scattering angles between zero and thirty degrees, for the same parameters, $X_g=1$ and $\sigma_g=1.7$. The results are shown in Figure 2-10.

Table 2-4. Components of the H Matrix for $X_g=1$ and $\sigma_g=1.7$, and Components of the Resulting $\underset{\sim}{A}$ Matrix Using the Forward Scattering Model of Equation (2-20). Components are normalized to $n_o=1$.

H Matrix	γ	$\overline{u}$	σ
X^2	3.5554	14.222	48.629
X^4	17.358	104.15	513.74
X^6	159.79	1278.4	8290.6
X^8	2773.8	27738	223390
X^{10}	90786	1089400	10491000
A Matrix			
10 degrees	3.428	13.47	44.94
20 degrees	3.099	11.58	36.13
30 degrees	2.686	9.389	27.16

Determinant: - 1.479

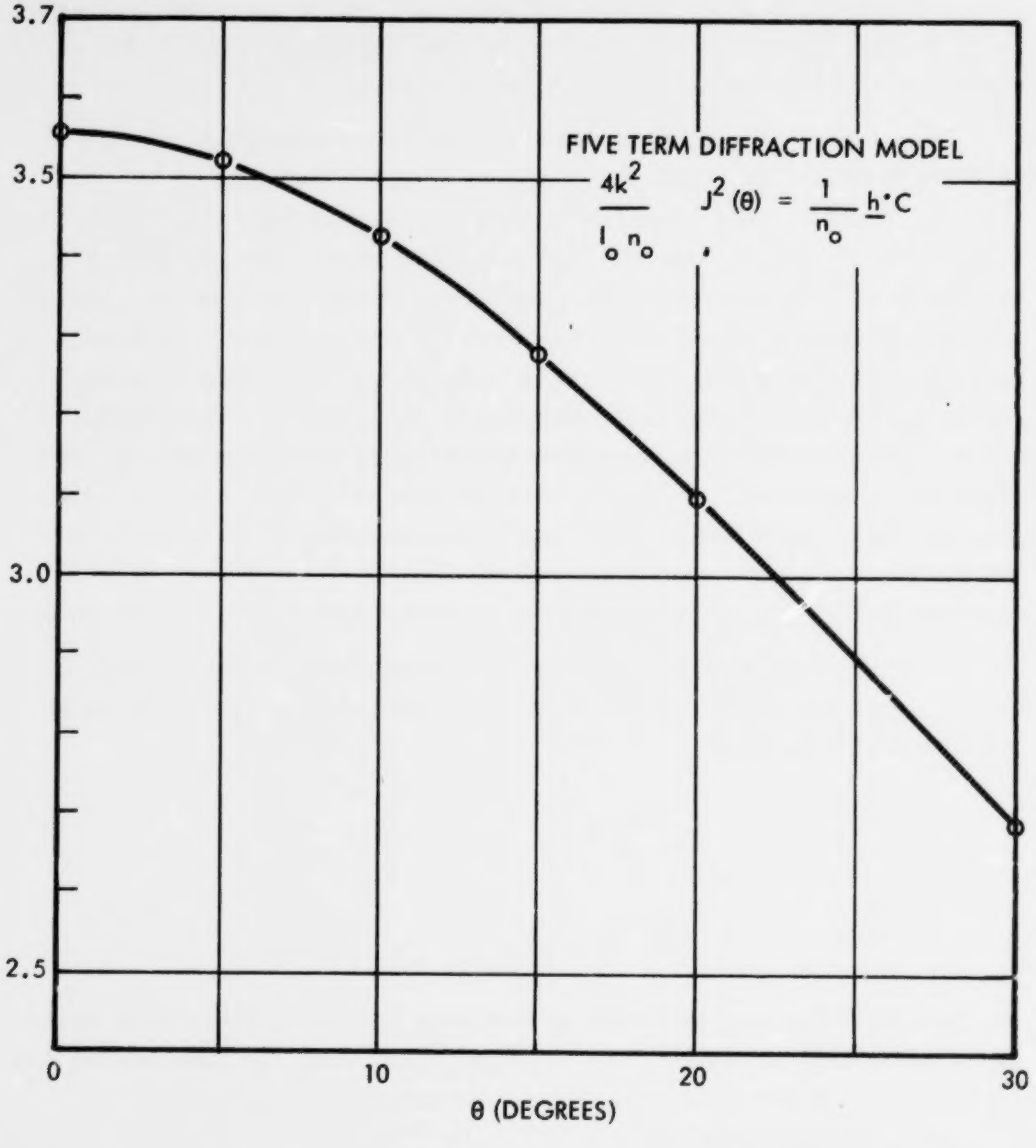

Figure 2-10. The Scattered Light Distribution for Particulate with $\chi g = 1.0$ and $\sigma g = 1.7$. Forward scattering computed with the five-term diffraction model of Table 2-2.

2.6 DISCRIMINATION BETWEEN TWO TYPES OF PARTICULATE

It is possible under certain limited conditions to distinguish between two different types of particulate in the same scattering medium. An example of how this may be done will now be derived.

The presence of multiple scattering species corresponds to the use of multiple values of the index i in Equation (2-22). Then each of the distribution functions and parameter vectors described by Equations (2-23) and (2-24) need also to be indexed. In the example chosen here, we start with two values of i in Equation (2-22), the value i=1 corresponding to a small particle Rayleigh scatterer, and the value i=2 corresponding to a large particle isotropic scatterer. We will then choose two different scattering angles θ_k, with k=1,2, and from these see if it is possible to estimate the two number densities n_{0i}, or alternatively the two number density logarithms γ_i. Log-normal particulate distributions will be assumed for both species, and in each case we will have to assume some a priori knowledge of average particulate size and distribution spread. If the $\underset{\sim}{A}^n$ matrix of Equation (2-22) is nonsingular, then a separate identification is possible.

We first write down the values of the scattering gain coefficients to be used. For the first species, there is a coefficient only of x^4, and we can obtain it from Equation (2-28).

$$C_k^{412} = 4 \left| \frac{m^2 - 1}{m^2 + 2} \right|^2 \cos^2\theta_k \tag{2-29}$$

$$C_k^{411} = 4 \left| \frac{m^2 - 1}{m^2 + 2} \right|^2$$

For the second species, we assume an isotropic scatterer with a total scattering efficiency of unity. This is often a good model for particulate with large X and back scattered light. The normalization criterion of Equation (2-6) shows that

$$C_k^{022} = 1.0 \tag{2-30}$$

This is the coefficient of X to the zero power, all other coefficients vanishing.

Next we compute the components of the $\underset{\sim}{H}$ matrix according to Equation (2-22). In this case, the components of the complete parameter vector $\underline{q}$ are simply the two number density logarithms γ_i, for i=1 and i=2. Then the integrand of the $\underset{\sim}{H}$ matrix has the partial derivative matrix $(\partial n_i/\partial\gamma_j)$, which is non-zero only for i=j. In this case.

$$H^i_{qi} = \int_0^\infty dX\, n_i(X,\underline{p}_i)\, X^{q+2} \qquad (2\text{-}30)$$

$$= n_{o_i}\, E(q+2,\underline{p}_i)$$

all other components of H^i_{qj} are vanishing. Furthermore, only the values for q=0 and q=4 are needed since these are the only non-vanishing coefficients in the $\underset{\sim}{C}^n$ matrix.

The vector $\underline{h}_i$, which gives the light intensity distribution, is the same as the first column vector of $\underset{\sim}{H}_i$. Performing the required sums over particulate species i and over powers of X^q, and considering only light polarized in the scattering plane, we first obtain the $\underline{J}^2$ vector.

$$J_k{}^2 = \frac{I_o}{4k^2}\left[4n_{o_1}\, E(6,\underline{p}_i)\left|\frac{m^2-1}{m^2+2}\right|^2 \cos^2\theta_k + n_{o_2}\, E(2,\underline{p}_2)\right] \qquad (2\text{-}32)$$

Because of the term in $\cos^2\theta_k$, the intensity is maximum for back scattering, and is a minimum but non-zero at θ=90 degrees. The model is not generally valid for forward scattering, since we have neglected diffraction effects of the large particulate.

With the matrix product $\underset{\sim}{H}:\underset{\sim}{C}$, again summed over i and q, we now obtain the $\underset{\sim}{A}^2$ matrix of Equation (2-22).

$$\underset{\sim}{A}^2 = \begin{bmatrix} 4n_{o_1}\left|\frac{m^2-1}{m^2+2}\right|^2 E(6,p_1)\cos^2\theta_1 & n_{o_2}\, E(2,p_2) \\ 4n_{o_1}\left|\frac{m^2-1}{m^2+2}\right|^2 E(6,p_2)\cos^2\theta_2 & n_{o_2}\, E(2,p_2) \end{bmatrix} \qquad (2\text{-}33)$$

Clearly, two scattering angles θ_1 and θ_2 may be found such that Equation (2-33) is nonsingular, and a distinction between n_{o1} and n_{o2} may be made. It is clear also from Equation (2-29) that if the $\underline{J}'$ vector were measured, light being polarized normal to the plane of reflection, Equation (2-33) would be singular, and no such distinction would be possible. Then for Equation (2-32) we would have a uniform $\underline{J}'$ distribution.

3. EXPERIMENTAL PROGRAM

The experimental objectives of the Task II program may be summarized as follows. A determination is to be made of the feasibility of holographically recording the scattered light signatures of airborne particulate down to 1-micron diameter in size. Either individual particles or an aggregate cloud of particulate are of interest. The feasibility of extending scattered light holography into the sub-micron size range is of interest. Finally, a determination of our ability to subsequently identify the particulate from the reconstructed holographic images is to be made. These objectives will be discussed in some detail in Section 3.1.

In Section 3.2, we will describe basic features of the test apparatus which was used. There were three basic test systems used. The first was a two-beam scattered light holocamera, hereinafter referred to as the Garrett holocamera,[12,14] which was developed on another program for the purpose of making holographic recordings of the flow field of an experimental fan turbine. This holocamera has a maximum included viewing angle of about 30 degrees, and effectively records light which is transmitted or scattered in the forward direction. It is easily adjustable to permit either bright field or dark field holography of a given scene. The second test system was a simple three-beam holographic apparatus using a point source scene, for the purpose of testing linearity and sensitivity of the holographic process. The third test system was a breadboard three-beam scattered light holocamera system with a three-plate holder designed to record light scattering over most of the range from 0 to 180 degrees scattering angle. This system included simple particulate generation devices for smoke and for water droplets.

Actual test procedures differed somewhat from those planned for reasons discussed in Section 3.3. Among the influencing factors were the availability for demonstration of the Garrett holocamera design and the desire to make a controlled test of two-beam and three-beam holographic process sensitivity. Progress with the three-beam scattered light holocamera was hampered by development difficulties related to the reference beam scatterballs.

Finally, in Section 3.4 we summarize and discuss the major results. These are briefly as follows.

With the Garrett holocamera, detection of particulate sizes down to 1 micron by forward scattering was demonstrated. It was visually apparent that some differentiation between particulate distributions was possible, at least in an unmixed state, by studying variation of light intensity with scattering angle. Although nothing basically new was learned, the method did demonstrate a consistently higher sensitivity by virtue of a lower noise-to-signal ratio than has previously been obtained.

The sensitivity of the holographic process was explored directly in terms of the ratio of scene light intensity to reference light intensity. This was found to be a significant parameter. A limiting value for this ratio of about 3×10^{-7} was found. Surprisingly, the second reference beam was not found to contribute significantly to the sensitivity.

The three-beam scattered light holocamera was therefore found to have merit only insofar as the third beam could be used as an intensity reference. A number of configurational changes were explored in order to try to use the holocamera to its best advantage in this mode. It was finally concluded that the best configuration to facilitate reconstruction and maintain linearity was one in which the reference beams were point sources at great enough distance from the holographic plate to provide a uniform intensity incident wave front.

Three-beam scattered light holograms were made of 30- and 50-micron water droplets obtained from a monodisperse droplet generator. Holograms were also obtained of a sub-micron tobacco smoke, and of mixtures of these two particulates. The two types of particulate were easily differentiable visually, and also from scattered light angular variation considerations. With the particular polarization mode chosen, the holocamera configuration was not sensitive enough to study side scattered light from sub-micron particulate. The forward scattered light, however, was found to be amenable to a size distribution analysis and was of sufficiently high intensity to seem preferable from sensitivity considerations.

3.1 EXPERIMENTAL OBJECTIVES

Experiments at TRW had previously verified our ability to make holographic recordings of small particulate by light scattering. Both individual particles (>15 to 20 microns) and clouds of micron-size particulate aerosols have been successfully recorded using this technique. Further, it was verified that particle number densities could be estimated from such recordings. To date, the limits of the scattered light holography techniques have not been fully established. The essential objective of the Task II program was to explore these limits. A brief summary statement of the objectives is as follows.

- Determine the feasibility of holographically recording the scattered light signature of airborne particulate down to 1-micron diameter in size. Either individual particles or an aggregate cloud of particulate are of interest.
- Determine the feasibility of extending scattered light holography into the sub-micron size range.
- Determine the feasibility of subsequently identifying the particulate from the reconstructed holographic images.

In pursuit of these objectives, and following the contractual work statement, the holographic process was studied with regard to the various effects of the following parameters and configurations.

Particle Size

This is perhaps the fundamental parameter of the whole study. The smaller the particle size, the more difficult it is to detect, and possibly less and less information about the particle is available from scattered light. The question of a lower useful size limit must be explored. Experience seems to indicate that, as a rule of thumb, anything that is photographically recordable is also holographically recordable. A comparison of techniques of scattered light holography for sub-micron particulate and for large particulate is of interest in order to see which problems are universal and which are a function of size. We therefore endeavored to make holographic measurements in each of four size ranges: (1) sub-micron, (2) 1 micron, (3) 10 micron and (4) 100 micron. Monodisperse particulate distributions were sought, and in one case used (30 to 50 micron water droplets).

Particle Number Density

Larger particle concentrations may be desirable since they will scatter proportionally more light intensity, and this is advantageous from a detection standpoint. Small particle size may be compensated for by large number density. On the other hand, large concentrations lead to increased liklihood of multiple scattering with consequent difficulties in modeling and interpretation. The program objective in this regard was to measure at least two number densities and evaluate their effects on light scattering.

Scattering Angle

The objective here was to measure as much as possible of the full range of forward, side and back scattering illumination of the particulate. This was achieved with some success using the three-beam scattered light holocamera, which simultaneously exposed three holographic plates at different orientations with respect to the scattered light. In this regard, forward scattered light has the property of being more intense and more easily recordable. Further, for relatively large particles, the forward scattering is primarily diffraction scattering and is independent of optical properties of the scattering medium. Under these conditions forward scattering is useful for obtaining size distributions for particulates with unknown index of refraction.

Side scatter is most sensitive to the internal structure of the scattering particles. However, net scattered light is also lowest in this direction.[1] Side scatter holography is worthy of consideration for two reasons. One reason is that for certain applications, physical restrictions limit one to side scatter techniques. Secondly, side scatter illumination of complex particles may offer the most sensitive means of detection and identification of particulates with complex optical structure and scattering properties. A possible example of this was given in Reference 1, where flyash from pulverized coal-fired combustion was found to consist partly of hollow spheres containing smaller internal particles.

Incident Beam Diameter

The tradeoff between the aerosol volume which can be holographically recorded and the particle size and number density has been studied. To state this problem in simple terms, the scattered light intensity falling on a film plate is an increasing function of each of these three parameters -- scene volume, particle size, and number density. The recordable scene light intensity depends on film sensitivity and on the ratio of scene light to reference light intensity. It was originally intended to study this aspect of the problem by using several (at least two) different incident laser beam diameters to probe the test aerosol. However, the same information was obtained and the intent of the work statement was satisfied by a study of the effects of emulsion sensitivity and scene to reference light intensity ratio.

Particle Velocity

In typical applications, particle velocities might range from very low values (1 to 2 ft/sec) up to perhaps 100 ft/sec, depending upon the duct or stack design and flow conditions. Hence, particle velocity is still another variable of interest. One must consider the velocity of the particles with respect to the stability of the holographic interference pattern for various holographic arrangements (i.e., forward, side and back scatter recordings). The worst case is the back scatter. Here, the limiting particle velocity is

$$v_b \leq \frac{\lambda/10}{2\tau}$$

where λ is the wavelength of the probing laser beam (~0.7μ) and τ is the duration of the laser pulse. As indicated in Section 3.2, 2-nanosecond laser pulses have been achieved at TRW Systems. With a ruby laser pulse of this duration, the limiting particle velocity for the back scatter condition is

$$v_b \leq \frac{0.7/10}{2(2\times10^{-9})} = 0.0175\times10^{9} \text{ microns/sec}$$

$$v_b \leq 1750 \text{ cm/sec } (\sim 60 \text{ ft/sec})$$

In other words, recording back scatter holograms of particles moving at velocities approaching 100 ft/sec is feasible provided a very short duration laser pulse is used.

The effect of particle velocity on holographic techniques is conveniently assessed by analytical means. The objective of the present study was to make this assessment while using a conventional 50-nanosecond laser to determine the limitation of the holographic technique with respect to the other variables discussed previously. Thus, only low velocity particles were studied. Velocity measurements were made, and the effect was determined to be minimal.

Three-Beam Holography

One of the objectives of this program was to explore the potentialities of this relatively new holographic test configuration. The name "three-beam holography" is derived from the presence of a scene beam and two reference beams. The two reference beams may be used interchangeably as reconstruction reference beams, if the configuration is properly chosen. The advantages were expected to be twofold.

In the first place, if one reference beam were chosen for reconstruction purposes, then the other would be available as a point source light intensity reference. Its intensity can be measured and compared to that of the incident scene light in the holocamera before any holograms are made. Then in the reconstructed hologram the ratio of reference light intensity to incident scene light intensity can be taken as the previously determined constant. In this way, a direct calibration is achieved for the ratio of scattered light to incident light intensity.

$$\frac{\text{scattered light}}{\text{incident light}} = \frac{\text{scattered light}}{\text{reference light}} \times \frac{\text{reference light}}{\text{incident light}}$$

The first intensity ratio on the right is measured from the hologram. The second is measured directly in the holocamera.

The second reference beam was also expected to result in an increase in the sensitivity of the holographic process. Preliminary investigation of this effect seemed to show that the fringe pattern obtained from the two reference beams had the effect of increasing sensitivity in recording scene light.[2] When the scene consists of weakly scattered light, it is desirable to reduce the reference light intensity correspondingly. Diminished light intensity at the hologram would result in adverse non-linear effects at the low end of the film emulsion characteristic curves. The presence of a second reference beam was intended to raise the exposure into the linear portion of the film characteristic. Outside of a tendency to reduce background light scattering from the hologram during reconstruction, no real effect of this sort was found during this program.

Two-Color Holography

This technique was considered as a possible approach to the program objectives, but time did not permit its use. In two-color holography, the output of the ruby laser is directed through a crystal of potassium dihydrogen phosphate (KDP). This crystal acts as a frequency doubler, and converts as much as 20 percent of the incident beam into light of half the wavelength. The output of the combination of the ruby laser and KDP crystal consists of both the primary red ruby radiation at 0.6943 micron, and the doubled ultraviolet radiation at 0.3471 micron. Either or both may be used to record a hologram of scattered light. The technique has been used to double the sensitivity of holographic interferometry.[13]

Since the size and intensity of the forward scattered light cone is sensitive to both particle size and incident wavelength, the two-color technique should make differentiation of particles of different size ranges easier. The use of two separate wavelengths gives each particle size "a" two different values of the parameter x=ka. (See Section 2.) Analysis is then possible over a large range of "a" while considering only a restricted range of x. Reconstructions of both the primary and secondary images can be obtained with a 0.6328-micron He-Ne laser, since the angular separation is great enough to view the two separately.

3.2 TEST APPARATUS

In the introductory remarks for this section we outlined three basic test systems which make up most of the experimental apparatus. In order of use, these were the Garrett scattered light holocamera, a three-beam sensitivity test breadboard holocamera, and a three-beam scattered light holocamera. Auxiliary units included the pulsed ruby laser system used for recording holograms of airborne particulate, and a monodisperse droplet generator which was used in conjunction with the three-beam scattered light holocamera.

Garrett Holocamera

The Garrett holocamera* was developed at TRW for studying the flow fields around the rotating blade rows of an aircraft fan turbine compressor. The holocamera is actually two separate holographic arrangements on a single frame, permitting the recording of bright field single and double exposure holograms (i.e., holographic interferograms), and dark field forward-scattered light holograms.[14] The two arrangements use much the same optics. The holocamera can be changed from one type of recording to the other by simple interchange of a few optical elements. Schematics of the two arrangements are shown in Figure 3-1. The lower diagram in Figure 3-1 shows the optical arrangement for recording bright field holograms (principally double exposure holographic interferograms). It is basically a "path-matched focused ground glass holocamera," similar to the ones first built to record holograms of liquid rocket fuel combustion.[15,16] The principles behind the design of this type of holocamera have already been elucidated.[17]

---

* Although the work subsequently described with the Garrett holocamera was not accomplished under this contract, it does constitute directly related technology. See Reference 14.

Of interest to the present EPA work is the scattered light holographic arrangement developed to record particulate in the flow field of the AiResearch fan turbine. The upper diagram in Figure 3-1 shows the scattered light arrangement in detail. Light from a pulsed ruby laser illuminator (typically 50-nanoseconds duration) is deflected into the holocamera by a prism reflector mounted below the tubular framework. The light is deflected vertically onto a glass wedge beam splitter which divides it into scene and reference beam components. The reference beam is the small (~4 percent) portion reflected from the first surface of the wedge. The scene component is the principal amount of light transmitted through the wedge (~92 percent). The beam is then incident on a second right angle prism reflector which directs it onto a third larger prism reflector. This then reflects the light toward the hologram. The prism is mounted for path adjusting reasons. The scene light is next focused through a pin hole aperture. Focusing of the pulsed laser beam with a positive lens was, in itself, a special development.* The pin hole blocked all light scattered by and from surfaces of the optics behind it; namely, the reflecting prisms, beam splitter, lenses, etc.

---

* Focusing of a Q-switched ruby laser beam with a positive lens leads to a phenomenon known as "air breakdown." The plasma formed at the focus of a lens is opaque to the laser beam. To prevent breakdown, a weak cylinder lens (0.5 diopter) was placed before the pair of focusing lenses. The combination produced an astigmatic pencil which reduced the electric fields below the breakdown threshold.

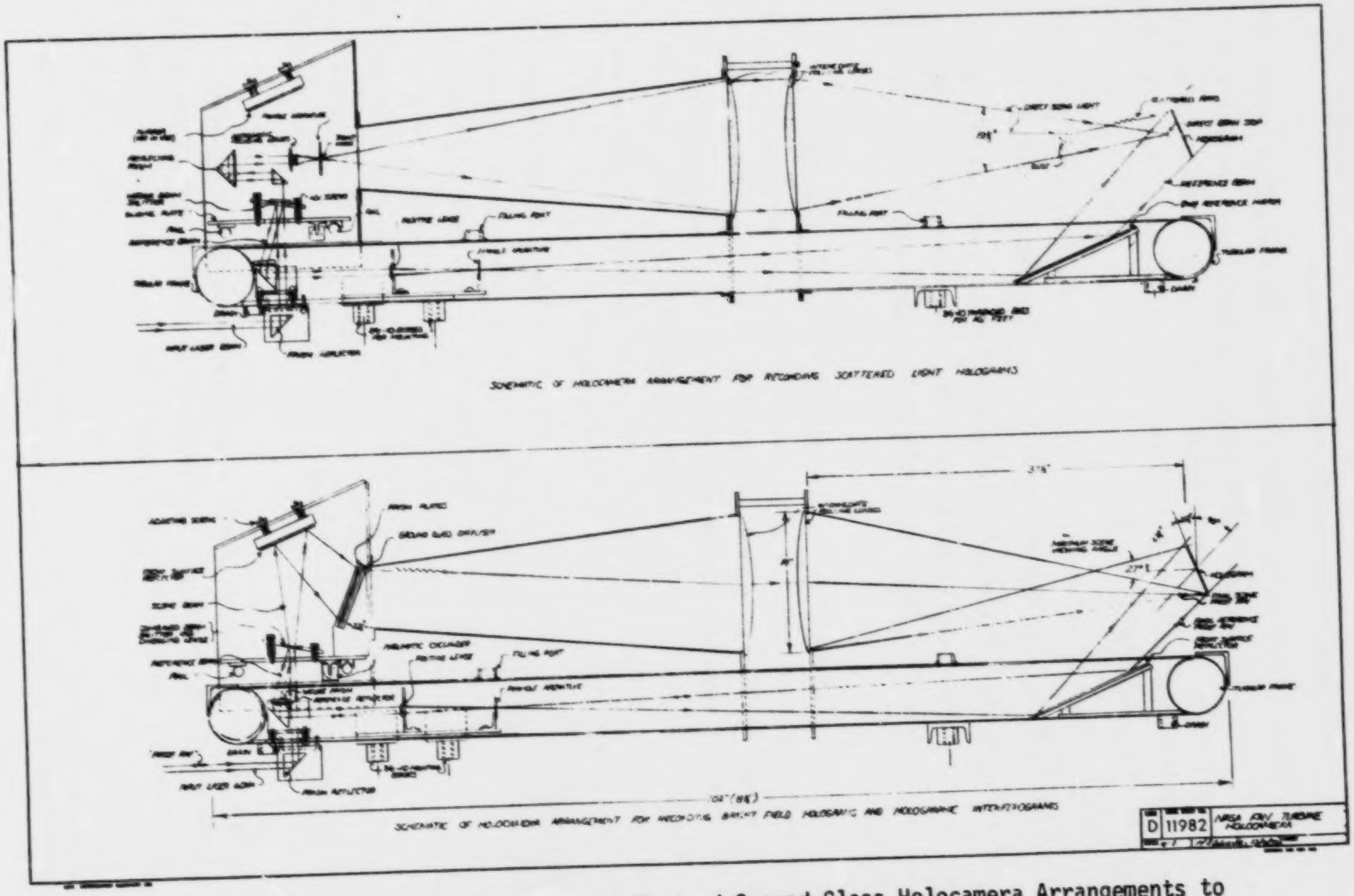

SCHEMATIC OF HOLOCAMERA ARRANGEMENT FOR RECORDING SCATTERED LIGHT HOLOGRAMS
SCHEMATIC OF HOLOCAMERA ARRANGEMENT FOR RECORDING BRIGHT FIELD HOLOGRAMS AND HOLOGRAPHIC INTERFEROGRAMS
D 11982
NASA FAN TURBINE HOLOCAMERA

Figure 3-1. Schematic Diagrams of Focused Ground Glass Holocamera Arrangements to Record Bright Field (Lower Diagram) and Dark Field (Upper Diagram) Scattered Light Holograms

The result is the creation of a single point source of light before the pair of 14-inch-diameter intermediate focusing lenses.

The intermediate focusing lenses refocused the light just before the hologram. A stop was mounted at the conjugate image point to absorb all of this light. Thus, the hologram received only light scattered from the surfaces of the intermediate focusing lenses (i.e., dirt) or from any other objects in the converging scene beam.

Particulate matter in this region scatters light in the forward direction, the arrangement for the most efficient scattering of light.

This scattering arrangement differs from earlier ones used by the writer in that light is convergent over a far wider solid angle. That is to say, the intermediate focusing lenses give a large scene volume for light scattering.

The reference beam, as noted earlier, is reflected from the first surface of the wedge beam splitter onto a wedge and prism reflector mounted in the base of the framework. These two elements direct the reference beam parallel to the framework, through a positive lens and second aperture,* onto a mirror which reflects the reference light onto the hologram. The reference beam is incident on the hologram at an angle of 45 degrees relative to the axis of the intermediate focusing lenses.

The beam splitter, two scene beam prism reflectors, the astigmatic focusing lens, and pinhole aperture were mounted on a platform, supported kinematically on horizontal rails. Also mounted on the same platform was the beam splitter diverging lens (a single plano-concave lens), prism plates, and ground glass diffuser of the bright field holographic arrangement. Sliding the plate sidewards converts the holocamera from the one type of recording to the other. A pneumatic cylinder was added for this purpose.

The two holographic arrangements were "breadboarded" before final construction. This was particularly important in the case of the scattered light configuration, where proper performance had to be verified by actual test. The bright field arrangement was also tested since it was a further simplification of the earlier focused ground glass holocameras.[15]

---

* An astigmatic lens combination is not needed in the reference beam leg since the intensity is below the breakdown threshold.

A photograph of the scattered light holographic breadboard is shown in Figure 3-2. Figure 3-3 shows a photograph of the completed holocamera.

Breadboard Sensitivity Tests

A three-beam breadboard holocamera was set up to test both the linearity and sensitivity of the holographic process. It is shown schematically in Figure 3-4. The optical components were placed on a large (242 by 152 by 21 cm) granite table (2 megagrams) mounted on vibration-isolation pads. A 15-milliwatt Spectra Physics Model 124 helium-neon laser was used as the illuminating source. Reference to Figure 3-4 shows that the laser beam is reflected from a mirror onto the first of two variable beam splitters (a Jodon VBA-200)*. Light reflected from this beam splitter is reflected from the two mirrors, which directs the resulting beam through a stack of attenuators and through a microscope objective. This beam, variable in intensity, is the scene beam. The objective spreads the scene beam across the hologram.

The portion of the initial laser beam which passes through the first variable beam splitter is next incident on a second identical variable beam splitter. Light reflected from this component is then reflected by a mirror which directs it through a Spectra Physics spatial filter. This element spreads the beam, uniformly illuminating the hologram. For the present discussion, this beam is the "first reference beam."

The component of light which passes through the second variable beam splitter is the "second reference beam." Like the first reference beam, it is reflected from a mirror and passed through a spatial filter (identical) to the one used for the first reference beam).

The two reference beams and the scene beam were set up so that their axes passed through one another at the hologram at angles of 30 and 45 degrees, respectively. That is to say, the first and second reference beams' axes were at an angle of 30 degrees. The first reference beam and scene beams' axes were at angles of 45 degrees. The angles were arbitrarily

---

* Rotation of the Jodon beam splitter about its axis allows one to continuously vary the intensity of the reflected and transmitted components.

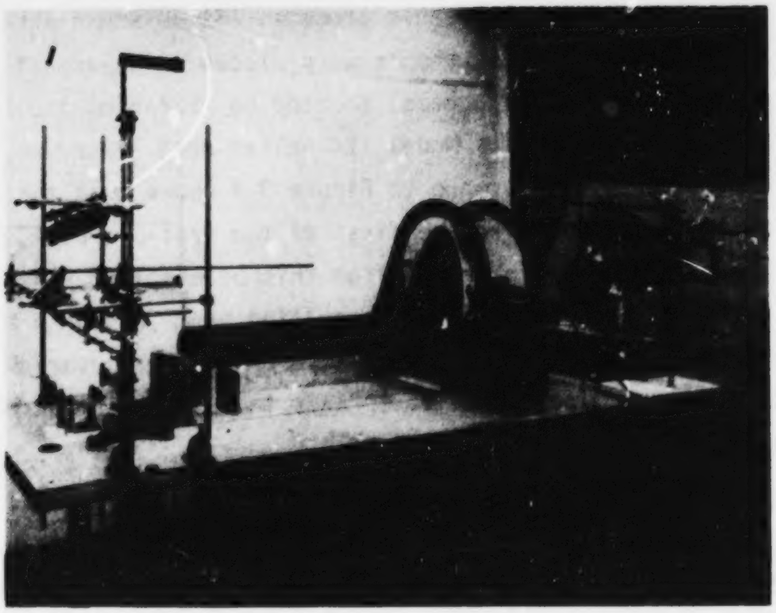

Figure 3-2. Photograph of Breadboard Scattered Light Holographic Arrangement Shown in Figure 3-1. Hologram is on far right, behind the model of a portion of the turbine fan. Before the fan is a nebulizer used to thrust larger particles in the scene volume.

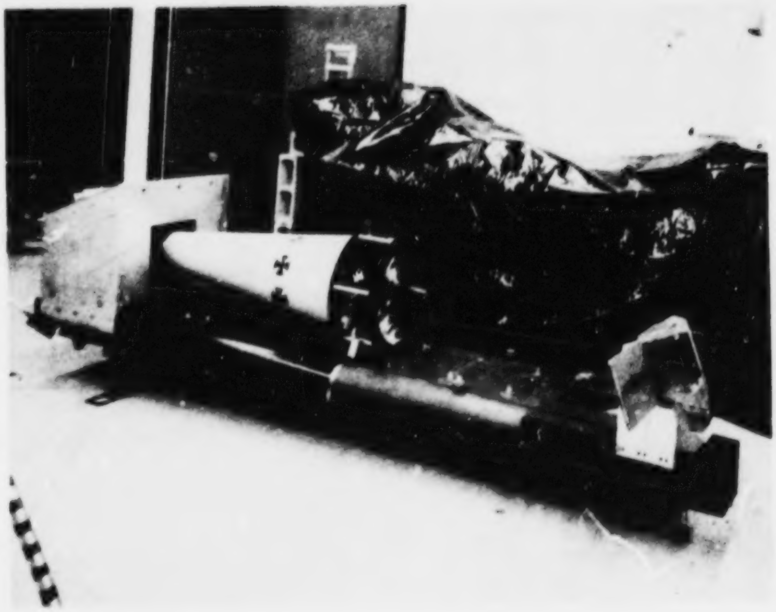

Figure 3-3. The Garrett Two-Beam Scattered Light Holocamera in its Completed Form. The scene volume is to the right of the large condensing lenses. To the right of that is the kinematic plate holder mounting. The beam forming optics are in the housing to the left. The beam enters from the underside. The whole camera sits on a water-filled ballast platform to provide stability.

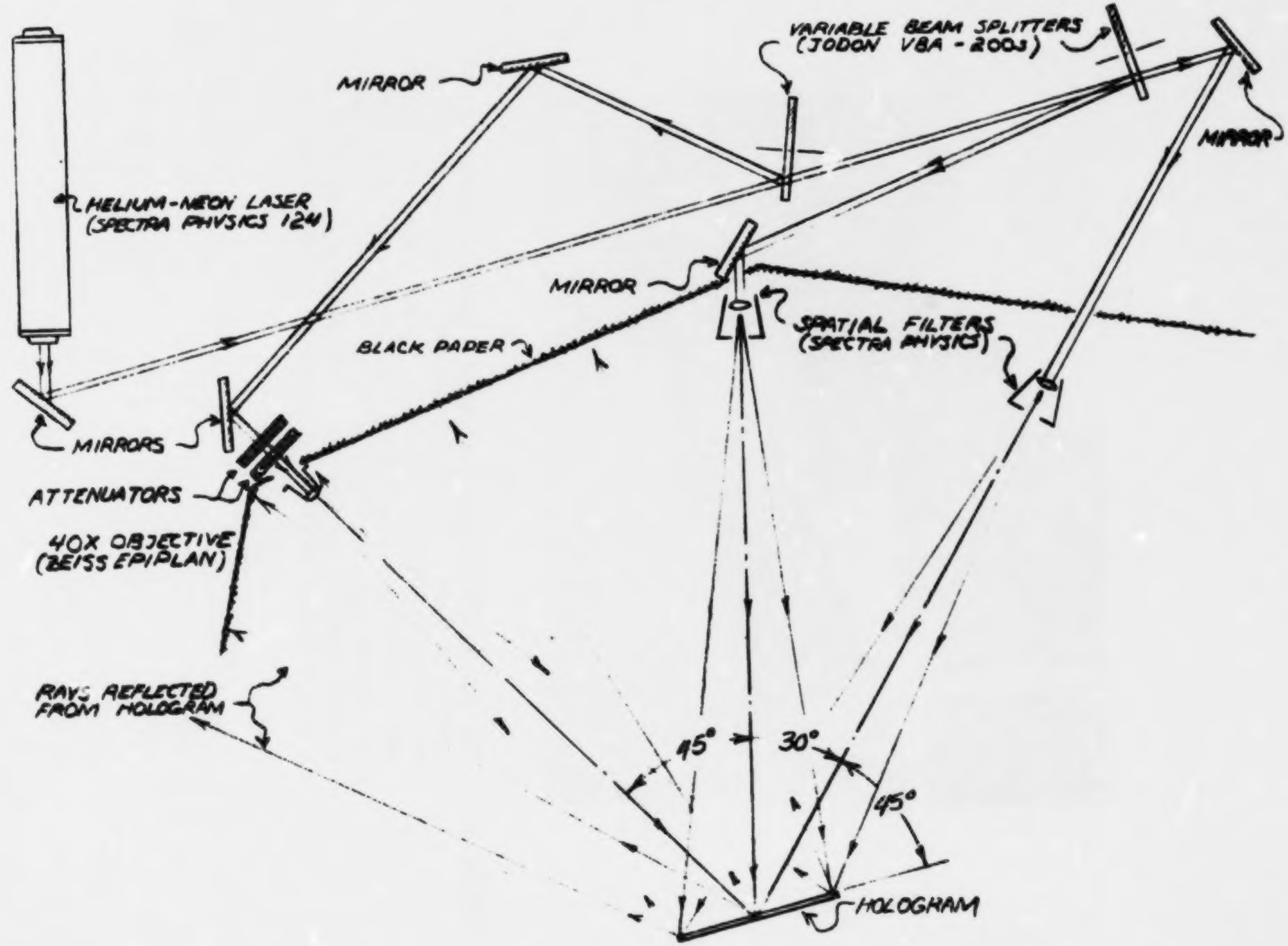
HELIUM-NEON LASER (SPECTRA PHYSICS 124)
MIRROR
VARIABLE BEAM SPLITTERS (JODON VBA - 200S)
MIRROR
MIRROR
SPATIAL FILTERS (SPECTRA PHYSICS)
BLACK PAPER
MIRRORS
ATTENUATORS
40X OBJECTIVE (ZEISS EPIPLAN)
RAYS REFLECTED FROM HOLOGRAM
45°
30°
45°
HOLOGRAM

Figure 3-4. Three-beam Breadboard Holocamera Used to Test Linearity and Sensitivity of the Holographic Process

chosen, not to be too large and such that the conjugate image reference beam (on reconstruction) did not appear close to the scene beam). Also, the second order reconstructed images did not appear near the reconstructed image of the scene beam.

The photographic plate or hologram was oriented relative to the three incoming beams so that the portions of the two reference beams reflected from its surface did not illuminate the front portion microscope objective which formed the scene beam, creating extraneous light signals. A little experimenting showed that this was possible with the surface of the hologram oriented at an angle of 45 degrees with respect to the axis of the second reference beam.

Black paper was placed between both the spatial filter, and the microscope objective and all of the other optical components. The paper barrier blocked the light scattered from the beam-forming components. As a result, the hologram "saw" (or was illuminated by) only three point sources of light — the two reference point sources and the scene, also a single point source.

Inspection of Figure 3-4 shows that by interchanging the microscope objective with the first reference beam, a three-beam arrangement with a weak scene beam between two strong reference beams is quickly created. This arrangement was tested after completion of tests with two reference beams proximate to one another. A telescope with a photomultiplier tube at the focal point was used to measure intensities.

Three-Beam Scattered Light Holocamera

A breadboard three-beam scattered light holocamera was designed with a three-plate holder designed to record light scattering over most of the range from about 5 to 175 degrees scattering angle. A perspective view of the holocamera is shown in Figure 3-5, and Figure 3-6 shows a layout drawing of the holocamera design.

The holocamera shown in Figure 3-5 utilizes a double reference beam and is designed to record ruby laser particulate light scattering over wide angles. Wide angle recording of the scattering is achieved by simultaneously exposing the three adjacent holograms. Each pair of adjacent holograms are positioned at an included angle of 120 degrees to each other.

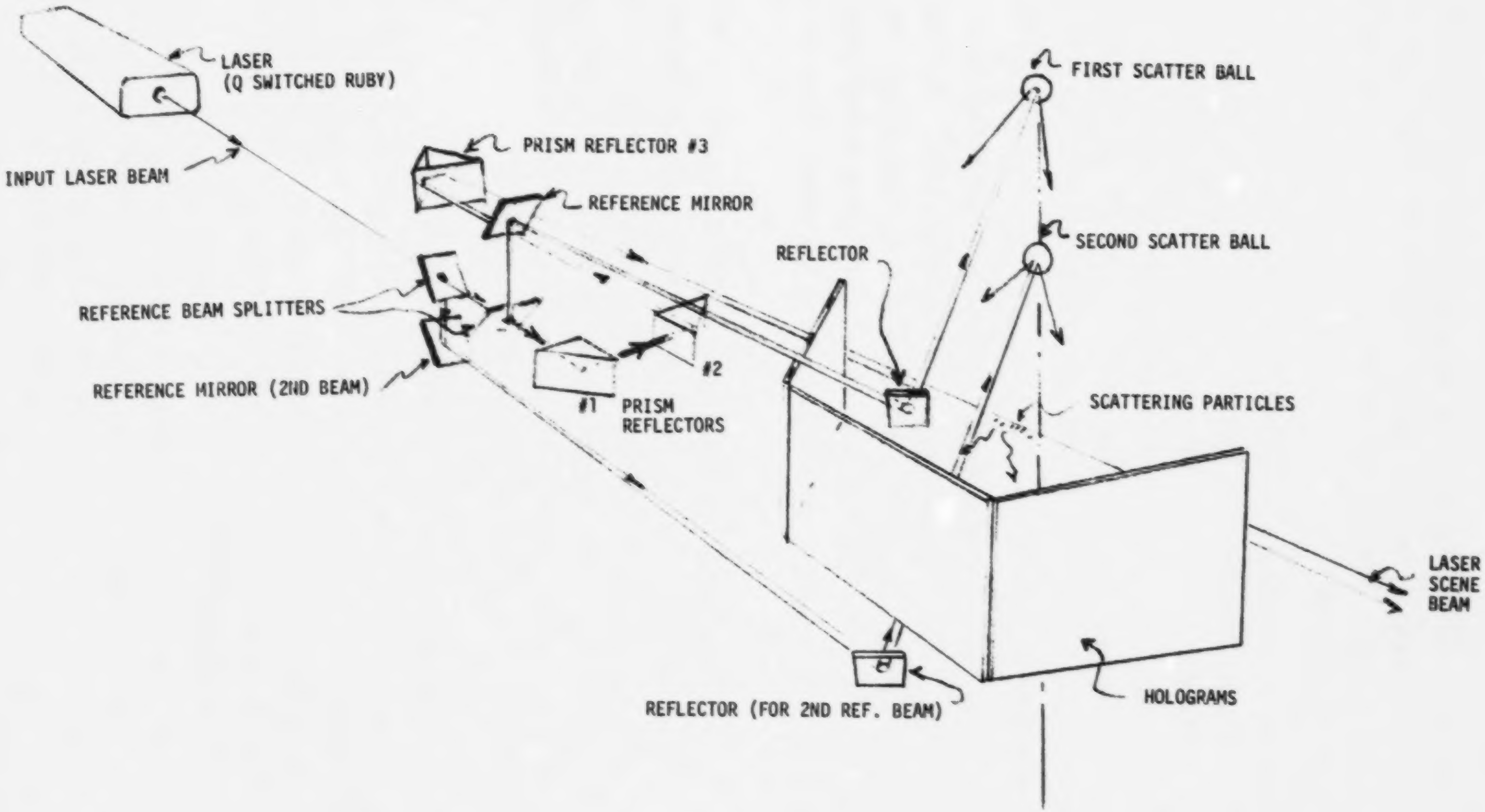
LASER
(Q SWITCHED RUBY)
INPUT LASER BEAM
PRISM REFLECTOR #3
REFERENCE MIRROR
REFERENCE BEAM SPLITTERS
REFERENCE MIRROR (2ND BEAM)
#1
#2
PRISM
REFLECTORS
REFLECTOR
FIRST SCATTER BALL
SECOND SCATTER BALL
SCATTERING PARTICLES
LASER
SCENE
BEAM
HOLOGRAMS
REFLECTOR (FOR 2ND REF. BEAM)

Figure 3-5. Perspective Sketch of Wide Angle Double Reference Beam Holographic Arrangement for Recording Scattered Light Holograms of Small Particles with Q-Switched Ruby Laser

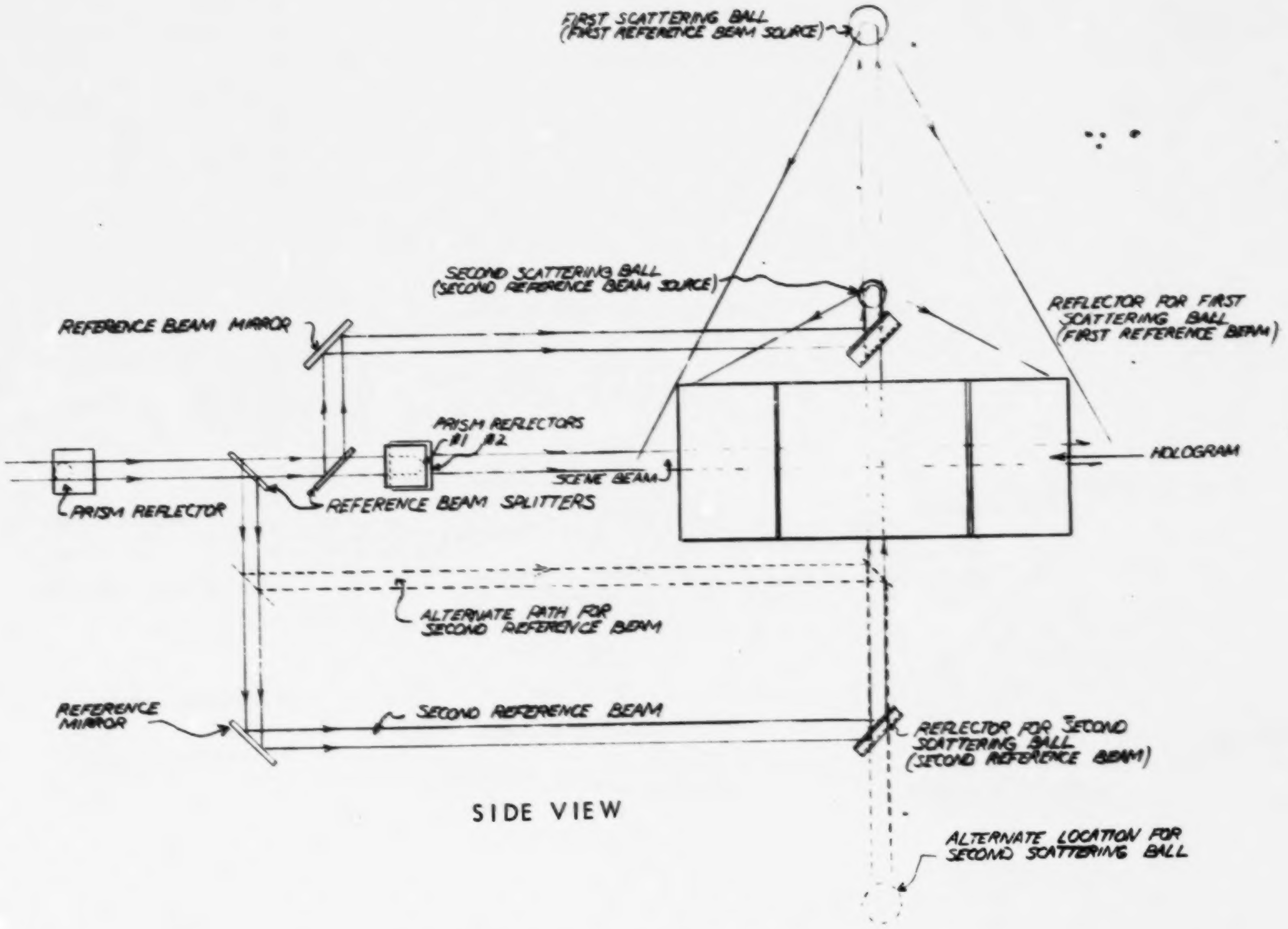
FIRST SCATTERING BALL
(FIRST REFERENCE BEAM SOURCE)
SECOND SCATTERING BALL
(SECOND REFERENCE BEAM SOURCE)
REFERENCE BEAM MIRROR
REFLECTOR FOR FIRST SCATTERING BALL (FIRST REFERENCE BEAM)
PRISM REFLECTORS
#1 #2
HOLOGRAM
SCENE BEAM
PRISM REFLECTOR
REFERENCE BEAM SPLITTERS
ALTERNATE PATH FOR SECOND REFERENCE BEAM
REFERENCE MIRROR
SECOND REFERENCE BEAM
REFLECTOR FOR SECOND SCATTERING BALL (SECOND REFERENCE BEAM)
SIDE VIEW
ALTERNATE LOCATION FOR SECOND SCATTERING BALL

Figure 3-6. Layout Drawing of Wide Angle Double Reference Beam Breadboard Holocamera

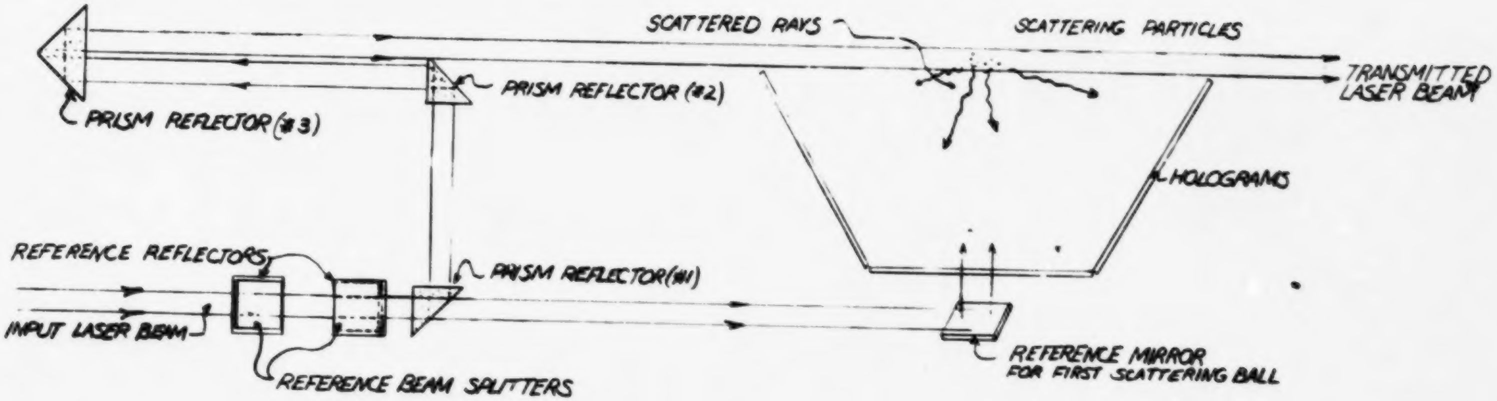
SCATTERED RAYS
SCATTERING PARTICLES
TRANSMITTED LASER BEAM
PRISM REFLECTOR (#2)
PRISM REFLECTOR (#3)
HOLOGRAMS
REFERENCE REFLECTORS
PRISM REFLECTOR (#1)
INPUT LASER BEAM
REFERENCE MIRROR FOR FIRST SCATTERING BALL
REFERENCE BEAM SPLITTERS

TOP VIEW

Figure 3-6. Layout Drawing of Wide Angle Double Reference Beam Breadboard Holocamera (Continued)

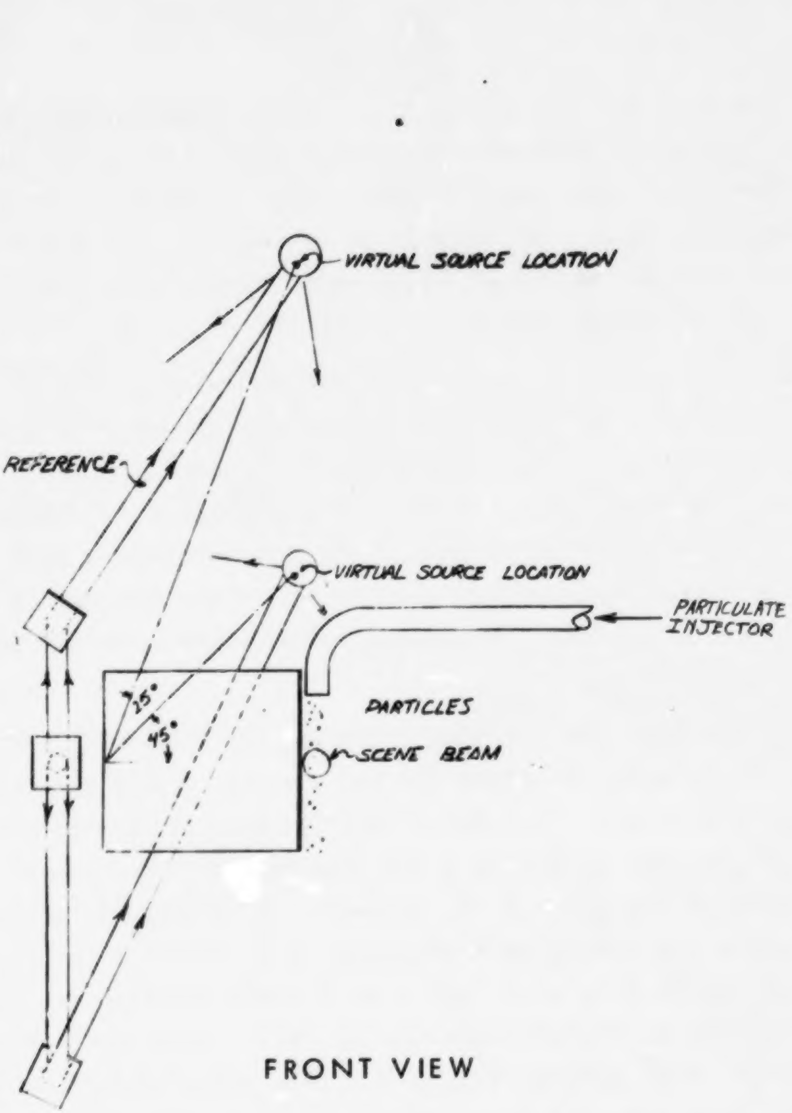
VIRTUAL SOURCE LOCATION
INITIAL REFERENCE
VIRTUAL SOURCE LOCATION
PARTICULATE INJECTOR
25°
45°
PARTICLES
SCENE BEAM
FRONT VIEW

Figure 3-6. Layout Drawing of Wide Angle Double Reference Beam Breadboard Holocamera (Continued)

The output of the pulsed ruby laser passes through a pair of wedge beam splitters. Reflected light from the beam splitters forms the two reference beams. Scene light transmitted through the glass wedges is directed into the scene volume with the aid of three prism reflectors. The incident scene light is not incident on any of the three holograms. The beam is directed past the edges of the two outside film plates.

Reference beams are derived from light reflected by the two glass wedges arranged in series. The first reference beam is formed at an elevation above the film plates using two first surface mirrors and a polished steel or coated glass scattering ball. The latter simultaneously illuminates the three holograms with reference light. The second reference beam is similarly formed except that the beam forming optics are arranged on a plane below the three holograms. The optical paths of the scene and reference beams are matched.

Figure 3-6 shows two alternate locations for the scatterballs. The preferred, first location is with the balls symmetrically located on either side of the film holder. The second location has both scatterballs on the same side of the film holder, as shown also in Figure 3-5. Both arrangements were tried during the experimental program. An additional configuration was tried which was similar to the first, only with the balls in closer to the center plane of the film holder and some distance out from it. This was to try and bring the scatterballs and the scattering particulate into the same field of view. Both polished steel, and gold- and silver-coated spherical glass lenses were tried for the scatterballs. The steel balls were 12.7-millimeter-diameter spheres. The glass lenses used were 10 millimeters in diameter, with a 10-millimeter focal length. A 15-millimeter diameter scene beam was used, and 15-millimeter reference beams were incident on each scatterball. In the final configuration, the path matching needed 18 centimeters from each scatterball to the center of each plate, and 12 centimeters from the scene to the center of each plate.

These variations in experimental procedure will be discussed further in Section 3.4.

The holocamera was originally intended to be oriented so that the scatterballs would be located above or below the film holder, on a vertical line, as indicated in Figure 3-5. In the final configuration the film holder and apparatus was rotated 90 degrees, for reasons of mounting convenience. The scatterballs were then both mounted below the film holder, on a horizontal line perpendicular to its center plane and the particulate stream was injected from left to right underneath the film holder.

The principal reconstruction angles chosen for the holograms were 30, 90 and 150 degrees, since these corresponded to the normals to the three plates.

Monodisperse Aerosol Generator

A vibrating orifice device for generating monodisperse aerosols, of the type described by Berglund and Liu,[16] was designed and fabricated and used in conjunction with the three-beam wide angle scattered light holocamera. Its use was directed toward determining our ability to discriminate between particulates of different size ranges. The basic components of the generator are an aerosol solution feed system, a 70-watt voice coil, and a 6.4-millimeter-long hollow stainless steel needle.

The vibrating orifice is the hollow needle, which has an ID of about 0.005 inch or 100 microns. The needle has a Luerlok fitting serving as an attachment to the feed system. A feed pressure of 520 to 750 torr (10 to 15 psi) produces a steady flow of aerosol solution to the orifice. The aerosol solution used was electronic grade isopropyl alcohol containing about 1 percent nonvolatile impurities (mostly water). The orifice is driven longitudinally with the 70-watt voice coil. The longitudinal vibration creates an instability in the fluid flow which causes the emerging liquid jet to break up into small, uniformly-sized droplets. The initial size of these droplets depends somewhat on the driving frequency, but more strongly on the orifice diameter.

The feed system is diagrammed in Figure 3-7. A 300-milliliter glass flask with a stopper and a tube insert serves as a reservoir for the aerosol solution. The flask is pressurized to 520 torr (10 psi) from air pressure reduced by a regulator and a pair of bleed valves.

The aerosol solution is forced through a feed line and through the hollow stainless steel needle by means of the 520 torr pressurization. The needle, or tube, has a 0.203-millimeter OD and a 0.127-millimeter ID (approximately 100 microns ID). The resulting aerosol flow is governed predominantly by the flow impedance of the needle. It was experimentally determined to be

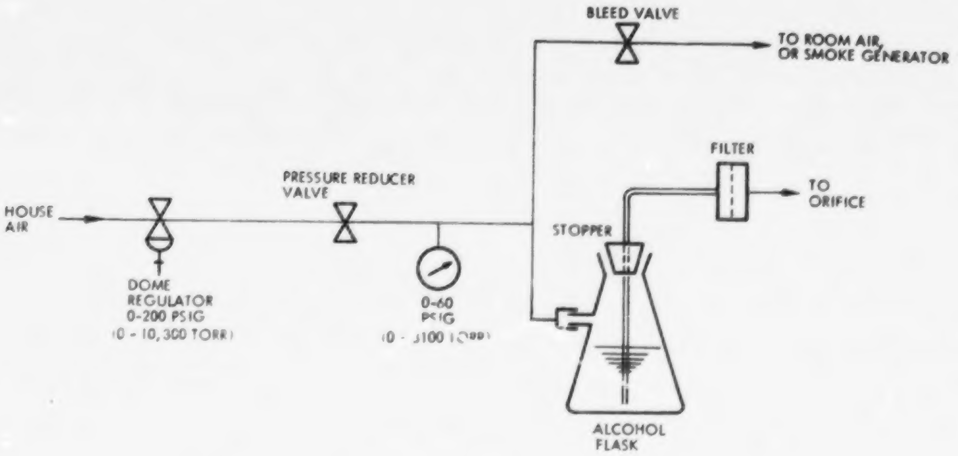
BLEED VALVE
TO ROOM AIR,
OR SMOKE GENERATOR
FILTER
TO
ORIFICE
PRESSURE REDUCER
VALVE
HOUSE
AIR
STOPPER
DOME
REGULATOR
0-200 PSIG
(0 - 10,300 TORR)
0-60
PSIG
(0 - 3100 TORR)
ALCOHOL
FLASK

Figure 3-7. Aerosol Solution Feed System

0.02 ml/sec at 520 torr feed pressure to within about 10 percent. Variations in flow rate are mostly due to dirt clogging the needle. This was alleviated by inserting a 10-micron Teflon Millipore filter in the feed line between the needle and the reservoir.

The method of mounting the needle orifice is illustrated in Figure 3-8. A conical stainless steel insert stiffens the voice coil and provides mass. The orifice is supported at the apex of a triangle formed of two stiff wires with the cone at its base. The orifice is held so that the driving force supplied by the speaker is longitudinal. The voice coil is driven by a Hewlett Packard signal generator with a 10-volt output and a 60-ohm internal resistance. Its output is amplified by a MacIntosh audio amplifier. The optimum frequency for the 100-micron orifice size is 3 kilocycles. The power input to the voice coil at this frequency is not critical, and was not measured, but it is known to be in the neighborhood of 20 watts.

The liquid aerosol generator was operated in conjunction with a simple forced air smoke generator, consisting of a cigarette holder and a duct to direct the smoke upstream. The air flow through the burning cigarette was obtained directly off the droplet generator pressure manifold, as shown in Figure 3-7.

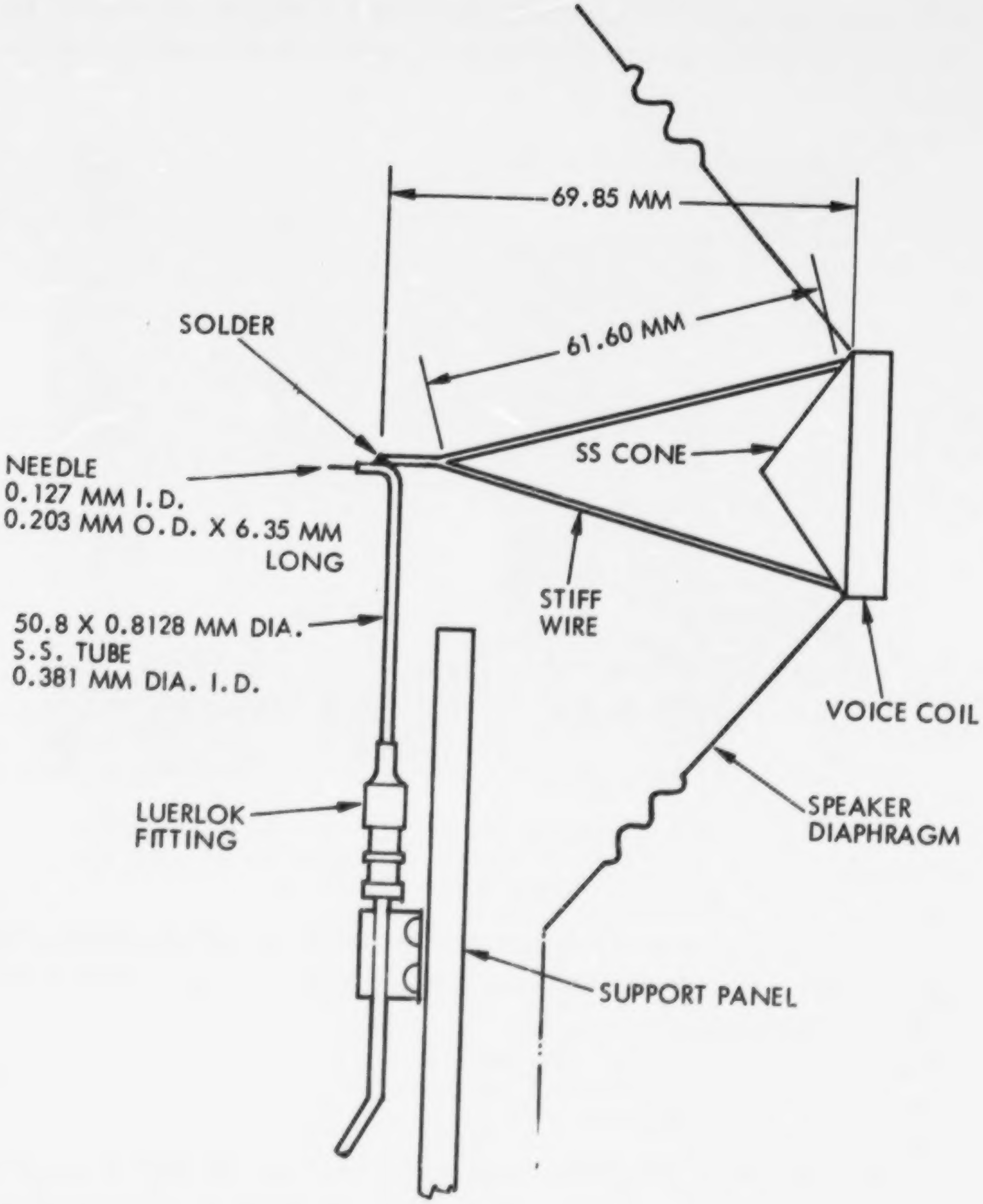
69.85 MM
61.60 MM
SOLDER
NEEDLE
0.127 MM I.D.
0.203 MM O.D. X 6.35 MM LONG
SS CONE
STIFF WIRE
50.8 X 0.8128 MM DIA.
S.S. TUBE
0.381 MM DIA. I.D.
VOICE COIL
LUERLOK FITTING
SPEAKER DIAPHRAGM
SUPPORT PANEL

Figure 3-8. Voice Coil and Aerosol Generator Orifice Mount

Figure 3-9 shows the droplet generator mounted in conjunction with the three-beam wide angle breadboard holocamera. In the picture are seen the voice coil, the aerosol liquid flask and filter, the pressure plenum, the MacIntosh amplifier, the three-plate film holder and the reversing prisms.

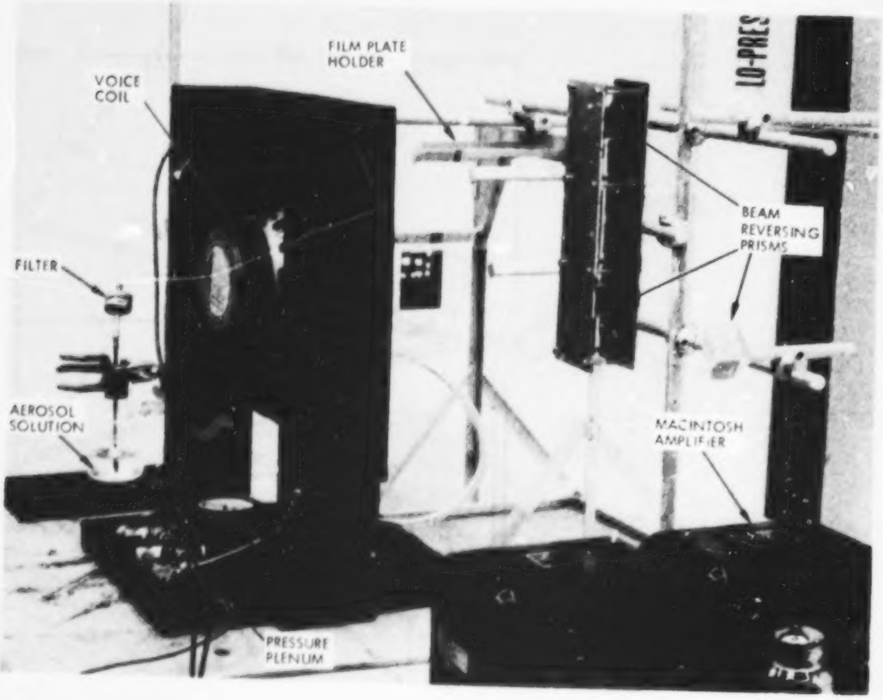
FILM PLATE HOLDER
VOICE COIL
LO-PRES
BEAM REVERSING PRISMS
FILTER
AEROSOL SOLUTION
MACINTOSH AMPLIFIER
PRESSURE PLENUM

Figure 3-9. Breadboard Three-Beam Wide Angle Scattered Light Holocamera With Monodisperse Aerosol Generating System (101119-73)

The droplet generator operates at frequencies around an optimum frequency given by the flow velocity divided by a wavelength. The wavelength is found experimentally to be[16]

$$L_{opt} = 4.508\ D \qquad (3\text{-}1)$$

Here, D is the jet diameter and may be taken as the same as the orifice ID, 100 microns. The optimum wavelength has also been calculated theoretically. The results were similar to Equation (3-1). The flow velocity is related to volumetric flow rate, Q, by

$$Q = \frac{\pi}{4} D^2 v \qquad (3\text{-}2)$$

The droplet diameter at the optimum frequency is then given by

$$a = \sqrt{\frac{6Q}{\pi\nu}} \tag{3-3}$$

A rather wide variation in frequency around the optimum for a given flow rate is possible. Droplets of uniform size were formed, for example, at a frequency as high as 9 kc. The droplet formation instability mechanism is ineffective too far above or below the optimum frequency.

The above equations give a flow velocity of 158 cm/sec for a flow rate of 0.02 cc/sec. The diameter of the droplets thus formed, before any evaporation occurs, is 240 microns. This diameter is found to be independent of flow velocity at the optimum frequency, since both ν and a have a factor of ν which cancels out in Equation (3-3). Droplet diameter thus depends mainly on orifice diameter, and can be varied only insofar as the frequency can be tuned away from the optimum.

Once the droplets were formed, the alcohol in the aerosol solution evaporated very radidly, leaving only water droplets. Complete evaporation of the alcohol should leave a water droplet of a diameter reduced by a factor of the cube root of the original water concentration. This is a factor of about 0.22, and the predicted water droplet diameter is thus 53 microns.

The aerosol thus formed was illuminated with a 15-milliwatt beam from a He-Ne laser. Interference rings of diffracted light were observed, the outer maximum of which occurred at an angle of about 35 degrees from the incoming laser beam. The interference fringes are caused by internally reflected light from the droplets, following an optical path illustrated in Figure 3-10. For a given fringe angle θ, there exist two incident light paths corresponding to two different values of β. Light from these paths interferes either constructively or destructively. Interference fringes were located at values of $\tan\theta$ of 0.7, corresponding to the 35-degree outer fringe, and then at 0.660 and 0.642. Analysis of the fringe spacing gave the droplet diameter. The value obtained was 50 microns. The nonlinear equations and their solution are illustrated in Figure 3-11.

Pulsed Ruby Laser Illuminator

The source of illumination for the holocameras was a pulsed ruby laser system designed and built at TRW Systems Group. Photographs of this solid-

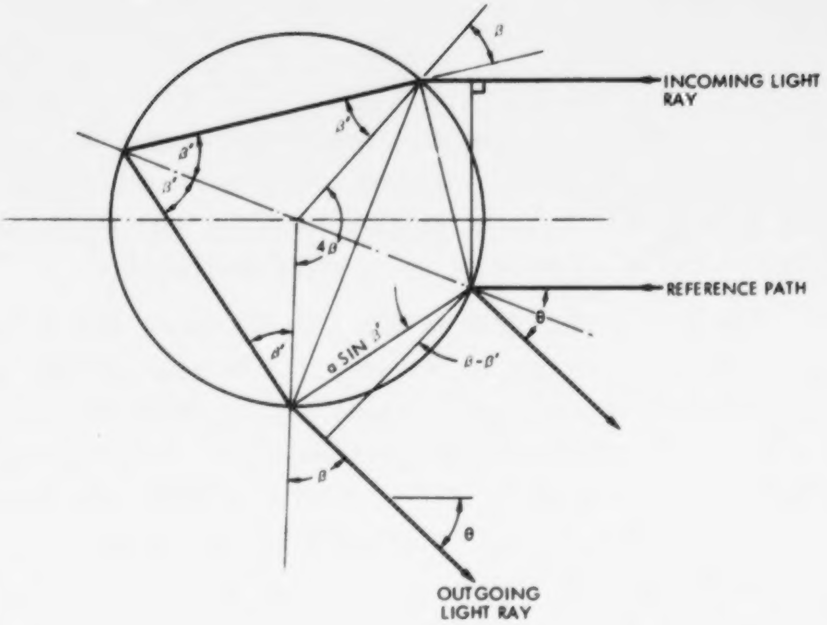
β
INCOMING LIGHT RAY
β''
β''
β'
4β
REFERENCE PATH
θ
β''
a SIN β'
β - β'
β
θ
OUTGOING LIGHT RAY

Figure 3-10. Geometry of Internally Scattered Light From a Liquid Aerosol Droplet of Diameter a

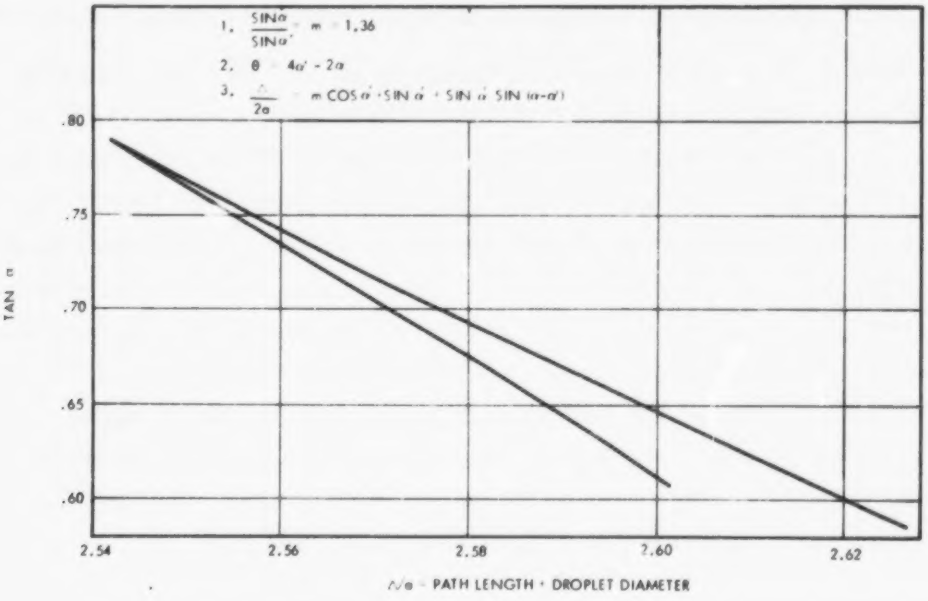

Figure 3-11. Nonlinear Diffraction Equations for Light Internally Reflected From a Sphere and the Two Branches of Their Solution

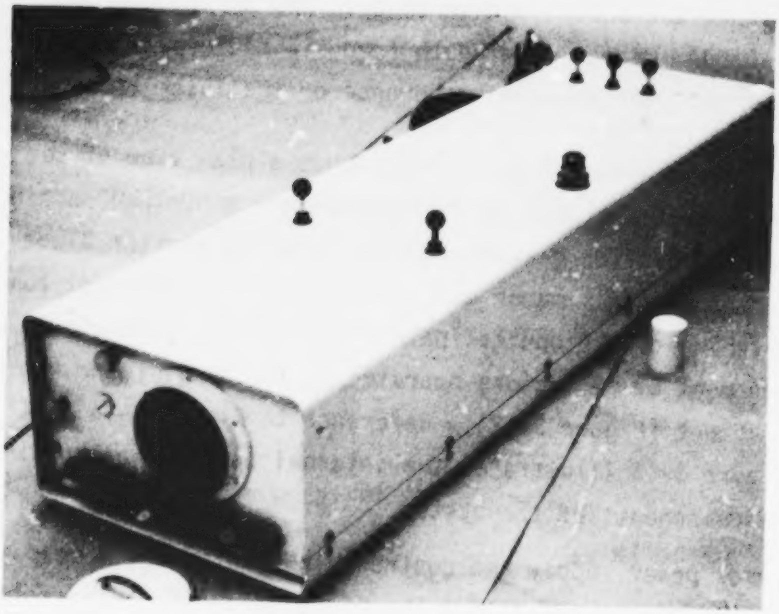

Figure 3-12. TRW Q-Switched Ruby Laser Illuminator

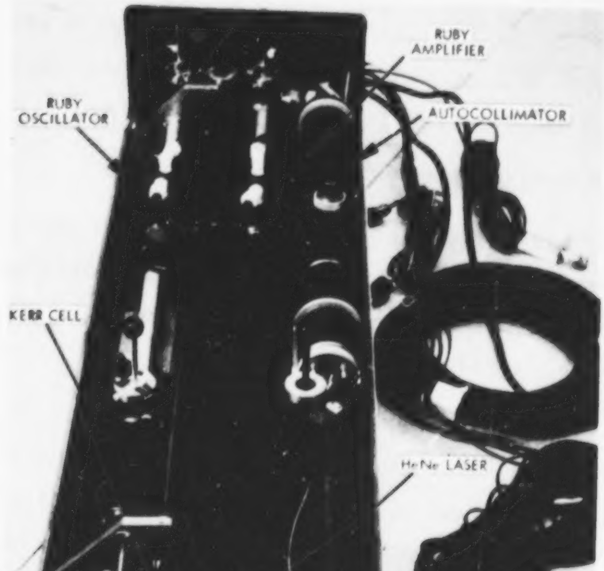
RUBY AMPLIFIER
RUBY OSCILLATOR
AUTOCOLLIMATOR
KERR CELL
HeNe LASER

Figure 3-13. Ruby Laser Illuminator With Cover Removed to Show Location of Major Components

state ruby laser are shown in Figures 3-12 and 3-13. The laser emits 1 to 3 joules of 0.6943 micron wavelength (red light) in pulses of 30 to 50 nanoseconds duration. The temporal coherence of the laser is about 5 centimeters.

A schematic diagram, Figure 3-14, shows a plan view of the components in the ruby laser. Included in the package are a "folded" arrangement of the oscillator-amplifier Q-switched ruby laser, a monitor diode, a dark-field alignment autocollimator and a helium-neon directional pointing gas laser. Switching of the optical path among these components is accomplished by an arrangement of reflectors operated by the small round knobs on top of the laser cabinet (Figure 3-12). Reference to Figure 3-14, and the photograph of Figure 3-13 illustrates the internal optical path of the laser and the various components of the system.[16]

The laser power supply and control electronics are housed in separate consoles as seen in Figure 3-15. The right-hand console contains two ignitron-fired 0 to 5 kv, 375 μF capacitor banks used to energize the helical Xenon flash lamps in the ruby oscillator and amplifier assemblies of the laser. The comparison console contains the independent high voltage supply and control circuits for the Kerr cell Q-switch. Also shown in Figure 3-15 is a Tektronix Type 535A oscilloscope used to record the ruby oscillator output energy monitored by the integrating photodiode.

3.3 EXPERIMENTAL PROCEDURES

Test methods and analytical methods were chosen which would accomplish all the objectives set forth in Section 3.1 as expeditiously as possible. The choice of methods was also governed by the need to make best use of currently available facilities.

When the Garrett holocamera was under development on a separate contract,[14] it became available for test work which was directly related to this program. This afforded a good opportunity to test an optimum, two-beam scattered light holocamera design in the sensitive forward scattering regime. The scattering angles which could be visualized were between 0 and 15 degrees.

In order to test the effects of the particulate size variable and variable optical properties, three different types of particulate were used. These were phenolic and glass micro-ballons, and incense smoke. The effects of these three size ranges will be discussed further in Section 3.4.

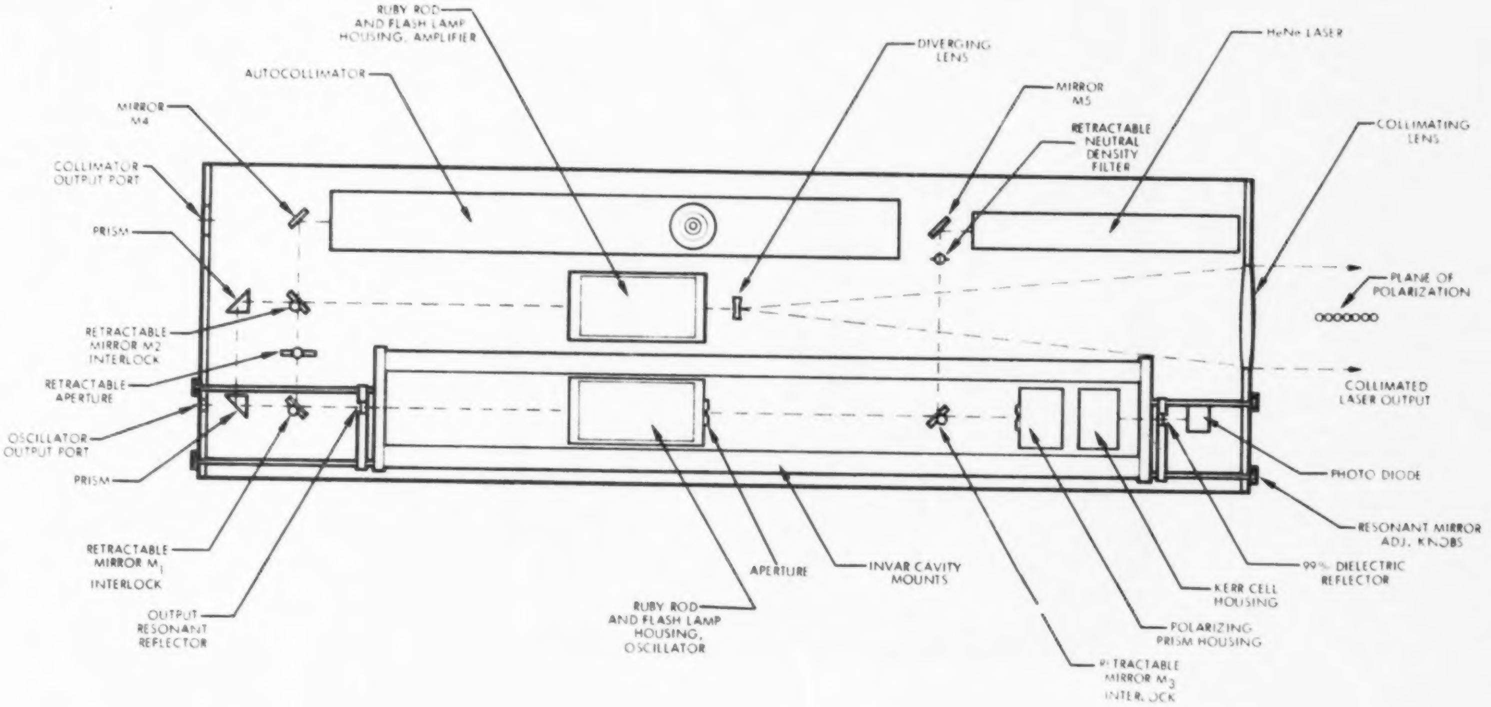
RUBY ROD AND FLASH LAMP HOUSING, AMPLIFIER
AUTOCOLLIMATOR
MIRROR M4
COLLIMATOR OUTPUT PORT
PRISM
RETRACTABLE MIRROR M2 INTERLOCK
RETRACTABLE APERTURE
OSCILLATOR OUTPUT PORT
PRISM
RETRACTABLE MIRROR M1 INTERLOCK
OUTPUT RESONANT REFLECTOR
DIVERGING LENS
MIRROR M5
RETRACTABLE NEUTRAL DENSITY FILTER
HeNe LASER
COLLIMATING LENS
PLANE OF POLARIZATION
COLLIMATED LASER OUTPUT
PHOTO DIODE
RESONANT MIRROR ADJ. KNOBS
99% DIELECTRIC REFLECTOR
KERR CELL HOUSING
POLARIZING PRISM HOUSING
RETRACTABLE MIRROR M3 INTERLOCK
INVAR CAVITY MOUNTS
APERTURE
RUBY ROD AND FLASH LAMP HOUSING, OSCILLATOR

Figure 3-14. Schematic Diagram of Compact Ruby Laser Illuminator

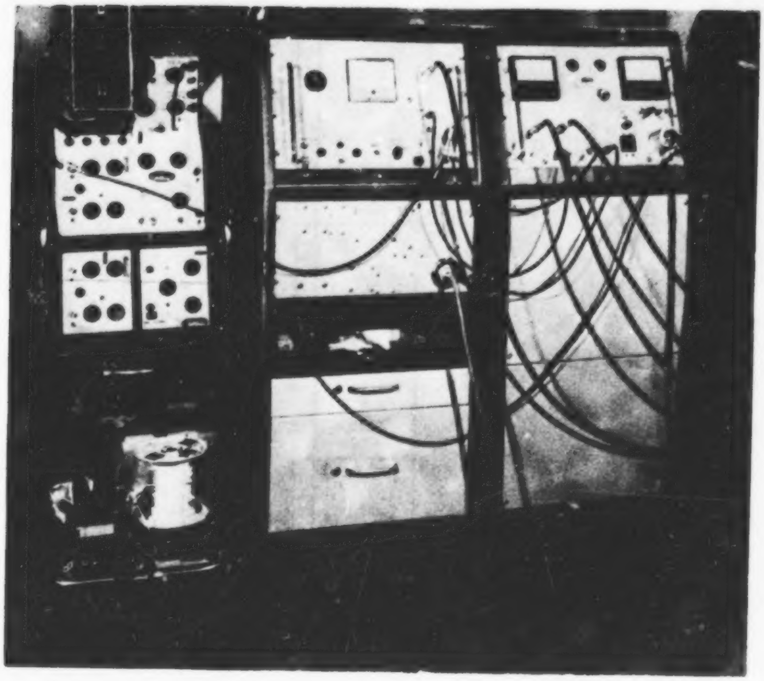

Figure 3-15. Photograph of TRW Pulsed Ruby Laser Power Supply Consoles and Tektronix 535A Oscilloscope

The glass micro-balloons were in the 30 to 50 micron size range. The phenolic particles were slightly larger, but more important was their tendency to agglomerate into macro-particles of several hundred microns diameter. The incense smoke was in the 1 to 3 micron size range.

The micro-balloon particulate was thrust into the scene volume with a forced air nebulizer. The incense smoke was wafted into the scene volume by convection. In neither case were velocity measurements made, but the velocities were low, on the order of several feet per second or less. No attempt was made either to measure particle number density in the three size ranges. However, the effect of scattering angle on light intensity was visually apparent.

The need to establish a quantitative relationship between the recorded aerosol volume, the particle size and number density and the recordable scattered light intensity led to the development of a simple three-beam holographic apparatus for intensity sensitivity testing. This apparatus was described in Section 3.2.

As previously discussed in Section 3.1, the light intensity scattered from an aerosol and onto a holographic plate is an increasing function of incident beam intensity, recorded scene volume, particle size and number density. The recordable scene light depends on film sensitivity and on the ratio of scene light to reference light intensity.

It was originally intended to study this effect by using a beam expander and collimator lens to vary the diameter of the laser beam incident on the aerosol. The laser beam contains a given amount of power and expanding the beam merely spreads this power over a larger area. The power density is less, but it is incident on proportionally more particulate. Thus if the particle number density was, on the average, constant through space, the total scattered light intensity should remain independent of incident beam diameter. The advantage would not be from increased scattered light intensity, but from an ability to study spatial density fluctuations within a larger volume of aerosol, or perhaps obtain a more extensive spatial averaging of particle density.

Particulate scattering in the Garrett holocamera (forward scattering) was recorded with an expanded beam, with a diameter of order one meter. The three-beam wide angle breadboard holocamera used an unexpanded beam of approximately a diameter of 1.5 centimeters. These two-beam diameters afforded some information on our ability to study spatial variations. However, a more definitive study of the effects of aerosol size, density, etc., on scattered light intensity and our ability to record it was made with the three-beam apparatus set up specifically for that purpose. Studies were made of the effects of film sensitivity, and of the use of both single and double reference beams. A lower limit for the required ratio of scene light to reference light intensity was found, and this limitation was then translated into minimum incident beam intensity needed to record particulate of various diameters. As well as testing holographic sensitivity and linearity of the emulsion exposure process, this technique also afforded a test on the value of a second reference beam as an intensity calibration device.

The design of the three-beam wide angle scattered light holocamera was accomplished early in the program, and was followed shortly by the fabrication of the three-plate film holder. Actual testing with the holocamera was not accomplished until later in the program, however, when the holocamera layout was breadboarded.

The parameter studies done with this holocamera included a particulate sizing. Two size ranges were studied. The first was a monodisperse water droplet distribution of size ranges 30 and 50 microns. The droplet size was calculated directly from the aerosol generator characteristics, and was also measured indirectly from the coherent light fringe pattern it produced. (See Section 3.2.) The two sizes thus obtained agreed to within 10 percent. The second size range was from submicron cigarette tobacco smoke. The size distribution of this smoke was not monodisperse. It was estimated directly from the forward scattered light intensity distribution as obtained both from holographic and direct observation. The measurements showed the smoke to be in the 0.2-micron size range, agreeing with commercially published data on such distribution.[11]

The two particulate distributions which were measured also represented two particle number densities. The water droplet density distribution was neither stochastic or homogeneous, since the droplets were generated in a straight stream, and no mixing mechanism was employed to disperse them. However, the droplet spacing resulted in an effective number density for a small enough volume, and this could be calculated directly from the aerosol generator characteristics. The smoke density, on the other hand, was measured directly from relative scattered light intensity measurements.

Particle velocity measurements were obtained on these two distributions. The velocities of the liquid aerosol droplets could be obtained by measuring the feed pressure applied to the aerosol solution flask, and using the known flow properties of the orifice as discussed in Section 3.2. The velocity of the air stream which carried the smoke particulate was measured with a hot wire anemometer.

Measurements of light intensity distribution were attempted at various angles and by various means, both from the holographic images and directly from the scattering volume. A method was devised by which light intensity from a small volume of a reconstructed real image of a homogram could be imaged onto a sensitive detector. This would allow some spatial resolution of particle size distribution as recorded by the hologram. Figure 3-16 illustrates the optical arrangement schematically. The hologram is assumed to present an effective aperture of diameter B.

Incident light on the hologram forms a real image of scattered light from a particulate cloud. A small volume element in this image is located at aperture 1. The first lens, having focal length y_1, images the first aperture onto the second aperture, whose purpose it is to shield the detector lens from seeing stray light from other portions of the scene volume. The second lens then focuses the light from the test volume onto the detector.

The first aperture effectively defines the test scene volume, δV_s (shown in Section 2.1) and shields the detector field of view from all but this small volume element. The outlines of the volume element are fuzzy, and are determined basically by the aperture diameter D_1, and the lens

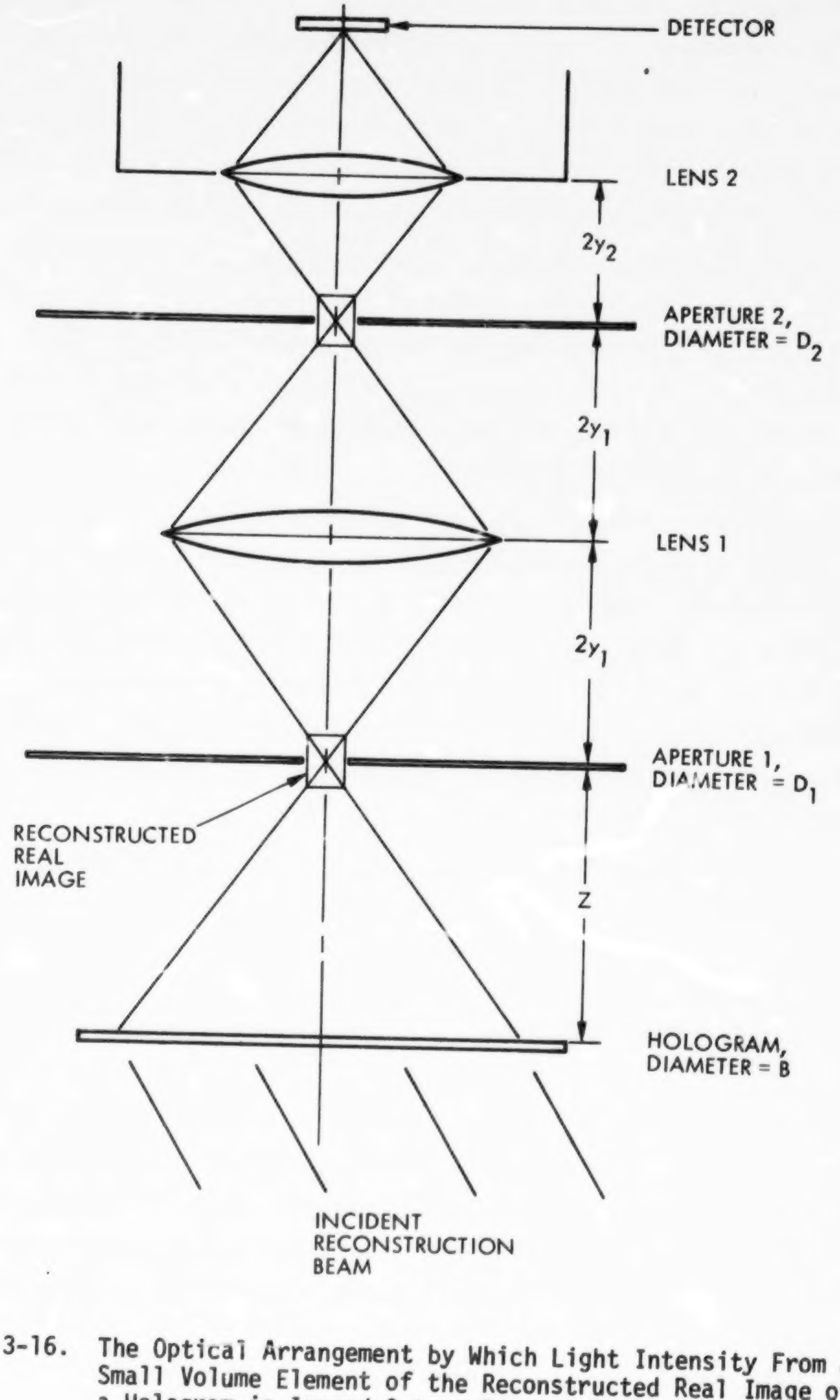
DETECTOR
LENS 2
$2y_2$
APERTURE 2, DIAMETER = D_2
$2y_1$
LENS 1
$2y_1$
APERTURE 1, DIAMETER = D_1
RECONSTRUCTED REAL IMAGE
Z
HOLOGRAM, DIAMETER = B
INCIDENT RECONSTRUCTION BEAM

Figure 3-16. The Optical Arrangement by Which Light Intensity From a Small Volume Element of the Reconstructed Real Image of a Hologram is Imaged Onto a Power Sensitive Detector

depth of focus. If the latter is taken as the depth at which point sources become defocused to the same diameter as the aperture, then the depth of field can be seen from geometrical considerations in Figure 3-16 to be $2Z\,(D_1/B)$, where Z is the distance from the plane of the hologram to the plane of the first aperture. We then have the following expression for the scene volume.

$$\delta V_s = \frac{\pi}{2}\,\frac{Z}{B}\,D_1^{\,3} \qquad (3\text{-}4)$$

The solid angle intercepted from the scene volume by the first lens may also be easily computed by integration.

$$\delta\Omega = 2\pi\left[1 - 1/\sqrt{1 + (D_1/Z)^2}\,\right] \qquad (3\text{-}5)$$

This apparatus was set up and tested on a hologram made of a cigarette smoke cloud (Hologram 13A, Section 3.4). Both apertures were 0.635 mm, and the objectives lens (lens 1) was a 48-mm-diameter, 57-mm focal length plano-convex lens. A United Detector Technology power meter was used as a detector. The sensing element was a silicon pin diode, with a one-square centimeter area. The detector meter was a digital readout with a maximum sensitivity of 10^{-10} watts. The reconstructed scene volume was located in the first aperture with little difficulty. The process was facilitated by the presence of a small thread located in the scene volume to provide an auxiliary intensity reference.

The detector was sensitive enough to read the light transmitted from the scene volume. However, the problem of optical alignment proved to be difficult beyond our available resources. No data were obtained by this method.

The most useful data on light scattering intensity as a function of angle were determined by visual estimation. These data are discussed in Section 3.4. Relative intensity estimates were obtained by eye, both from holographic reconstruction and directly from a real scene. Since the human perceptive faculty is nonlinear, we made an attempt to calibrate it against power meter readings of helium-neon laser light incident on ground glass and transmitted through a 0.635-mm aperture. A series of neutral density filters was used to reduce the perceived intensity. The results, nonetheless, must be regarded as low accuracy numbers, on the order of 30 to 50 percent. Calibration to absolute intensity was made using the power meter.

A series of sixteen holographic recordings were made with the three-beam wide angle scattered light apparatus. These holograms were numbered consecutively. They were all made on standard AGFA8E75 102- by 127-mm (4- by 5-inch) plates. The first five holograms were single plate holograms of side scattered light only ($\theta = 90$ degrees). Of these, the first four had just a single reference beam corresponding to light coming from the second scatterball. During these recordings the scatterballs were in the primary configuration, shown in Figures 3-5 and 3-6, and were both on the same side of the plate holder.

Holographic records 6 through 11 were made with three plates each. The plates were labeled A, B and C corresponding to forward, side, and back scattered light respectively. The holographic records up through number 8 were all made with a low density of aerosol droplets, so that only two or three droplets appeared in the scene volume each time. With hologram number 9 the droplet density was increased, and the smoke generator was added so that a stream of 50-micron droplets appeared mixed with a cloud of smoke particles.

Holograms 9 through 11 were made in this fashion, and were the best of this series of holograms. Hologram number 11 was made with the droplet generator frequency higher by a factor of three, but all other conditions the same. Thus, the droplet diameter was 30 microns instead of 50.

For holograms 12 through 16 the scatterballs were relocated near the alternate configuration, and a small thread was placed in the scene to provide an auxiliary intensity reference source. These holograms consisted of three recordings each, of tobacco smoke clouds only. To understand the reasons behind these changes, we will review the development procedures for the holocamera.

The first eleven holographic records were made with 12.7-mm stainless steel spheres for scatterballs. These spheres were placed in the primary configuration. Several problems became evident as these holograms were taken. The scatterballs were polished with Wenol jewelers' rouge, but the surfaces could not be made optically smooth. Tiny nicks and scratches in the scatterballs affected the quality of the reference beams arriving at the film plates.

Secondly, the reference light was not distributed uniformly over the three plates. This made a linear reconstruction impossible to achieve unless the hologram were put back in position in the holocamera and reconstructed there. When this was attempted, the reconstructions were found to be of generally poor quality due to the difficulty of getting enough reconstruction beam intensity and of masking from stray light.

Thirdly, the holograms were fogging quite badly. This was determined to be caused by depolarization of the reference beams with respect to the scene beam and was a characteristic of the geometry. In all cases the incident scene beam was polarized vertically, or in the plane of the scattering. The reference beam was depolarized by about 45 degrees upon reflection from the surface of the scatterball.

Finally, with the scatterballs in their primary location, it was impossible to use the intensity reference scatterball as a valid calibration source. The reason for this was the nonuniformity of the reference light over the plane of the hologram. The furthest scatterball was used as a reconstruction reference, at an angle of about 25 degrees from the hologram. The nearer scatterball was tried as an intensity reference.

After the 11th holographic record was taken, the holocamera was modified. The polished stainless steel scatterballs were replaced with two glass lenses, 10 mm in diameter and 10 mm focal length, and plated first with silver and then with gold. Both platings proved unable to stand up under the power density from the ruby laser. When a gold coating was vacuum-sputtered on to a thickness of 100 angstroms, it was reliable.

The scatterballs were then moved to their new location, near the alternate configuration but closer to the scattering plane, in order to minimize depolarization of the reference beams. The 10-mm radius of curvature was not small enough to spread the reference beams sufficiently to cover all three film plates at once. A good compromise was achieved by illuminating the forward 90 degrees with one scatterball and the backward 90 degrees with the other scatterball. This meant that neither scatterball was available as an intensity calibration reference. To provide for this, a thin fabric thread was stretched through the lower portion of the scene volume. The scattered light intensity from the thread was measured with the UDT power meter. It was found to be isotropic.

The last five holographic recordings were made with this modifications, studying light scattered from cigarette smoke. The holograms were of generally good quality, and the previously experienced fogging was absent. The smoke volume could be separately distinguished from the reference thread. However, reconstruction of the holograms in situ, in the holocamera, gave rise to the same problems as before. Our resources did not permit the solution of the problem of obtaining exact reconstructions. The reconstructions shown in Section 3.4 were made with a Spectra-Physics 124 He-Ne laser with a spatial filter and beam expander. The reconstruction beam thus obtained is that of a point source at a distance of two or three times that of the scatterballs from the plate.

3.4 RESULTS

There were three basic phases of this program which deserve to be discussed in terms of the results they yielded. These include accomplishments with the Garrett holocamera, the holographic linearity and sensitivity tests, and the three-beam wide angle scattered light holocamera. We will summarize and discuss each in turn.

Garrett Holocamera

With the Garrett holocamera, detection of particulate sizes down to 1 micron by forward scattered light was demonstrated. It was visually apparent that some differentiation between particulate size ranges and size distributions was possible, at least in an unmixed state, by studying variations in angular scattered light intensity. Although nothing basically new was learned, the method did demonstrate a consistently higher sensitivity by virtue of a lower noise-to-signal ratio than has been previously obtained with similar systems.

The Garrett holocamera may be regarded as an optimum, two-beam scattered light holocamera design for the sensitive forward scattering regime. The scattering angles which could be visualized were between zero and fifteen degrees.

The holocamera was tested by recording holograms of particulate thrust, blown, or converted into the scene volume (i.e., between the focusing lens set and the beam stop). Scrutiny of Figure 3-2 shows the nebulizer used to thrust the larger 40 to 50 microns (in diameter) particles into the scene volume. It is the plastic bottle just before the model of the portion of the fan. The nebulizer was a plastic squeeze wash bottle filled with test powder. A rubber tube was attached to the spout. Blowing into the tube caused a cloud of particulate to fill the scene volume. The nebulizer was filled with either phenolic particles or glass micro-balloons. Both samples consisted of particles primarily in the 30 to 50-micron size range. Photomicrographs of these two types of particles are shown in Figures 3-17 and 3-18. The glass micro-balloons appear white like sugar. The phenolic particles appear brown like freeze-dried coffee.

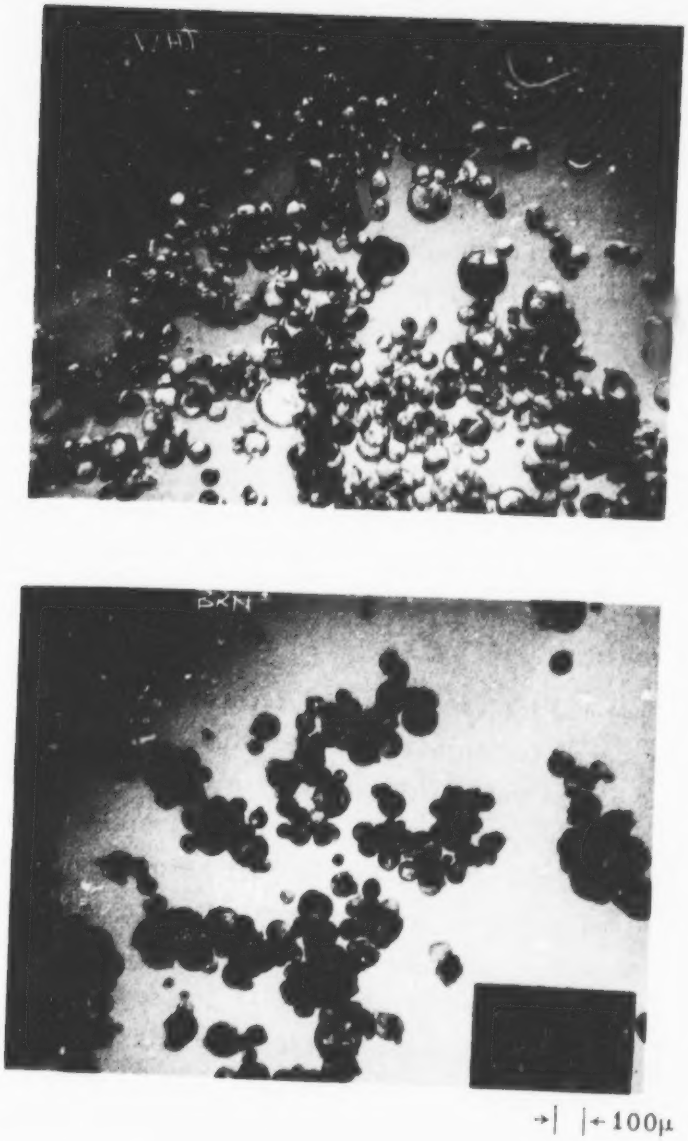

Figure 3-17. Photomicrographs of Sample "Micro-Balloons." The upper picture shows glass particles, which appear to the eye as white powder. The lower picture shows phenolic particles, which look brown. Included in one is a scale, with 100-micron spacing between major divisions.

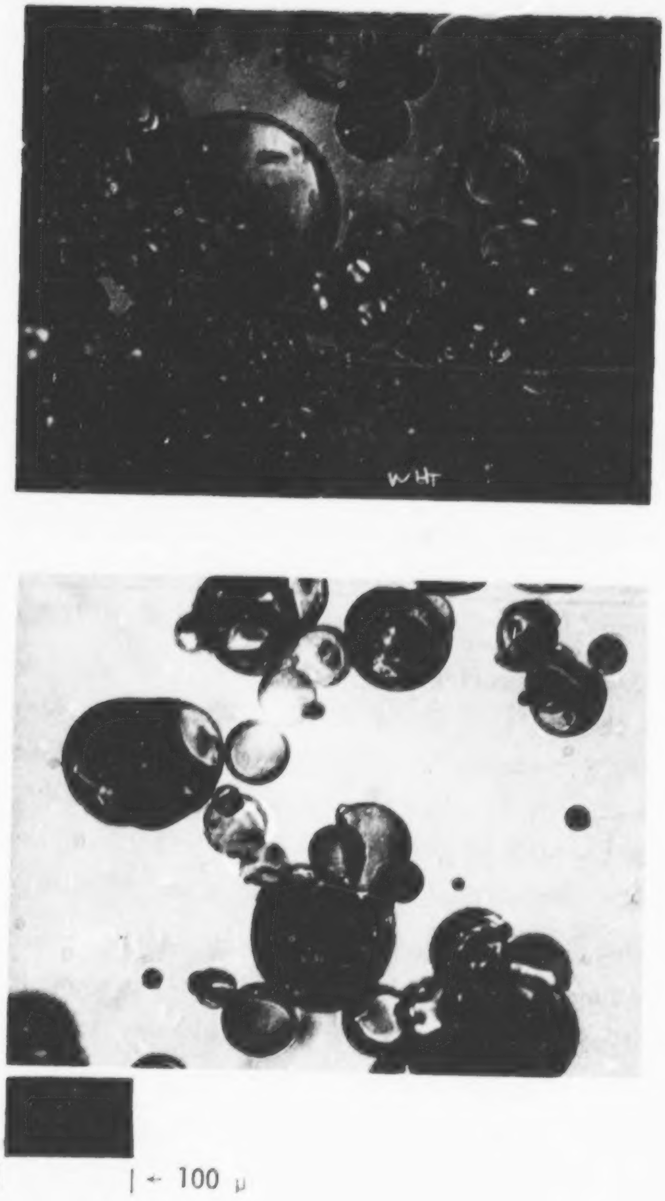

Figure 3-18. High Magnification Photomicrographs of Sample "Micro-balloons." The upper picture shows glass particulate. The lower picture shows phenolic particles. A scale of 10-micron spacing has been included.

To test the sensitivity of the scheme for particles of even smaller size, incense was employed as the scattering source.* This material had been used in earlier tests of scattered light holography conducted at TRW for EPA.[2] This type of incense produces particles in the size range of 1 to 3 microns diameter. The incense burner merely replaced the nebulizer in the scene volume.

Holograms were made of the three different scattering targets. Exposure was with light from a Kerr cell Q-switched ruby laser. All three size ranges could be easily recorded, even of the most tenuous clouds. Examples in terms of photographs of selected reconstructed holograms are shown in Figures 3-19, 3-20, and 3-21. The first shows examples of the recording of holograms of incense. The two are pictures of different holograms. The cloud like character of these particles is clearly evident. Both pictures suffer from a depth-of-focus problem of the copy camera. Figure 3-20 is a pair of photos taken from the same hologram of the glass "micro-balloons." The two pictures differ only by exposure. The picture is clearly more granular, particles are seen as individual bright points of light. The edge of the plastic nebulizer is seen in the right-hand picture.

Figure 3-21 is similar except that it is of the phenolic particles, which are on the whole slightly larger than the glass micro-balloons. These particles have a tendency to stick together, making large agglomerates several hundred microns in diameter. Like the hologram of the glass micro-balloons, the picture is more granular or less cloudlike than the incense smoke which was composed of particles an order of magnitude smaller.

Visual inspection of the holograms showed the expected variation in intensity as a function of scattering angle. This variation and the general appearance of each type of scattering enable one to recognize one size range from the other.

In summary, forward scattered light holograms have been recorded or particles in the size range of 1 to 3 microns. The tests re-established our ability to holographically record particles of this small size. Comparisons of these holograms with ones of larger particles (typically, 30 microns) showed both qualitative and quantitative differences.

---

*Trappist Incense, produced by Abbey of Our Lady of New Melleray, Dubuque, Iowa.

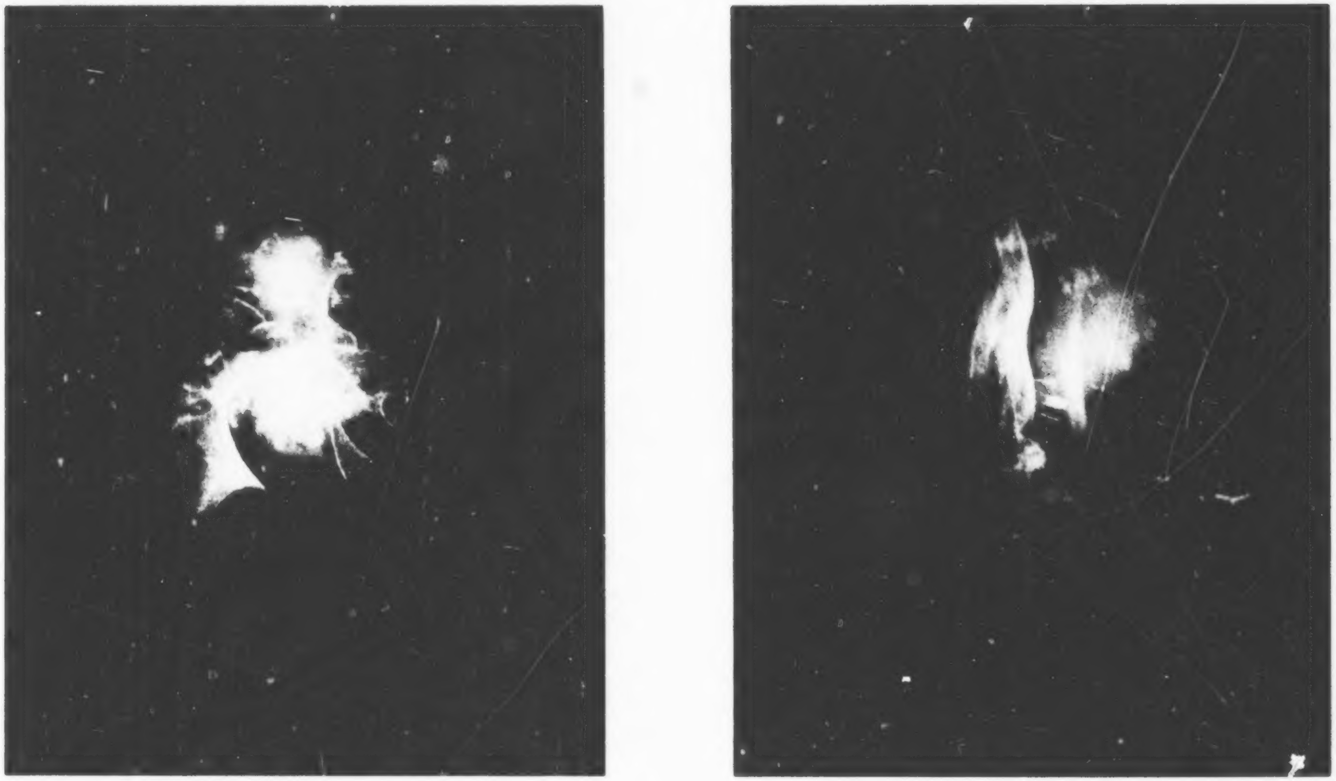

Figure 3-19. Photographs of the Reconstruction of Two Different Holograms of Incense Smoke Recorded in the "Dark Field" Scattered Light Holographic Arrangement Shown in Figure 3-1. Incense provided a test source of particles of primarily 1 to 3 micron size.

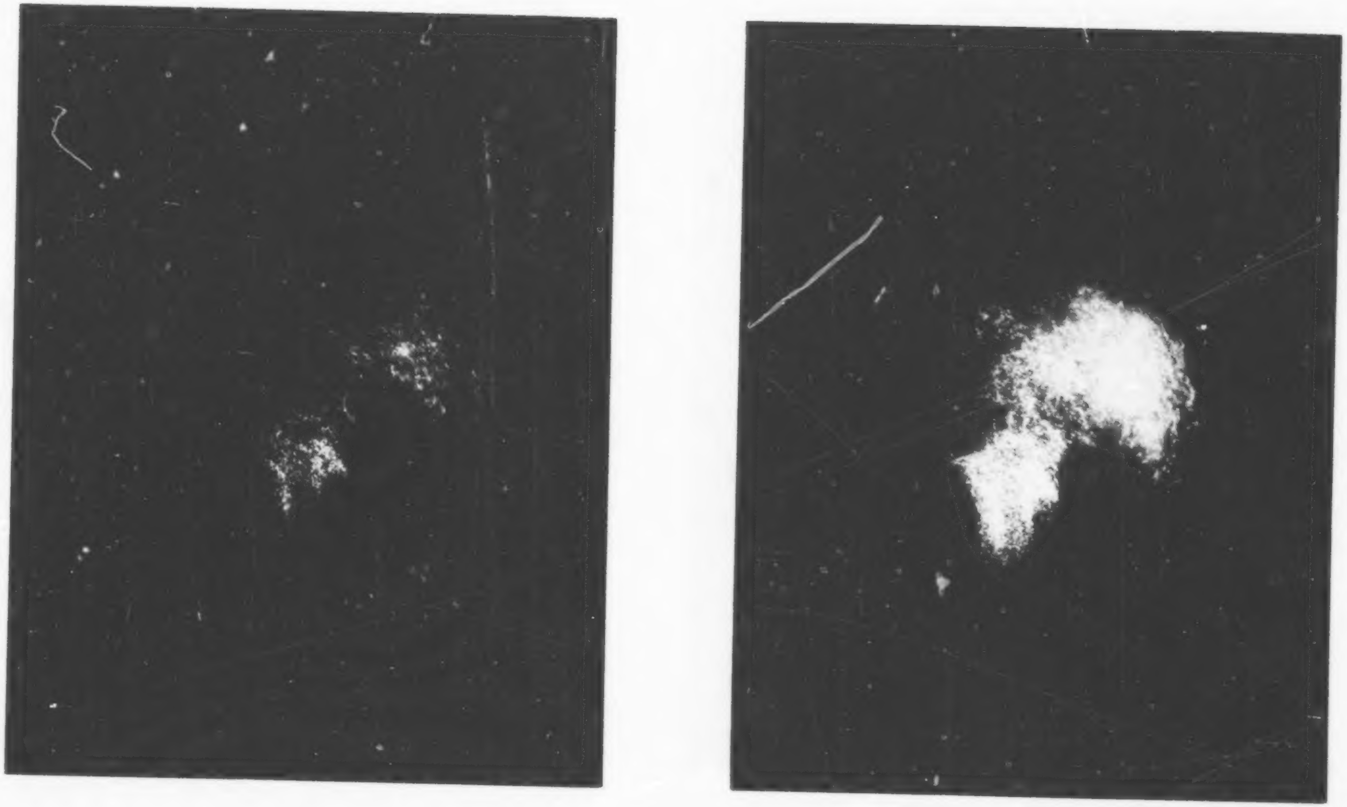

Figure 3-20. Photographs of the Reconstruction of Same Scattered Light Hologram of Glass Micro-Balloons of 30-Micron Typical Size. The hologram was recorded in the holographic apparatus shown in Figure 3-1.

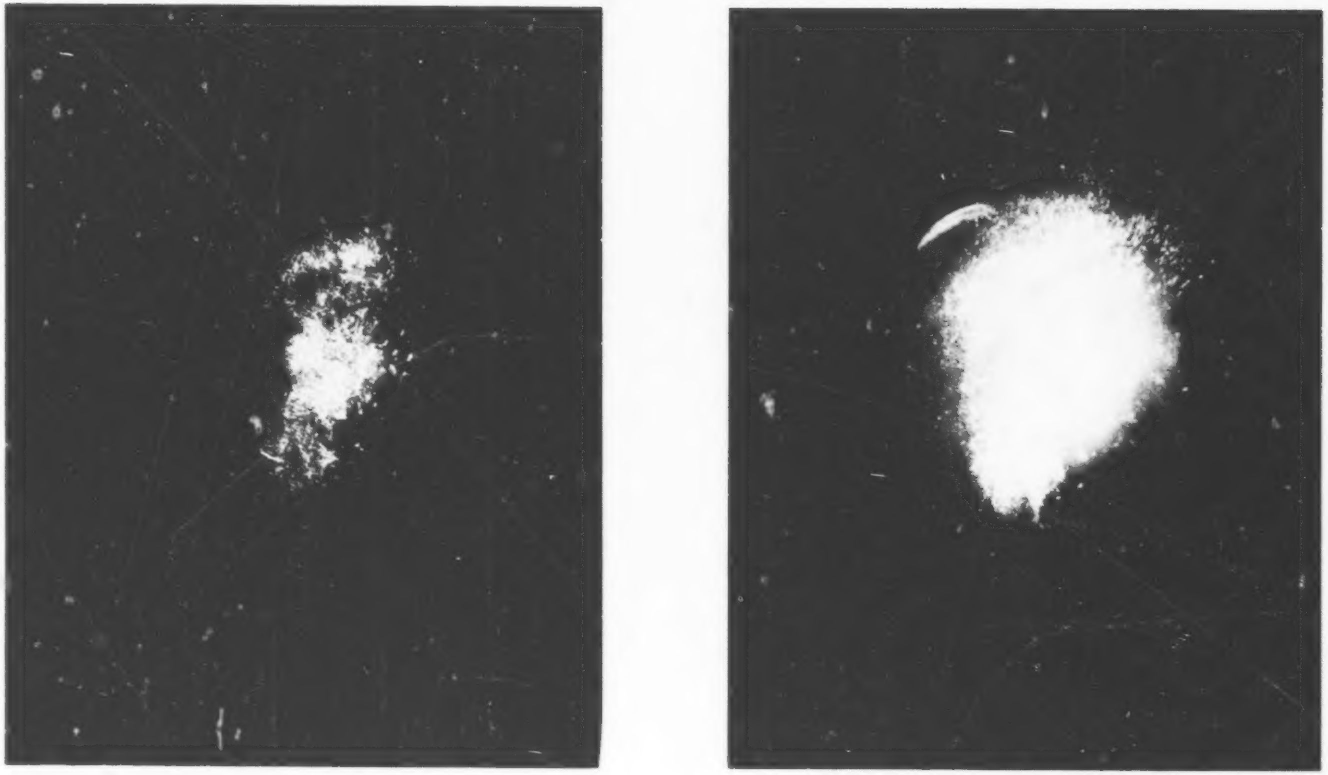

Figure 3-21. Photographs of the Reconstruction of the Same Hologram of Phenolic Micro-Balloons Recorded in the Dark Field Scattered Light Holocamera Shown in Figure 3-1. The micro-balloons were of 30- to 50-micron size, typically. The lip of the nebulizer is seen in the overexposed picture.

All the scattered light holograms shown in this report were recorded with a more conventional Q-switched ruby laser illuminator, namely, a laser without any coherence-improving elements (such as a chlorophyll dye cell) within the laser cavity.[*] As a result, many of the holograms showed the effects of the limited coherence of the Kerr cell Q-switch ruby oscillator. For these reasons, analysis was not attempted. Holograms suitable for analysis should be recorded with a more coherent oscillator.

Holographic Linearity and Sensitivity Tests

The sensitivity of the holographic process was explored directly in terms of the ratio of scene light intensity to reference light intensity. This was found to be a significant parameter. A limiting value for this ration of about 3×10^{-7} has been found. Surprisingly, the three-beam configuration was not found to contribute significantly to the sensitivity.

During the first set of experiments, the two reference beams were made to be equal in intensity at the hologram. (See Section 3.2.) The scene beam was attenuated so as to be 0.3×10^{-6} as intense.[**]

Holograms were recorded on Agfa 8E75 plate; a 1-minute exposure time developed plates in 2 minutes.

After exposure and development, the dried plate (now a hologram) was placed back in the three-beam apparatus. The kinematic plate holder repositioned the plate accurately. The second reference beam was blocked. By viewing through the plate, the reconstructed image of the scene could be observed. The reconstructed image of the 0.3×10^{-6} scene point source of light could be observed with the unaided eye. Unblocking the scene beam helped to locate the scene beam in space. This experiment verified earlier tests done in the laboratory on a less sophisticated optical arrangement; namely, the ability of a hologram with two reference beams to sense a very weak signal, one of an intensity of 0.3×10^{-6} of that of the reference beam.

---

[*] In the AiResearch project, precise timing is a requirement. As a result the chlorophyll coherence stretcher was removed.

[**] The attenuators were lenses from a pair of welding goggles. The transmission of each was measured at the onset with a silicon photocell and a microvoltmeter (Hewlett Packard Model 124).

The question as to the merits of the second reference beam was next quickly examined. A hologram was recorded with the second reference beam blocked. That is to say, in this test, the hologram only saw a single reference beam and the same greatly attenuated scene beam (0.3×10^{-6} as intense as the reference beam). A hologram was exposed. After development, it was also replaced in the kinematic plate holder and reconstructed. Observation of the plate with the unaided eye showed the point source reconstructed! This was actually a surprise and indicates that the merits of a second reference beam, at least as a means for increasing hologram sensitivity, has not been established.

A modified set of experiments was then conducted with the apparatus; namely, a 30-degree angle between the two reference beams, a 45-degree angle between the axis of the inner reference beam and the axis of the scene beam, and a 50-degree angle between the plane of the plate and the axis of the scene beam. The apparatus was improved to the extent that both single and double reference beam type holograms could be recorded on the same plate. This minimized the effects of differences in redevelopment. This was achieved by blocking the upper half of the second reference beam with a strip of black paper. An attenuator was added to the lower portion of the first reference beam. The beams were adjusted to make the two reference beams equal. That is to say, the lower portion of the photographic plate recorded a double reference beam hologram with reference beams of equal intensity. The upper portion of the plate recorded a hologram with only a single reference beam. The upper beam was 1.5 times more intense than either of the lower reference beams. Intensities of the reference beams, as measured normal to the beam directions with a silicon photocell, are shown in Table 3-1. Also included in this table is the measured unattenuated intensity of the scene beam.

Table 3-1. Reference and Scene Beam Intensities in Terms of Photocell Output

Position of Plate	Reference Beam No. 1 Millivolts	Reference Beam No. 2 Millivolts	Maximum Scene Beam Intensity, Millivolts
Single Reference Portion	0.23	0	0.05
Double Reference Portion	0.15	0.14	0.05

Adding intensities, one sees initial scene-to-reference beam ratios of 0.22 and 0.17, respectively.

The scene beam intensity was controlled with attenuators placed behind the 40X microscope objective. Attenuators were either pieces from a welder's goggle, or Wratten No. 96 (N.D. 1.0) gelatin filters. The attenuation of these filters as measured independently with a helium-neon laser is presented in Table 3-2.

As described in the previous report, holograms were recorded with different degrees of attenuation of the scene beam. The beam was attenuated until it could no longer be seen in the reconstruction with a telescope of 2 centimeters aperture. The results of several experiments are summarized in Table 3-3. These tests led us to the conclusion that 3.0×10^{-7} was a practical lower limit to the scene-reference beam ratio.

After development, the hologram was put back into the apparatus and reconstructed with the light from the first reference beam. The second reference beam was blocked. By looking through the developed plate, the location of the scene point source was seen through the developed plate. The scene beam was blocked and the field searched for the reconstruction. Equally practical was the tilting of the plate and the observation of two point sources, namely, the original scene through the plate and the reconstruction.

The experiments afforded several interesting side observations. First, the single beam portion of the hologram reconstructed with more background noise than the portion of the hologram with the two-reference beams. This did not, however, limit our ability to recognize the reconstructed point source. For this reason, the two methods must be judged equal in sensitivity. The intensity of the reconstructed point in the two-reference beam portion appeared weaker than in the single-beam portion. Second, reconstruction of the test holograms with a more intense (80 milliwatt) helium-neon reconstruction laser did not increase our ability to detect reconstructed

Table 3-2. Transmission of Filters at 0.6328 Micron

Type	
Welder's Goggles	1.32×10^{-3}
Wratten N.D. 1.0	1.03×10^{-1}

Table 3-3. Experimental Results

Case	Hologram Portion	Initial Scene-Reference Ratio	Scene Attenuation	Net Scene/Reference Ratio	Scene Reconstruction
I	A. Single Reference Portion of Hologram	0.22	1.75×10^{-6} (2 welding goggles)	3.9×10^{-7}	Visible to naked eye
	B. Double Reference Portion	0.17	1.75×10^{-6} (2 welding goggles)	3.0×10^{-7}	Visible to naked eye
II	A. Single Reference Portion of Hologram	0.22	1.8×10^{-7} (2 welding goggles and Wratten ND 1)	4.0×10^{-8}	Visible through telescope
	B. Double Reference Portion	0.17	1.8×10^{-7} (2 welding goggles and Wratten ND 1)	3.0×10^{-8}	Invisible through telescope

points even with lower scene-reference beam ratios (Case II in Table 3-3). Third, at the level of 3.0×10^{-7}, location of the reconstructed point source without prior knowledge of its position was almost impossible. For these reasons, we now accept 3×10^{-7} as a practical lower limit to the scene-reference beam ratio of a two-beam holographic arrangement.

Given 2 or 3×10^{-7} as the minimum scene-to-reference beam intensity required to reconstruct a hologram of a point source, one can derive an equation for the amount of laser beam energy needed to record holograms of individual small micron-sized particles. For reasons of time and simplicity, we assume that the particle scatters uniformly. On this basis, the light energy density or flux scattered by a particle of scattering cross section Σ_{sca}, at a distance r from the hologram, is

$$I_{sca} = I_o \frac{\Sigma_{sca}}{4\pi r^2} \tag{3-6}$$

Knowing now that the reference beam can be $1/3 \times 10^{-7}$ the intensity of the scene beam, a quantity called K (i.e., K = min scene/reference ratio), the above equation can be written in terms of minimum reference beam intensity;

$$I_{\substack{min\\ref}} = I_o \frac{\Sigma_{sca}}{4\pi r^2 K} \tag{3-7}$$

where $K = 3 \times 10^{-7}$. The reference flux is then equated to the sensitivity of the plate, a quantity represented by ϵ_s (for Agfa 8E75 holographic plate, $\epsilon_s = 10$ microjoules/cm^2). Sensiometric curves for more popular emulsions are given in Figure 3-22. Substitution and solving for the laser energy delivered over a pulse time τ yields

$$I_o \tau = \frac{4\pi r^2}{\Sigma_{sca}} \epsilon_s K \tag{3-8}$$

assuming the scattering cross section can be expressed in terms of an effective scattering diameter d_s, so that

$$\Sigma_{sca} = \frac{\pi}{4} d_s^2$$

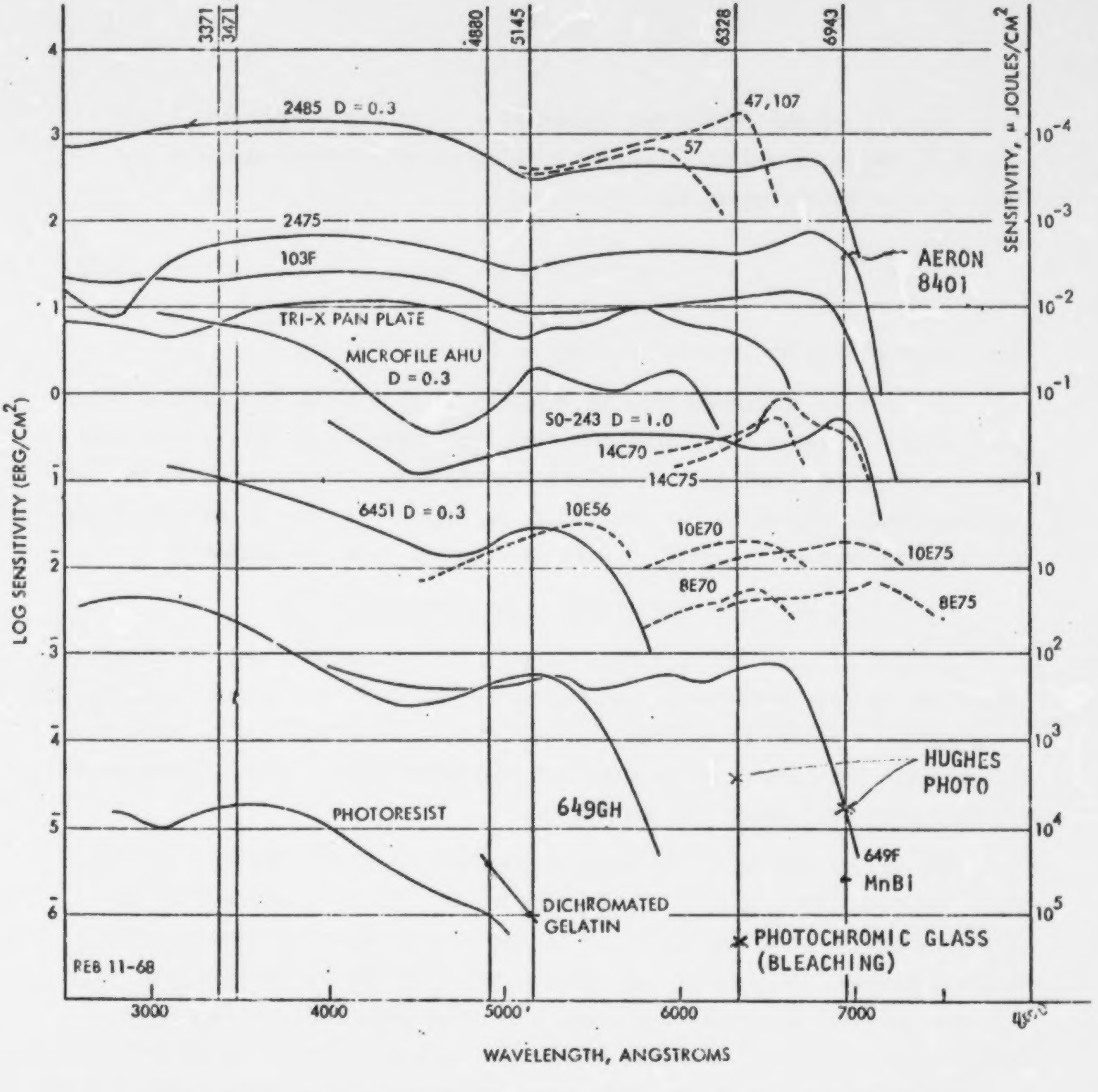

Figure 3-22. Sensiometric Curves of Emulsions Used in Holography

the above equation yields

$$I_o = 16 \left(\frac{r}{d_s}\right) \epsilon_s K \qquad (3\text{-}9)$$

Thus, for a 1-micron scattering diameter, ϵ_s = 10 microjoules/cm^2 and K = 3 x 10^{-7}, the flux needed to record a hologram of a single particle a distance r from the hologram plate is

$$I_o\tau = 4.8 \times 110^{-3} r^2 \text{ joules/cm}^2 \qquad (3\text{-}10)$$

This equation can be graphed as shown in Figure 3-23.

If light is scattered from an ensemble of particles, the foregoing analysis should be valid under the condition that there is no multiple scattering and that the total scattering cross section used corresponds to the sum of the cross sections of the individual particles. A similar minimum scene-to-reference ratio ($K = 3 \times 10^{-7}$) will be required from the ensemble.

Three-Beam Wide Angle Scattered Light Holocamera

The use of a second reference beam in the scattered light holocamera was found to have merit only inasmuch as it could be used as an intensity reference. A number of configurational changes were explored in order to try and use the holocamera to its best advantage in this mode. These were discussed at some length in Section 3.3.

The main problems in hologram reconstruction and interpretation arose from the nonuniformity of the reference beams. It may therefore be concluded that the best configuration to facilitate reconstruction and maintain linearity, although it was never actually tried during this program, was one in which the reference beams come from point sources located at great enough distances from the holographic plate to provide a uniform intensity incident wave front. The point sources could be two spatial filters with beam expanding optics, such as were used in the three-beam holographic sensitivity tests discussed in Section 3.2 and illustrated in Figure 3-4. An alternative is to expand the beam with a single spatial filter arrangement, and then direct the expanded beam through a beam splitter as illustrated in Figure 3-24. This arrangement has also been used successfully in laboratory experiments.

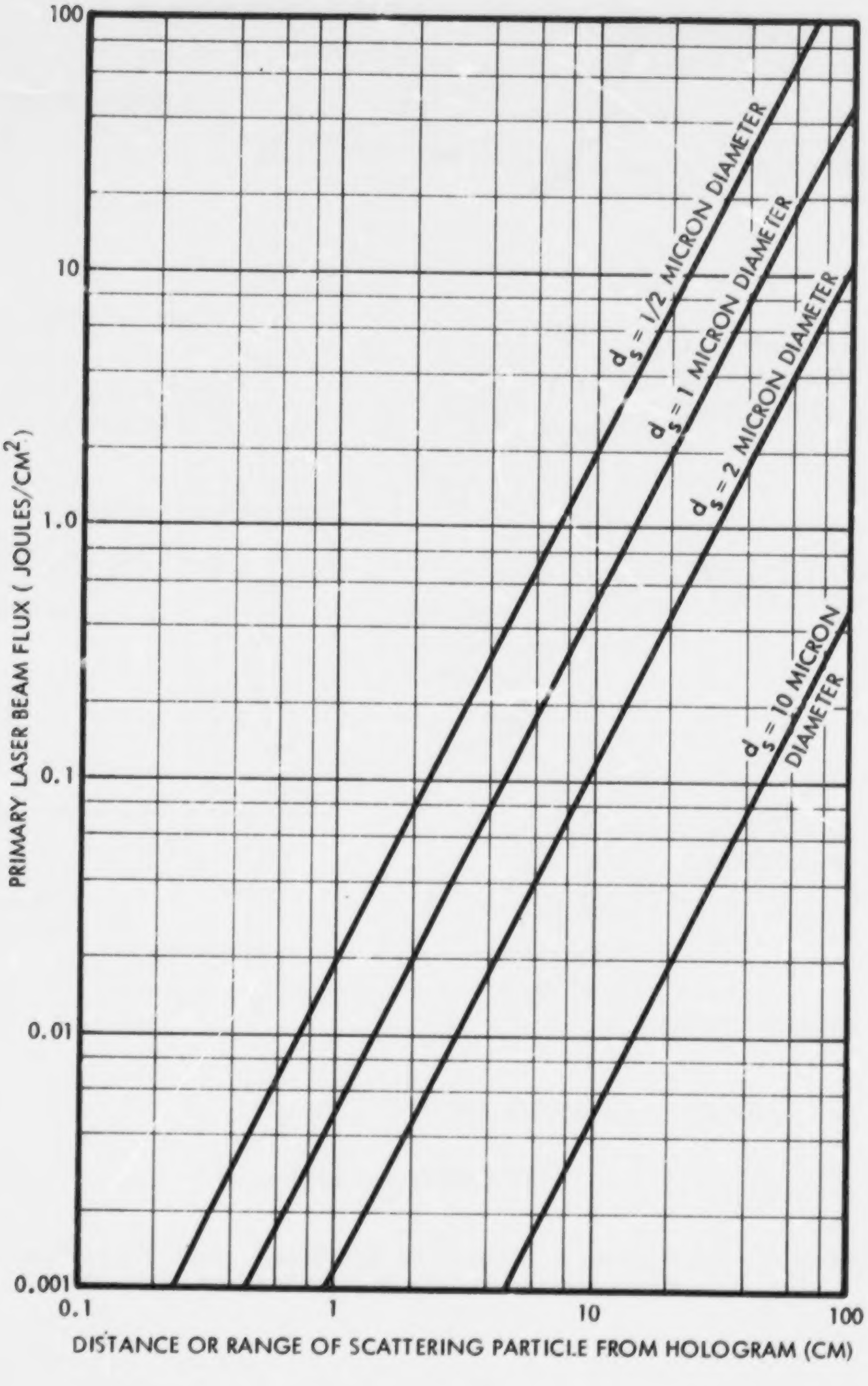

Figure 3-23. Primary Laser Beam Flux to Record Scattered Light Holograms of Individual Particles on Agfa 8E75 Plate

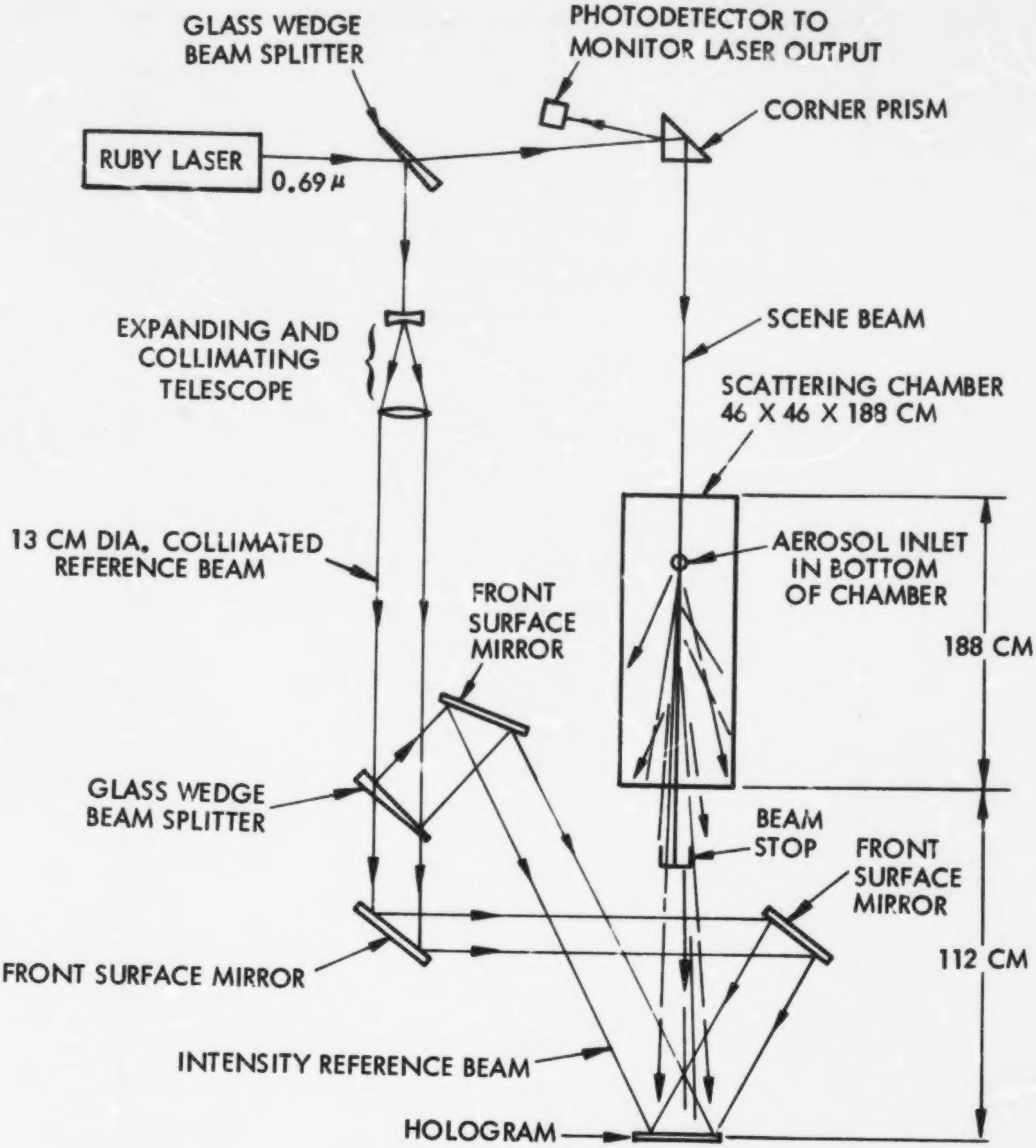
GLASS WEDGE
BEAM SPLITTER
PHOTODETECTOR TO
MONITOR LASER OUTPUT
CORNER PRISM
RUBY LASER
0.69 μ
EXPANDING AND
COLLIMATING
TELESCOPE
SCENE BEAM
SCATTERING CHAMBER
46 X 46 X 188 CM
13 CM DIA. COLLIMATED
REFERENCE BEAM
AEROSOL INLET
IN BOTTOM
OF CHAMBER
FRONT
SURFACE
MIRROR
188 CM
GLASS WEDGE
BEAM SPLITTER
BEAM
STOP
FRONT
SURFACE
MIRROR
FRONT SURFACE MIRROR
112 CM
INTENSITY REFERENCE BEAM
HOLOGRAM

Figure 3-24. Schematic Diagram of Scattered Light Three-Beam Transmission Holocamera Test Setup

It is more difficult to direct two reference beams thus obtained onto a set of three holographic plates arranged to record light scattered over a full 180-degree range. However the results of this program also indicate that no great benefits are derived from doing so. It appears to be much easier to obtain good information about particulate size distributions from light scattered through a relatively narrow range of angles, such as forward scattering, than to attempt to coorelate scattering over the whole range. (See Section 2.5 for a discussion of the analysis of this problem.) Usually all the scattering information needed can be recorded on one plate.

Three-beam scattered light holograms were made of 30- and 50-micron water droplets obtained from the monodisperse droplet generator. Holograms were also obtained of a sub-micron tobacco smoke, and of mixtures of these two particulate. The two types of particulate were easily differentiable visually, and apparently also from scattered light angular variation considerations. The incident beam light was polarized in the scattering plane. Under these conditions, the side scattered light intensity is very low. The holocamera configuration was not sensitive enough to extract much information from side scattered light from sub-micron particulate. The forward scattered light, however, was found to be amenable to a size distribution analysis, and was of sufficiently high intensity to seem preferable for analysis from sensitivity considerations.

Figure 3-25 shows reconstruction photographs of three views of a mixture of tobacco smoke and 50-micron water droplets. They were photographed from hologram set number 9, the A, B and C holograms corresponding to forward, side and back scattering, respectively. The reconstruction photos were taken of the real image projected by the hologram. A copy camera with a 210-mm Schneider Kreuznach lens was used. Figure 3-25a shows the strong forward scattering at 30 degrees from the droplet stream. The smoke is also visible behind the droplets. Figures 3-25b and c are both views of hologram 9B, taken at an angle of 90 degrees. In Figure 3-25b, the focal plane is on the droplets, and the smoke is basely visible behind them. In Figure 3-25c the camera was focused on the smoke.

These figures are of interest because of the similarity of the size ranges to a sub-micron industrial fume mixed with wet steam. In a well-developed fog or vapor the water droplets are in the 10- to 100-micron size

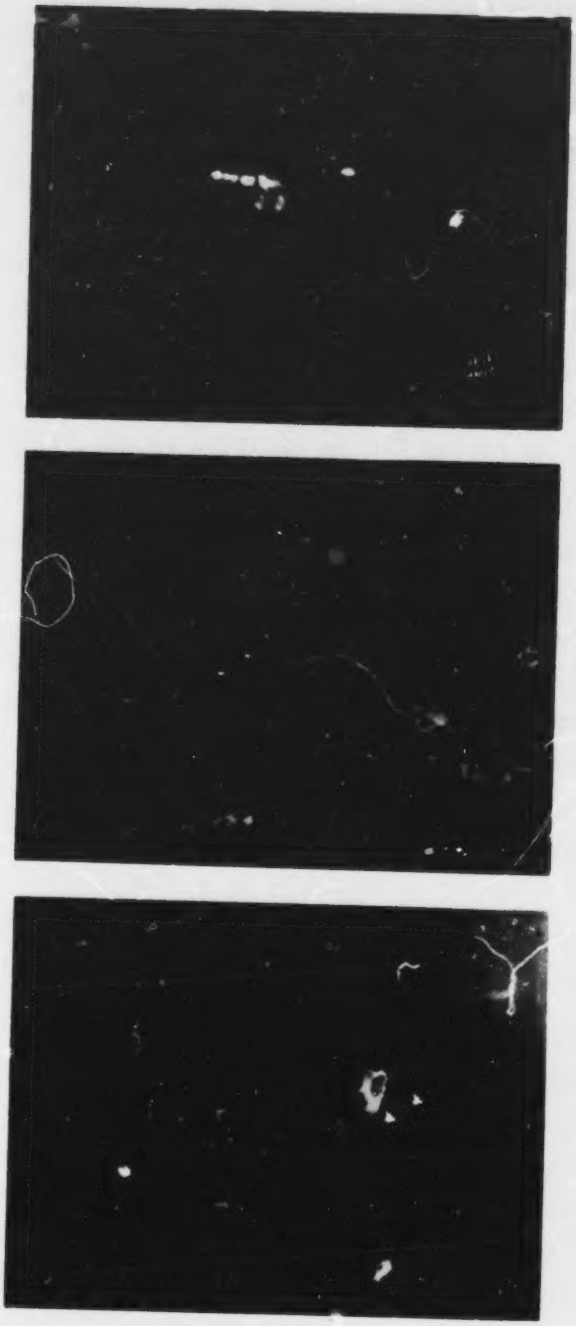

(A) VIEW OF HOLOGRAM 9A, SCATTERING ANGLE 30 DEGREES. FOCUS INTERMEDIATE TO DROPLETS AND SMOKE.

(B) VIEW OF HOLOGRAM 9B, SCATTERING ANGLE OF 90 DEGREES. FOCUS IS ON THE DROPLETS.

(C) VIEW OF HOLOGRAM 9B, SCATTERING ANGLE OF 90 DEGREES. FOCUS IS IN THE SMOKE CLOUD.

Figure 3-25. Reconstruction Photographs of Holograms 9A and 9B, Showing Forward and Side Scattering. The scene volume contains tobacco smoke, and 50-micron water droplets

range.[11] Thus, scattered light techniques should be capable of distinguishing between the fume content and water content of an industrial waste, for example. This possibility was also analyzed in Section 2.6.

Figure 3-26 shows a reconstruction of a hologram of scattered light from tobacco smoke, after the configuration of the holocamera was changed. The hologram number was 12a. Two different scattering angles were viewed, each corresponding to forward scattering. The first angle was 30 degrees, normal to the hologram plane. The second angle was about 20 degrees, scattering angle. This image contained a thin thread which was used as a scattered light intensity reference. In Figure 3-26a, the camera is focused on a fairly large volume of smoke below and behind the thread. In Figure 3-26b the scattered light is seen to be more intense.

Figure 3-27 shows an unusual effect of secondary light scattered off the thread being strongly forward scattered by the smoke. This effect was found in hologram set 16, and was seen in all three views. Figure 3-27a shows the view at a scattering angle of 30 degrees, and Figure 3-27b shows the backscattering angle of 150 degrees. In each case, however, the scattered light comes from the thread and the actual scattering angle is about 10 degrees.

Particle Size Distributions

Three separate types of particulates were sized during this program. The glass and phenolic micro-balloons used with the Garrett holocamera experiments were described earlier in this section. The size of these was visually estimated from photomicrographs to be in the 30 to 50 micron range. The aerosol droplets from the monodisperse aerosol generator were sized both by calculations using the generator characteristics, and by direct light interference measurements as described in Section 3.2. Droplets of diameters 50 and 30 microns were formed, and may be estimated to be monodisperse to within about 10 percent of volume.

The size distribution of the tobacco smoke was also estimated from scattered light data. These data were obtained by visual estimation as described in Section 3.3. It is a composite obtained partly by direct visual observation of the scene volume and partly by inspection of holograms 12, 13 and 14. The curve which was obtained is shown in Figure 3-28, which is

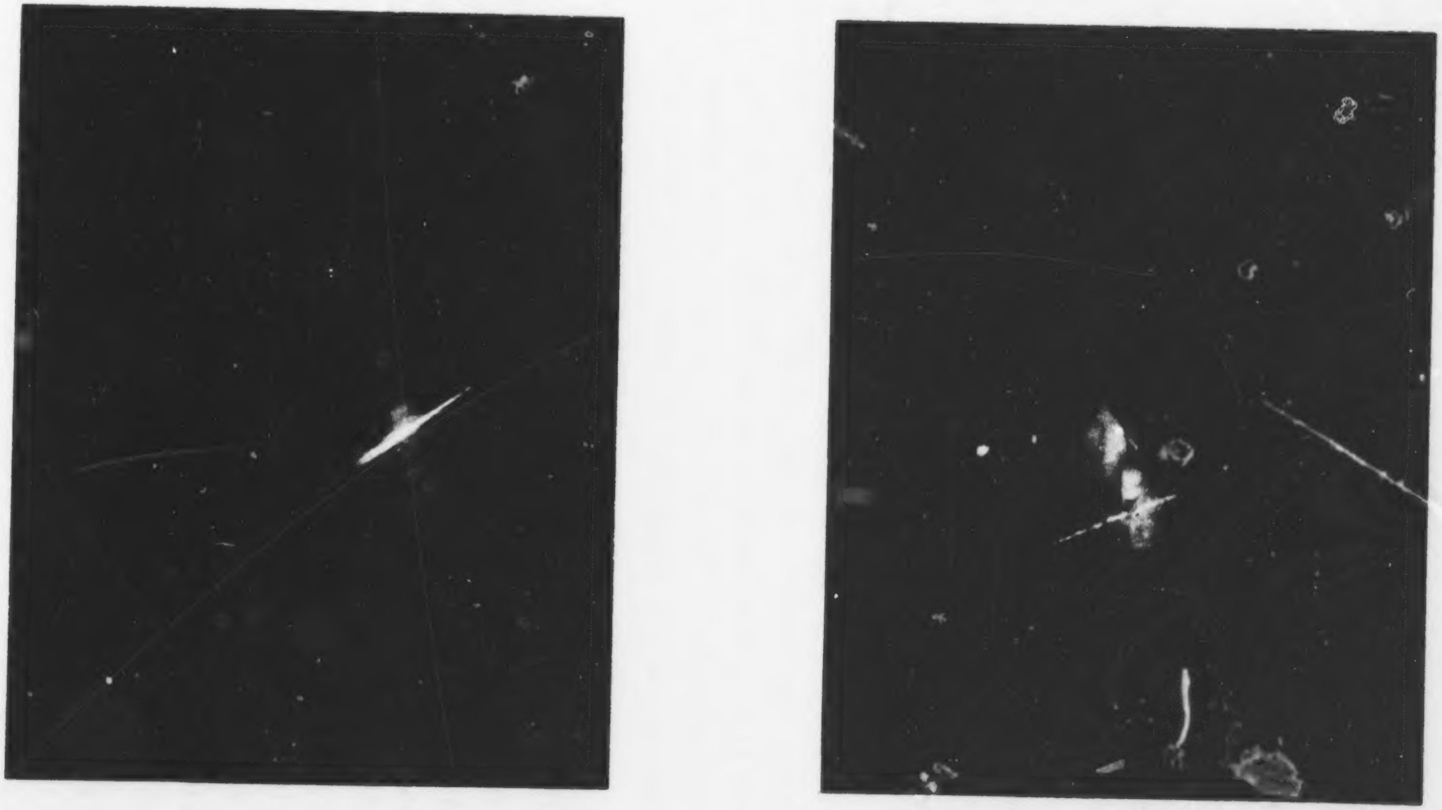

(A) FORWARD SCATTERING AT 30 DEGREES

(B) FORWARD SCATTERING AT 20 DEGREES

Figure 3-26. Reconstruction of Hologram 12A, Showing Forward Scattered Light From Tobacco Smoke. Two scattering angles are viewed. The thread was used as a scattered light intensity reference.

(A) HOLOGRAM 16A, SCATTERING ANGLE OF 30 DEGREES

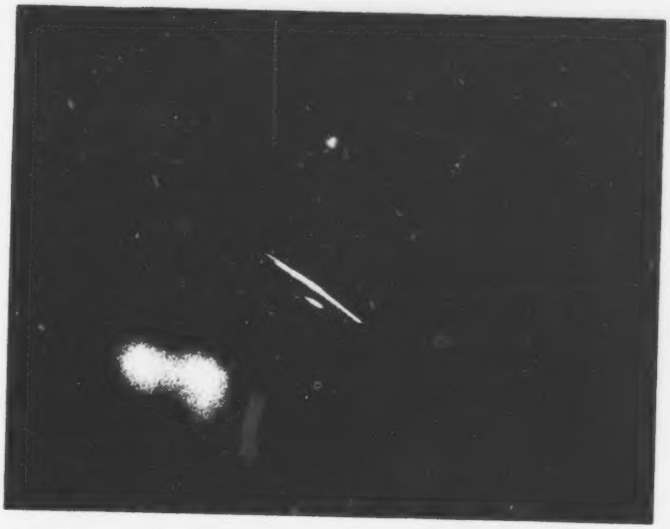

(B) HOLOGRAM 16C, SCATTERING ANGLE OF 150 DEGREES.

Figure 3-27. Reconstruction Photos of Hologram 16A at 30 Degrees Scattering Angle, and Hologram 16C at 150 Degrees Scattering Angle. The smoke is illuminated by secondary scattered light from the thread.

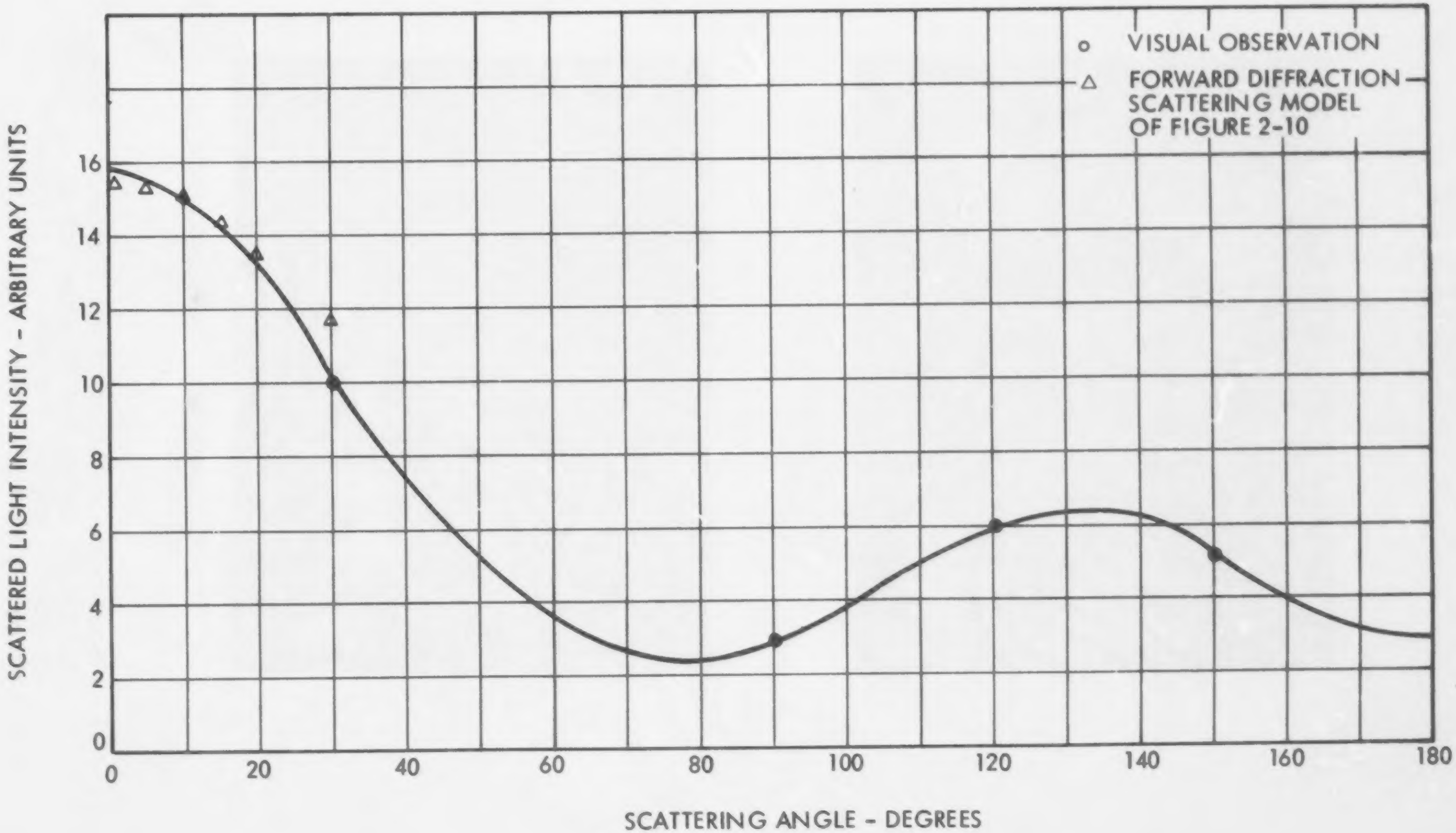

Figure 3-28. Observed and Calculated Scattered Light Intensity Distribution from Tobacco Smoke

a plot of relative scattered light intensity distribution as a function of scattering angle.

It is worth noting that the shape of this curve shows a strong resemblance to the shape of the gain function for totally reflecting particles of size X = 3. This can be seen from Figure 2-7. A match was sought for the forward scattered light portion of the distribution by using the Fraunhofer diffraction scattering model developed in Sections 2.3 and 2.5. A fairly good fit to the observed forward scattering was obtained from diffraction scattering from a log-normal distribution having parameters $X_g = 1.0$ and $\sigma_g = 1.7$. A value of n_0 depends on calibrating the curve to absolute scattered intensity.

The theoretical diffraction scattering for this distribution is also shown in Figure 3-28. The value $X_g = 1.0$ corresponds to a 0.22-micron geometric mean diameter particulate. The three-sigma distribution limits for $\sigma_g = 1.7$ give a size range from about 0.05 micron to 1.0 micron. This is in good agreement with known data on smoke particulate size distributions.[11]

The theoretical points in Figure 3-28 were calculated from the coefficients of Table 2-2 and Table 2-4 and have been renormalized on a scale of 15 to agree with the maximum observed scattered light intensity at a scattering angle of 10 degrees. The theoretical points in Figure 3-28 are the same as were shown in Figure 2-10, where the normalization was to unit number density, incident beam intensity, and wave number.

Particle Number Density

The three particulate distributions which were measured also represented three particle number densities. Of these we were able to obtain estimates of two.

The water droplet density distribution was neither stochastic nor homogeneous, since the droplets were generated in a straight stream, and no mixing mechanism was employed to disperse them. However, the droplet spacing results in an effective number density in a localized volume element, and this can be calculated directly from the aerosol generator characteristics.

The droplet velocity at a generating frequency of 3 kilocycles and a volume flow rate of 0.02 cc/sec (as shown in discussion in Section 3.2) can be calculated as 158 cm/sec. The droplet spacing is then equal to the velocity divided by the frequency, and comes out to be 525 microns, or about 10 times the droplet radius. The droplets disperse very little over their path to the scene volume, as is evident from examination of Figure 3-25. If we consider each droplet as being contained in a spherical volume element of diameter equal to the droplet spacing, the resulting number density is of order 1.3×10^4 particles per cubic centimeter.

The density of the tobacco smoke clouds which were generated can be estimated directly from relative scattered light intensity measurements. Using the Spectra-physics 124 Helium-Neon loser, the beam energy incident on the scene was measured as

$$I_o = 28 \text{ milliwatts/cm}^2.$$

This measurement was made with the UDT power meter, using a beam diameter of 0.5 centimeter at the scene volume. With the light scattering thread in place, the power meter was used to measure an isotropic scattered light distribution of 10^{-7} watts at a distance of 6.4 centimeter from the thread. With a one-square-centimeter detector area, this gives a scattered light intensity of

$$J_{ref} \ \delta V_{ref} = 4 \times 10^{-6} \text{ watts/sterad}$$

scattered off the whole thread. The thread was approximately 100 microns in diameter, and the illuminated portion was about one centimeter long. This gives a reference beam to scene beam intensity of

$$\frac{J_{ref} \ \delta V_{ref}}{I_o} = 1.5 \times 10^{-4} \frac{\text{cm}^2}{\text{sterad}} \qquad (3\text{-}11)$$

for either the He-Ne laser or the pulsed ruby laser. Note the difference in units of J_{ref} and I_o, such that I_o is a power flux as previously defined, but J_{ref} has units of watts/cm^3-sterad, and δV_{ref} is the scattering volume of the reference thread. The factor δV_{ref} is of secondary importance since it cancels out.

Now a visual estimate of relative scattered light intensity from the smoke cloud was obtained from hologram 13A, at a forward scattering angle of 30 degrees. The scattered light intensity per unit area from the smoke, in watts/sterad-cm^2, was estimated to be about 1 percent of that from the reference thread. The solid angle subtended was of course the same for both. The illuminated area of the thread which was visible was about 0.01 square centimeters, while the smoke cloud presented a viewing area of 2 square centimeters. Thus the total scattered light from the thread, in watts/sterad, was about twice the total scattered light from the scene, in watts/sterad, at 30 degrees scattering angle. This comes from multiplying the observed light intensity in watts/cm^2-sterad by the appropriate area. On alternatively, we multiply their ratios. We then have

$$\frac{J\ \delta V_s}{J_{ref}\ \delta V_{ref}} = 2 \tag{3-12}$$

where J and δV_s are the scattered scene light intensity and the scene volume as previously defined. Multiplying Equation (3-11) by (3-12) we then have

$$\frac{J\ \delta V_s}{I_o} = 3 \times 10^{-4}\ \frac{\mathrm{cm}^2}{\mathrm{sterad}} \tag{3-13}$$

The value of δV_s for the smoke-filled scene was about 2 cm^3, so we have a ratio which can be compared with the first of Equations (2-22).

$$\frac{J}{I_o} = \frac{1}{4k^2}\,\underline{h}\cdot\underline{C}_j = 1.5 \times 10^{-4}\ \frac{\mathrm{cm}^2}{\mathrm{sterad}} \tag{3-14}$$

Here the index j corresponds to the 30-degree scattering angle, and the product $\underline{h}\cdot\underline{C}_j$ is just the appropriate element of the A matrix which may be found in Table 2-4 to be equal to 2.686 n_o. Substituting this in Equation (3-14) with $k = 4.53 \times 10^4\ \mathrm{cm}^{-1}$, and solving for n_o, we find

$$n_o = 4.58 \times 10^5\ \mathrm{cm}^{-3}$$

This is roughly a factor of thirty more than the effective density of the 50-micron water droplets, and leads to an inter-particle spacing of about 100 microns.

Particle Velocity

In the Garrett holocamera experiments the phenolic and glass microballoons were thrust into the scene volume with a forced air nebulizer as discussed previously in this section. The incense smoke was wafted into the scene volume by convection. In neither case was the velocity measured, but in either case the velocity was only severla feet per second, or 100 cm/sec or less.

When the monodisperse aerosol generator was used, the velocity of the stream of water droplets could be readily calculated from the flow characteristics of the orifice. It was found to be about 160 cm/sec at a volume flow rate of 0.02 cc/sec of alcohol.

The cigarette smoke used to make holographic recordings with the three-beam wide angle scattered light holocamera was also injected into the scene volume with forced air. The velocity of this air stream was measured with a hot wire anomometer, and was found to be about 100 cm/sec.

The objective of these experiments insofar as particulate velocity is concerned was to measure the particle velocity and determine its effects on the holographic recording process, and on our ability to measure and analyze the other important particle distribution and light scattering parameters. In each of the above cases the velocity was low enough and the laser pulse time fast enough that velocity considerations were not important.

In recording holograms of particles by scattered laser light, one has to consider the stability of the interference pattern recorded by the photographic plate. If the interference pattern moves during the exposure time, then the plate records a smeared or composite interference pattern. The result is a greatly degraded reconstructed image.

It can be shown from the theory of holography that high quality reconstructions are realized whenever the optical path does not change more than one-tenth of the laser's wavelength during the hologram's exposure. At first glance, this might seem too restricting. The back scatter condition is the worst case. Here one is limited to low particle velocities, even with short ~ 50 nanosecond duration laser pulses. For example, if a particle is moving away from the hologram, the path change (Δ) is twice the product of particle velocity and laser pulse duration (i.e., $\Delta = 2\nu\tau$). Thus, to keep the interference pattern stationary, the path change must be less than the tenth wavelength bound. The velocity for back scatter must not exceed

$$v_b \le \frac{\lambda/10}{2\tau} . \qquad (3\text{-}15)$$

For a conventional Q-switch ruby laser, $\tau \sim 50$ nanoseconds and $\lambda = 0.6943$. Thus, $v_b \le 1$ meter/second, which is not particularly fast. More recently, the pulse duration of a ruby laser has been shortened to 2 nanoseconds by electro-optical chopping techniques. This factor of 25 decrease in pulse duration means a comparable increase in particle velocity, or a limiting velocity for the back scatter case of over 25 meters per second. Short pulses, however, have short coherence lengths which limit the amount of depth that can be recorded in a scene with a single reference beam. A one nanosecond pulse corresponds to a coherence length of 30 centimeters (1 foot), or a scene depth of 15 centimeters (6 inches). This limitation can be overcome by having a reference beam which is derived from mirrors at increasing 15-centimeter intervals. Such innovations are beyond the intent of the present discussion.

Holograms recorded by forward scatter greatly relax the velocity requirements. There are several cases which are best considered separately. The worst case is where the particle moves parallel to the hologram and viewing is at an angle relative to the input beam (the input beam is toward the viewer). The hologram is parallel to the particle motion. It can be shown from trigonometric arguments that for this case

$$\underset{(\text{motion}||)}{v_{max}} \le \frac{\Delta}{\lambda \sin\theta} = \frac{\lambda}{10\ \tau \sin\theta} \qquad (3\text{-}16)$$

As the viewing angle approaches 0 degrees, the maximum permitted particle velocity diverges. Table 3-4 compiles some representative values.

If one views in the direction perpendicular to both the particle direction and the direction of propagation of the laser beam, then it can be shown that the limiting particle velocity to record a hologram becomes

$$v_{max_0} \le \frac{\sqrt{\Delta r}}{\tau} = \frac{1}{\tau}\sqrt{\frac{\lambda r}{10}} \qquad (3\text{-}17)$$

Table 3-4. Maximum Velocity for Q-Switch Ruby Laser Forward-Scattered Hologram With Particle Moving Parallel to Hologram

Viewing Angle Relative to Laser Beam θ (degrees)	$v_{max. \parallel}$ (τ = 50 nanoseconds) (meter/sec)
1	$\leq$ 79.5 meter/sec
3	$\leq$ 26.5 meter/sec
5	$\leq$ 15.9 meter/sec
10	$\leq$ 8.0 meter/sec
15	$\leq$ 5.3 meter/sec
20	$\leq$ 4.1 meter/sec

where r is the distance of the particle from the hologram. For this case the velocity is independent of the viewing angle. The direction of propagation of the laser beam is perpendicular to the plane of the holograms. The viewing is perpendicular to the direction of motion of the particle and at an angle ϕ relative to the plane determined by the laser beam and the direction of motion of the particle.

Table 3-5 gives a compilation of the maximum velocities for different ranges for a 0.6943 μ - 50 nanosecond ruby laser pulse. The permitted velocities are now much high due to the greater insensitivity of this geometry on particle motion.

Table 3-5. Maximum Velocity for Q-Switched Ruby Laser for Different Ranges and for Particle Moving Parallel to Hologram and Viewing Along All Angles Perpendicular to Motion

Range D (Centimeters)	Maximum Velocity, v_{max_o} (kilometer/sec)
1 cm	0.525
10 cm	1.66
100 cm	5.25
1000 cm	16.6

An even more insensitive case is where the particle moves either toward or away from the hologram. It can be shown that for this case

$$v_{max_\perp} \leq \frac{\Delta}{\tau(1 - \cos\theta)} \qquad (3\text{-}18)$$

where in the above equation is the angle between the direction of viewing and the direction of propagation of the input laser beam. For this case, both the direction of viewing and the direction of propagation lie in the same plane. A compilation of maximum velocities for motions toward and away from the hologram is given in Table 3-6.

The preceding discussion has shown that velocity restrictions are less in the forward scattering case than in the back scattering condition. In addition, more light is scattered in the forward direction, making the recording of the hologram an easier task. Forward scattering holography also minimizes the coherence requirements on the laser.

Table 3-6. Maximum Velocity for Q-Switched Ruby Laser Forward Scattered Hologram When Particle Moves Toward or Away from the Hologram

Viewing Angle θ (Degrees)	Maximum Velocity $v_{max_\perp}$
1/2	≤35 kilometers/sec
1	≤9 kilometers/sec
2	≤2.3 kilometers/sec
3	≤1.0 kilometers/sec
5	≤360 meters/sec
10	≤91 meters/sec
15	≤41 meters/sec
20	≤20 meters/sec

4. CONCLUSIONS AND RECOMMENDATIONS

4.1 CONCLUSIONS

1) Individual particulates of sizes greater than about 20 microns can be detected, recorded, and reconstructed with scattered light holography. They may not necessarily be resolved. It was demonstrated with the three-beam scattered light holocamera and the monodisperse droplet generator that there is sufficient angular variation in the forward scattered light intensity to determine their sizes by diffraction scattering.

2) Particulates whose diameters are approximately the same as the wavelength of the scattered light (0.1 to 1.0 micron for ruby laser light) can be holographically recorded and reconstructed from any angle to obtain a size distribution. If there is a holographic intensity reference beam, a particulate density may also be recovered. Experiments with both the two-beam and three-beam scattered light holocameras show that forward scattered light is by far the easiest to analyze. Besides being more intense and having more pronounced angular variation, it is independent of the particulate index of refraction.

3) The use of three holographic beams does not increase the recording sensitivity. It is necessary, however, if aggregate densities are to be obtained where no resolution is possible. This was verified from experiments with the three-beam scattered light holocamera and with breadboard holographic sensitivity tests.

4) For particulate larger than the wavelength of the scattered light, particulate size distribution can be obtained from forward diffraction scattering which is independent of particulate optical properties or system resolving power.

5) A limiting value for scene-to-reference beam light intensity ratio has been established at 3×10^{-7}.

4.2 RECOMMENDATIONS

1) The use of a 180-degree angular range scattered light holocamera is generally not necessary to obtain adequate data. The preferable method is low angle forward scattering, and the next preferable is back scattering.

2) A particulate measurement holocamera should include two reference beams to enable an absolute determination of scattered light intensity.

3) The two reference beams should both be collimated and of uniform intensity for best results in reconstruction and calibration.

REFERENCES

1. Matthews, B.J., and Kemp, R.F., "Development of Laser Instrumentation for Particle Measurement," TRW Report No. 14103-6003-RO-00 (EPA Contract No. CPA 70-4), June 1971.

2. Matthews, B.J., and Kemp, R.F., "Investigation of Scattered Light Holography of Aerosols and Data Reduction Techniques," TRW Report No. 14103-6002-RO-00 (EPA Contract No. CPA 70-4), November 1970.

3. H.C. Van de Hulst, Light Scattering by Small Particles, John Wiley & Sons, New York, 1957.

4. Milton Kerker, The Scattering of Light and Other Electromagnetic Radiation, Academic Press, New York, 1969.

5. Kerker, M., Matijevic, E., Espenscheid, W., Farone, W., and Kitani,S., J. Colloid Sci. 19, 213, (1964).

6. Wallach, M.L. and Heller, W., J. Phys. Chem. 68, 924, (1964).

7. Chin, J.H., Sliepcevich, C.M., and Tribus, M., J. Phys. Chem. 59, 845 (1955).

8. Shifrin, K.S., and Perelman, A.Y., Tellus 18, 566 (1966).

9. Shifrin, K.S., and Perelman, A.Y., Opt. Spectry. (USSR) (English Translation) 20, 75, 386 (1966).

10. T.W. Anderson, Introduction of Multivariate Statistical Analysis, John Wiley & Sons, New York, 1958.

11. Air Pollution Manual: Part II, Control Equipment, American Industrial Hygiene Association, Detroit, Michigan, 1968.

12. Wuerker, R.F., Heflinger, L.O., and Briones, R.A., "Holographic Interferometry with Ultraviolet Light," Applied Physics Letters, 12, pp 302-303, May 1968.

13. Wuerker, R.F., Matthews, B.J., and Briones, R.A., "Production Holograms of Reacting Sprays in Liquid Propellant Rocket Engines," Final Report, JPL Contract #952023, NAS 7-100, TRW Report 68.4712.2-024, 31 July 1968.

14. Wuerker, R.F., "Operation Manual for Transmission Holocamera," Contract F04611-69-C-0015, AFPRL, Edwards, California, February 1970.

15. Wuerker, R.F., "Pulsed Laser Holography," published in E.R. Robertson and J.M. Harvey, The Engineering Uses of Holography, Cambridge University Press (1970).

16. Berglund, R.N., and Liu, B.Y.H., "Generation of Monodisperse Aerosol Standards," Environmental Science and Technology 7 No. 2, Feb. 1973.

17. Wuerker, R.F., Koboyashi, R.J., Heflinger, L.O., and Ware, T.C., "Application of Holography to Flow Visualization Within a Rotating Compressor Blade Row," Garrett AiResearch Final Report 73-9489, NASA CR-121264, Sept. 1973.

APPENDIX A

THE IMAGINARY PART OF THE INDEX OF REFRACTION

If the index of refraction has an imaginary part, the propagation of light is altered. It will be quickly shown that the imaginary part represents an attenuation of a light wave passing through a medium of index n.

In its simplest form the propagation of light may be expressed as:

$$\text{Wave} = A_0 e^{j(\omega t - kx)} \tag{A-1}$$

where,

A_0	is the amplitude of the light wave
e	is the base of the natural system of logarithms
j	is $\sqrt{-1}$
ω	is the angular frequency f of the wave in radians per unit time ($\omega = 2\pi f$)
t	is time
k	is the wave number (i.e., $k = 2\pi/\lambda$)
x	is distance

The equation represents a wave moving to the right at a constant velocity. This can be seen by setting the argument of the exponent equal to a constant; namely, $\omega t - kx$ = constant. Differentiating x with respect to t one obtains $dx/dt \equiv C$. In vacuum, the index of refraction is unity. When light moves through a media of refractive index not equal to unity, the wave felocity slows. The index n is related to the velocity v by the following: $v = c/n$. By substitution, one can write the original equation in terms of n:

$$\begin{aligned} \text{Wave} &= A_0 e^{j(\omega t - n\omega x/c)} \\ &= A_0 e^{j(t - nx/c)\omega} \end{aligned} \tag{A-2}$$

Now let $n = n_o - j\Delta$ so that the index of refraction contains both a real (n_o) and an imaginary ($j\Delta$) part. The symbol Δ represents the numerical value of the imaginary part. Again, by substitution,

$$\text{Wave} = A_o e^{j(t - n_o x/c + j\Delta x/c)}$$

$$= A_o e^{-(\Delta\omega/c)x} \quad e^{j(t - n_o x/c)\omega} \qquad \text{(A-3)}$$

Inspection of Equation (A-3) shows that it now contains a term $A_o e^{-(\Delta\omega/c)x}$. This quantity represents an attenuation of the wave amplitude as the distance x increases. This occurs due to the imaginary part of the index. The attenuation is multiplied by the function $e^{j(t - n_o x/c)\omega}$, which has already been shown to be the expression for a right traveling wave [Equation (A-1)]. The wave moves to the right at a velocity $dx/dt = v = c/n_o$.

In essence, the real part of the refractive index determines the speed of light through a given medium while the imaginary part imposes a damping effect on the light wave resulting in attenuation or absorption of the wave energy.

APPENDIX B

COMPUTER PROGRAM FOR FORWARD DIFFRACTION SCATTERING

A small, study-type computer program was written in the BASIC language to compute the elements of the $\underline{A}$ matrix for forward diffraction scattering. The matrix elements are computed using Equation (2-22) with $I_0/4k^2 = 1$. The calculation of the $\underline{\underline{H}}$ matrix is done as shown in Equations (2-25) and (2-26), with N_0 normalized to one.

The program computes the first five forward diffraction scattering coefficients, which are the coefficients of x^{2n}, for $n = 1$ to 5, in the expression for the scattering gain function as shown in Equations (2-20).

$$G(x,\theta) = \frac{2J_1\,(x\sin\theta)}{x\sin\theta}^{\,2}$$

These coefficients are found from Equation (2-21) and are displayed in Table 2-2.

It is assumed that three angles are input, and that three parameters of a log-normal distribution are adjusted to obtain the desired intensity distribution. These parameters are $Y = \ln N_0$, $\overline{\mu}$, and σ, as in Equation (2-24). The intensity distribution is the same as the first column of the A matrix.

The program is displayed in Figure B-1. The input angles go into a three-component vector called T, and are called for by the program's interactive input capability. The program also calls for input of geometric mean and standard deviation of the distribution, which are called M and S respectively. This input is also by the interactive mode. The adjustment parameters are then designated by $U = \overline{U}1$ and $\sigma = U2$ in the program. The C, H and A matrices all retain that nomenclature in the program.

```
10  PRINT "INPUT THREE ANGLES,DEG."
20  MATINPUT T(3)
30  DIM C(3,5),D(3),H(5,3)
40  FØR I=1 TØ 3
50  C(I,1)=1
60  Q=(SIN(PI*T(I)/180))↑2
65  C(I,2)=-.25*Q
70  C(I,3)=(5/192)*(Q↑2)
75  C(I,4)=-(7/4608)*(Q↑3)
77  C(I,5)=(11/184320)*(Q↑4)
80  NEXT I
90  PRINT "C2","C4","C6","C8","C10"
100 MATPRINT C
110 PRINT "INPUT GEØM. MEAN, S.D."
120 INPUT M,S
130 U1=LØG(M)
140 U2=LØG(S)
150 S=U2↑2
160 FØR I=1 TØ 5
170 H(I,1)=EXP(4*(I+1)*S*(U1+(I+1)*S))
180 H(I,2)=2*(I+1)*H(I,1)
190 H(I,3)=(1+12*S*(I+1)↑2)*H(I,1)/(2*U2)
200 NEXT I
205 PRINT "H MATRIX"
210 PRINT "GAMMA","UBAR","SIGMA"
220 MATPRINT H
230 PRINT "A MATRIX"
235 MAT A(3,3)=C*H
240 MATPRINT A
```

Figure B-1. A Computer Program in BASIC, to Calculate the Forward Diffraction Scattering Distribution